Monthly Notices of the ROYAL ASTRONOMICAL SOCIETY

MNRAS **521,** 3348–3383 (2023) https://doi.org/10.1093/mnras/stad424
Advance Access publication 2023 February 8

The ALMOND survey: molecular cloud properties and gas density tracers across 25 nearby spiral galaxies with ALMA

Lukas Neumann [1★] Molly J. Gallagher,[2] Frank Bigiel,[1] Adam K. Leroy,[2] Ashley T. Barnes [1,3] Antonio Usero,[4] Jakob S. den Brok [1,5] Francesco Belfiore [6] Ivana Bešlić,[1] Yixian Cao,[7] Mélanie Chevance [8,9] Daniel A. Dale,[10] Cosima Eibensteiner,[1] Simon C. O. Glover [8] Kathryn Grasha [11,12] Jonathan D. Henshaw [13,14] María J. Jiménez-Donaire [4,15] Ralf S. Klessen [8,16] J. M. Diederik Kruijssen [9] Daizhong Liu,[7] Sharon Meidt,[17] Jérôme Pety,[18,19] Johannes Puschnig [1] Miguel Querejeta,[4] Erik Rosolowsky [20] Eva Schinnerer,[13] Andreas Schruba,[7] Mattia C. Sormani [8] Jiayi Sun [2,21,22] Yu-Hsuan Teng [23] and Thomas G. Williams [11,24]

Affiliations are listed at the end of the paper

Accepted 2023 January 31. Received 2022 December 16; in original form 2022 June 8

ABSTRACT

We use new HCN(1–0) data from the ACA Large-sample Mapping Of Nearby galaxies in Dense gas (ALMOND) survey to trace the kpc-scale molecular gas density structure and CO(2–1) data from the Physics at High Angular resolution in Nearby GalaxieS–Atacama Large Millimeter/submillimeter Array (PHANGS–ALMA) to trace the bulk molecular gas across 25 nearby star-forming galaxies. At 2.1 kpc scale, we measure the density-sensitive HCN/CO line ratio and the star formation rate (SFR)/HCN ratio to trace the star formation efficiency in the denser molecular medium. At 150 pc scale, we measure structural and dynamical properties of the molecular gas via CO(2–1) line emission, which is linked to the lower resolution data using an intensity-weighted averaging method. We find positive correlations (negative) of HCN/CO (SFR/HCN) with the surface density, the velocity dispersion, and the internal turbulent pressure of the molecular gas. These observed correlations agree with expected trends from turbulent models of star formation, which consider a single free-fall time gravitational collapse. Our results show that the kpc-scale HCN/CO line ratio is a powerful tool to trace the 150 pc scale average density distribution of the molecular clouds. Lastly, we find systematic variations of the SFR/HCN ratio with cloud-scale molecular gas properties, which are incompatible with a universal star formation efficiency. Overall, these findings show that mean molecular gas density, molecular cloud properties, and star formation are closely linked in a coherent way, and observations of density-sensitive molecular gas tracers are a useful tool to analyse these variations, linking molecular gas physics to stellar output across galaxy discs.

Key words: ISM: clouds – ISM: molecules – ISM: structure – galaxies: ISM – galaxies: star formation – radio lines: ISM.

1 INTRODUCTION

Star formation is at the heart of many astrophysical processes ranging from planet formation to the evolution of whole galaxies. Yet, the details of the star-forming process are far from being well understood. We know from observations inside the Milky Way (MW) and of other galaxies that the star formation rate (SFR) per unit area is tightly correlated to the gas surface density (e.g. Schmidt 1959; Kennicutt 1998; Bigiel et al. 2008; Schruba et al. 2011; Leroy et al. 2013). In more detail, observations of MW star-forming regions show that stars form specifically within the densest parts of molecular clouds (MCs) and that the SFR of individual clouds correlates with the mass of dense gas[1] ($M_{\rm dense}$) as traced by dust emission (e.g. Lada & Lada 2003; Kainulainen et al. 2009; André et al. 2014) or emission of high excitation density lines (e.g. Wu et al. 2005, 2010; Stephens et al. 2016). In a landmark paper, Gao & Solomon (2004) used HCN emission to trace $M_{\rm dense}$ from a large sample of external galaxies and found a linear relation between SFR and $M_{\rm dense}$. Following up, Wu et al. (2005) studied HCN emission in local molecular clouds confirming the linear SFR–$M_{\rm dense}$ relation that, combining MC and integrated whole galaxy observations, spans 10 dex. These studies suggest that the star formation efficiency of dense gas ($\rm SFE_{dense} \equiv SFR/M_{dense}$) may be constant across this wide range of scales and environments.

However, the works by Usero et al. (2015), Bigiel et al. (2016), Gallagher et al. (2018a), Jiménez-Donaire et al. (2019), and Bemis & Wilson (2019) on kpc-scale spectroscopic measurements find systematic variations of the HCN/CO line ratio and the SFR/HCN ratio with kpc-scale environmental properties, e.g. the molecular gas surface density or the stellar mass surface density. In addition, observations of the MW's Central Molecular Zone (CMZ) show that the star formation efficiency of dense gas is much lower than

★ E-mail: lukas.neumann.astro@gmail.com

[1] Here the term 'dense gas' refers to a density $n_{\rm H_2} \gtrsim 10^4$ cm^{-3} and is primarily used to distinguish it from the lower density molecular gas traced by low-J CO.

is seen in the rest of the Galaxy (see e.g. Longmore et al. 2013; Barnes et al. 2017). This apparent underproduction of stars follows naturally if the critical density of star formation is environmentally dependent, as predicted by turbulent star formation theories (e.g. Kruijssen et al. 2014). One persistent question about these results is how HCN/CO or similar ratios (e.g. HCO^+/CO, CS/CO) trace density variations quantitatively in different environments when observed in other galaxies. In an attempt to address this, Gallagher et al. (2018b) took a novel step comparing the kpc-scale spectroscopic measurements with the ∼100 pc scale molecular gas surface density in their five galaxies sample. They found systematic variations of the HCN/CO line ratio, a proxy for the fraction of dense molecular gas, as a function of the molecular gas surface density. This approach directly connects our two major methods of assessing density and gas properties in extragalactic systems: high-resolution spectroscopic CO imaging and multispecies (HCN, HCO^+, and CS) spectroscopy.

Combining multispecies spectroscopy with high-resolution imaging has applications beyond only constraining density estimates. Turbulent theories of star formation predict that molecular cloud properties such as mean density, velocity dispersion, or magnetic fields influence the density structure of the clouds, which regulate their ability to emit HCN (e.g. Krumholz & McKee 2005; Hennebelle & Chabrier 2011; Padoan & Nordlund 2011; Federrath & Klessen 2012; Padoan et al. 2014). Moreover, these same parameters also regulate the SFE_{dense} of the clouds, thus providing a first-order explanation of the observed correlations between the HCN/CO and SFR/HCN ratios and molecular cloud properties.

Until very recently, the exploration of such potential correlations was limited because high-resolution (∼100 pc) CO imaging of the full molecular gas disc of galaxies has been almost as rare as kpc-scale and full-disc spectroscopy (see e.g. Wong & Blitz 2002; Leroy et al. 2009 for kpc CO mapping, and e.g. Usero et al. 2015; Jiménez-Donaire et al. 2019 for kpc HCN mapping). This situation was recently directly addressed in the Physics at High Angular resolution in Nearby GalaxieS (PHANGS) project,[2] which uses the Atacama Large Millimeter/submillimeter Array (ALMA) to observe the molecular gas via the CO(2–1) line at ∼1–2 arcsec resolution in 90 nearby ($d < 25$ Mpc) galaxies (PHANGS–ALMA; Leroy et al. 2021b). This survey allows access to the molecular gas distribution at ∼100 pc physical scales, which is close to the size of individual giant molecular clouds (GMCs). By combining PHANGS–ALMA with spectral mapping of dense gas tracers like HCN(1–0), we can explore the molecular cloud properties in the extragalactic regime and compare it to the kpc-scale dense gas spectroscopy. This technique bypasses the lack of extragalactic cloud-scale dense gas observations that are currently only available for a few galaxies (M51, Querejeta et al. 2019; NGC 3627, Bešlić et al. 2021; NGC 1068, Sánchez-García et al. 2022).

Tracing dense gas associated with star formation is challenging at extragalactic distances because tracers of dense gas that are currently popular in Galactic studies, e.g. N_2H^+ (see e.g. Kauffmann et al. 2017; Pety et al. 2017; Barnes et al. 2020), are too faint to be mapped at kpc-scales across the discs of external galaxies with current instrumentation within reasonable time. Still, we can gain a lot of information about the dense gas by focusing on the brightest higher critical density lines, i.e. HCN(1–0) or HCO^+(1–0). The primary method to measure dense gas is based on the observation of various molecular emission lines with a range of effective critical densities (n_{eff}; see e.g. Leroy et al. 2017a; Gallagher et al. 2018a). To first order, the intensity of a line reflects the total gas mass above n_{eff}, though see discussion in Shirley (2015) and Mangum & Shirley (2015). Therefore, the ratio of two lines with different critical densities reflects the ratio of gas masses above the two critical densities. For example, comparison between CO and HCN line emission yields an approximate gauge of the dense gas fraction (e.g. see Usero et al. 2015; Bigiel et al. 2016 and reference therein), as the latter requires a significantly larger density for excitation.[3]

Accordingly, in this paper, we combine a large new HCN (along with HCO^+ and CS) data set with PHANGS–ALMA CO observations and use the HCN(1–0)/CO(2–1) ratio to trace the fraction of dense gas. Because the targets were picked to overlap PHANGS–ALMA, we have cloud-scale gas properties and infrared (IR)- and ultraviolet (UV)-based SFR estimates across the whole sample. We explore the correlations of several cloud-scale structural and dynamical gas properties with both the HCN/CO ratio, a proxy for the dense gas fraction (f_{dense}), and the SFR/HCN ratio, a proxy for the dense gas star formation efficiency (SFE_{dense}), across a sample of 25 galaxies. This builds on the study of Gallagher et al. (2018b), who used a subset of these data (five galaxies) and considered only HCN/CO and cloud-scale molecular gas surface density (Σ_{mol}), and on the works of Leroy et al. (2017b) and Utomo et al. (2018), who compared CO-based cloud properties to the star formation efficiency in the bulk molecular medium traced by CO emission (SFE_{mol}). We compare the kpc-scale HCN/CO and SFR/HCN to the cloud-scale molecular gas surface density (Σ_{mol}), the velocity dispersion (σ_{mol}), the virial parameter (α_{vir}), and the internal turbulent pressure (P_{turb}) as defined in Section 4.3. We measure Σ_{mol}, σ_{mol}, α_{vir}, and P_{turb} using CO(2–1) data from the PHANGS–ALMA survey, and we measure HCN/CO and SFR/HCN using HCN(1–0) data from new ALMA observations, called the ACA Large-sample Mapping Of Nearby galaxies in Dense gas (ALMOND) survey. ALMOND uses the Morita Atacama Compact Array (ACA) to observe a subsample of 25 targets of the PHANGS–ALMA survey in dense molecular gas tracers like HCN(1–0), HCO^+(1–0), or CS(2–1). Our goal is to characterize the impact of these cloud-scale gas properties on the amount and star-forming ability of the dense gas and its connection with local environment.

This paper is organized as follows. First, we lay out the concept that motivates the studied correlations based on turbulent cloud models in Section 2. Next, we describe our data products and methods in Section 3. In Section 5, we present the main results where we compare the dense gas to cloud-scale molecular gas properties. We further analyse the findings in Section 6 where we separately look at the galaxies' centres. Finally, we summarize and discuss the results in Section 7. In the online version, we provide supplementary figures.

2 EXPECTATIONS

2.1 Does HCN/CO trace dense gas fraction?

The goal of this section is to set a qualitative, first-order expectation of the relations between molecular cloud properties and the $W_{HCN}/W_{CO(2-1)}$ ratio (hereafter HCN/CO) and the Σ_{SFR}/W_{HCN} integrated intensity ratio (hereafter SFR/HCN). Using established models of star formation (e.g. Krumholz & McKee 2005; see Section 2.2), we model the probability distribution function (PDF)

[2] http://phangs.org

[3] $n_{eff}(HCN(1–0)) \approx 2 \times 10^4$–$2 \times 10^5$ cm^{-3}, $n_{eff}(CO(2–1)) \approx 1 \times 10^3$ cm^{-3} (Mangum & Shirley 2015; Shirley 2015; Leroy et al. 2017a; Onus, Krumholz & Federrath 2018).

of the gas density of molecular clouds as a function of several cloud properties, i.e. the mean surface density n_0, the Mach number $\mathcal{M}$, and the virial parameter $\alpha_{\rm vir}$ (in Section 4.3, we explain our best empirical estimates of these molecular cloud properties). Then, based on the density PDF, we infer qualitative changes of HCN/CO and SFR/HCN as a function of the molecular cloud properties. At the model level, we can infer the gas masses traced above certain density thresholds and thus estimate the dense gas fraction ($f_{\rm dense}$) and star formation efficiency (SFE$_{\rm dense}$). Therefore, to infer HCN/CO and SFR/HCN from the models we assume that HCN(1–0) and CO(2–1) emission trace the gas mass above a certain effective critical density using a constant mass-to-light conversion factor. However, Galactic observations, albeit largely limited to selected local clouds or even subregions of these (e.g. Kauffmann et al. 2017; Pety et al. 2017; Barnes et al. 2020; Evans Neal J. et al. 2020), and simulations (e.g. Mangum & Shirley 2015; Shirley 2015; Leroy et al. 2017a; Onus et al. 2018; Jones et al. 2022) have clearly shown that reality is more complex. Rather than simply tracing gas above some fixed density threshold, HCN always traces a convolution of the density distribution and density-dependent emissivity, with additional complications offered by chemical abundance variations, variations in temperature, and possible excitation by collisions with electrons. Despite these concerns, the preponderance of evidence even in the studies above supports the use of the HCN/CO ratio as a tracer of the density distribution in a cloud, with higher HCN/CO reflecting denser gas.

Given these uncertainties, in our analysis, we focus on the observational quantities, i.e. HCN/CO and SFR/HCN, rather than the less certain physical quantities, i.e. $f_{\rm dense}$ and SFE$_{\rm dense}$. In this section laying out basic theoretical expectations, we adopt the simpler picture that HCN emission has a step-function dependence on density and emits with a fixed mass-to-light ratio, or conversion factor, above that density threshold. The purpose is not to derive quantitative predictions about line emissivities but instead to discuss how currently popular models predict the directions of observed correlations between cloud-scale molecular gas properties and dense gas spectroscopy.

We also note further alternative descriptions of the basic theoretical framework, we adopt (e.g. Hennebelle & Chabrier 2011; Federrath & Klessen 2012) and refer the reader to those works for more quantitative discussion of turbulent cloud models.

2.2 Turbulent cloud models

In turbulent models of star formation (e.g. Padoan & Nordlund 2002, 2011; Krumholz & McKee 2005; Hennebelle & Chabrier 2011; Federrath & Klessen 2012, 2013; Padoan et al. 2014), the PDF ($p(n)$) of the molecular gas number density, n, is to first order described by a lognormal function, which can be written as

$$p(s)\,{\rm d}s = \frac{1}{\sqrt{2\pi\sigma_{\rm s}^2}} \exp\left[-\frac{(s-s_0)^2}{2\sigma_{\rm s}^2}\right] {\rm d}s, \tag{1}$$

where $s = \ln(n/n_0)$ is the logarithmic number density in units of the mean number density, n_0, and $s_0 = -\sigma_{\rm s}^2/2$ is the centre of the PDF. Note that gravitational collapse and star formation will introduce a power-law tail at high densities (see e.g. Girichidis et al. 2014; Burkhart 2018). This is particularly noticeable in the high-density gas of individual molecular clouds (e.g. Kainulainen et al. 2009; Schneider et al. 2015). However, we expect the contribution of the power-law tail to the overall mass budget of the multiphase interstellar medium (ISM) to be negligible at the larger scales of ~150 pc and above (e.g. in entire gravitationally bound GMCs; e.g. Klessen & Glover 2016).

For isothermal turbulent flows, the width of the lognormal PDF is quantified by the rms Mach number $\mathcal{M} \equiv \sigma_{\rm 3D}/c_{\rm s}$ ($\sigma_{\rm 3D}$ is the three-dimensional velocity dispersion and $c_{\rm s}$ is the sound speed of the molecular gas), the turbulence driving parameter, b, and the gas to magnetic pressure ratio, β (see e.g. Padoan & Nordlund 2011; Molina et al. 2012):

$$\sigma_{\rm s}^2 = \ln\left(1 + b^2\mathcal{M}^2\frac{\beta}{\beta+1}\right). \tag{2}$$

The parameter b depends on the ratio of compressive versus solenoidal modes and on the dimensionality of the flow. For isotropic turbulence in isothermal gas with a natural mix of both modes contributing equally, simple theoretical considerations lead to $b = 3/4$ in two and $b = 2/3$ in three dimensions (Federrath, Klessen & Schmidt 2008). Numerical simulations indicate somewhat smaller values (Federrath et al. 2010), however, with considerable scatter. We follow Padoan & Nordlund (2002), neglect magnetic fields ($\beta \to \infty$) and adopt $b \sim 0.5$ such that the width of the PDF becomes

$$\sigma_{\rm s}^2 = \ln\left(1 + 0.25\,\mathcal{M}^2\right). \tag{3}$$

The above formalism implies a link between the distribution of mass above any given density and the mean properties of molecular clouds, i.e. for varying mean density (n_0) or velocity dispersion ($\sigma_{\rm mol}$) as is illustrated in Fig. 1. Here, we adopt the prescription from Krumholz & McKee (2005, hereafter KM theory) to compute the density threshold $n_{\rm SF}$ above which gas is considered to collapse and form stars within a free-fall time:

$$\frac{n_{\rm SF}}{n_0} = 0.82\,\alpha_{\rm vir}\,\mathcal{M}^2. \tag{4}$$

Assuming a fixed virial parameter $\alpha_{\rm vir} \approx 1.3$ (Krumholz & McKee 2005), the above equation reads $n_{\rm SF}/n_0 \approx 1.07\mathcal{M}^2$. Thus, for fixed virial parameter, the physical interpretation drawn from equation (4) is that stars form in local overdensities of the molecular clouds determined by the density contrast $n_{\rm SF}/n_0$ that shifts to higher overdensities if the turbulence ($\mathcal{M}$) of the molecular gas increases. Variations of the virial parameter are small (~0.7 dex; Sun et al. 2020b) compared to variations of the mean density (~3.4 dex) or the Mach number (~1.7 dex) of molecular clouds that justifies assuming a fixed $\alpha_{\rm vir}$ to first order. However, variations of $\alpha_{\rm vir}$ are still evident and might also manifest in the spectroscopic observations, e.g. by affecting $n_{\rm SF}$. In this simplified model, $\alpha_{\rm vir}$ does not affect the PDF and thus HCN/CO is unaffected by changes in $\alpha_{\rm vir}$. On the contrary, based on equation (4), $n_{\rm SF}$ increases for increasing $\alpha_{\rm vir}$ that would result in a negative correlation between SFR/HCN and $\alpha_{\rm vir}$. In practice, in this study, we infer the virial parameter from observations by assuming a fixed cloud-scale, such that $\alpha_{\rm vir} \propto \sigma_{\rm mol}^2/\Sigma_{\rm mol}$ (see Section 4.3.3). In this case, $\alpha_{\rm vir}$ is correlated with $\sigma_{\rm mol}$ (tracing $\mathcal{M}$) and $\Sigma_{\rm mol}$ (tracing n_0) making the effect of $\alpha_{\rm vir}$ on HCN/CO and SFR/HCN more complex. Still, we can estimate how $\sigma_{\rm mol}^2/\Sigma_{\rm mol}$ tracing $\alpha_{\rm vir}$ affects HCN/CO and SFR/HCN taking into account the distribution and thus the correlation of molecular cloud properties based on observations (see Sections 2.4 and 2.5 and Fig. 2).

2.3 Line emissivity

In an ideal case, we can detect molecular lines, such as HCN(1–0) or CO(2–1), if a substantial fraction of the gas is at densities close to or above the so-called 'critical density' for emission. Considering the simplest case of only collisional (de)excitation (e.g. within

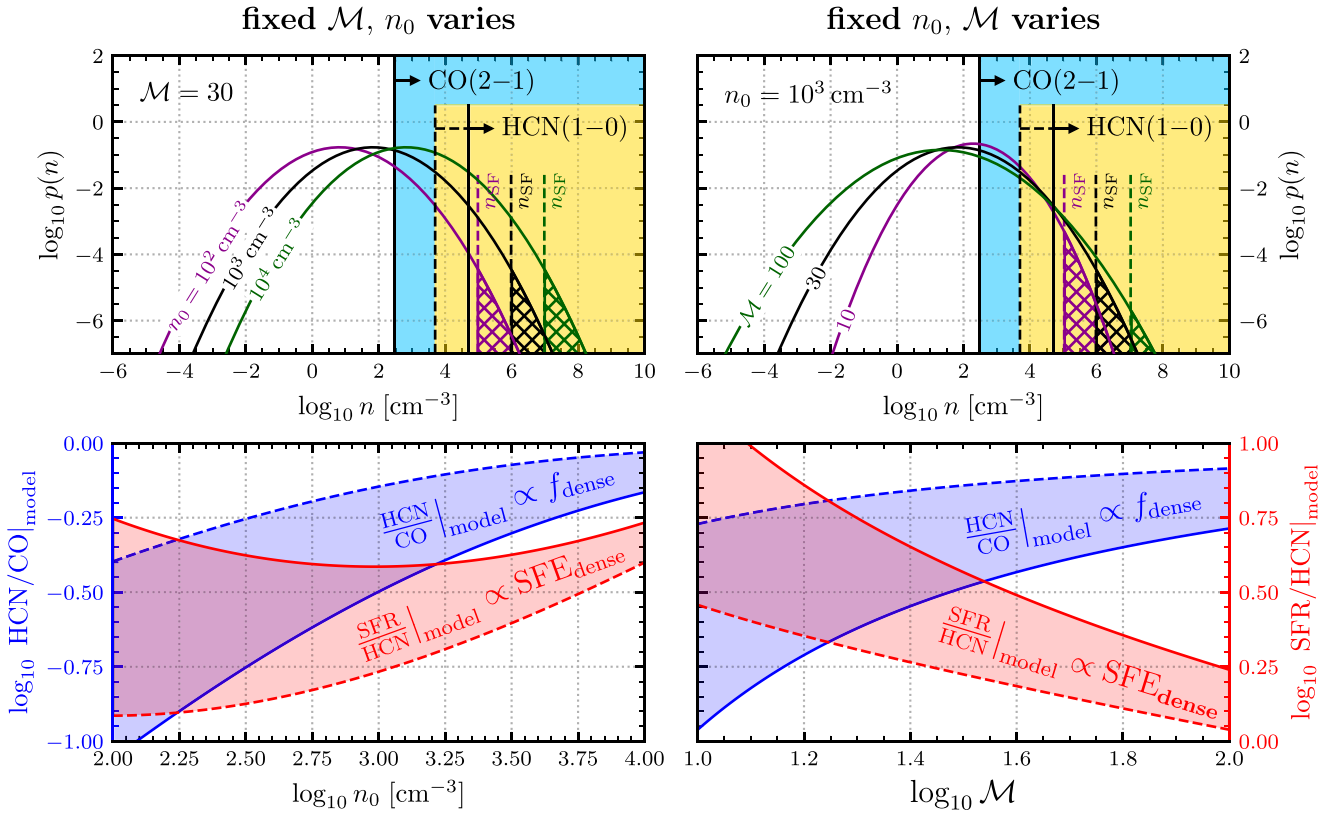

Figure 1. Top: volume-weighted probability distribution functions (PDFs) of the molecular cloud gas density, n, for varying mean density (n_0, left-hand panel) and varying Mach number ($\mathcal{M}$, right-hand panel). The light blue shaded area indicates the density regime traced by CO(2–1), i.e. all gas above $n_{\rm eff}(\mathrm{CO}) = 3 \times 10^2$ cm^{-3} (Leroy et al. 2017a). Analogously, the yellow shaded area is the density regime traced by HCN(1–0), where we adopted two effective critical densities such that in one case (solid line) HCN traces all gas above $n_{\rm eff}(\mathrm{HCN}) = 5 \times 10^4$ cm^{-3} (Leroy et al. 2017a) and in the other case (dashed line) HCN traces gas above $n_{\rm eff}(\mathrm{HCN}) = 5 \times 10^3$ cm^{-3} (Onus et al. 2018). The dashed lines labelled with $n_{\rm SF}$ show the threshold density above which gas in clouds collapses to form stars. Thus, the hatched areas are a measure of the SFR per free-fall time. Bottom: HCN/CO as a proxy for $f_{\rm dense}$ and SFR/HCN as a proxy for $\mathrm{SFE}_{\rm dense}$ estimated from the PDFs as a function of the mean density (left-hand panel) and the Mach number (right-hand panel) in accordance with the top panel plots. We compute HCN/CO as the ratio of the integrated mass-weighted PDFs within the assumed density regimes (equation 6). Similarly, SFR/HCN is obtained by integrating the mass-weighted PDF above $n_{\rm SF}$ accounting for the free-fall time at mean density and dividing with the area of the PDF traced by HCN (equation 7). The solid line and dashed lines are in accordance with the density thresholds in the top panels.

dense molecular clouds), this critical density can be defined as the density at which the collisional de-excitation rate and spontaneous de-excitation are equal, and hence above this density line emission is enhanced. In general, the critical density of a certain line depends on the optical depth (τ) of the line and the kinetic temperature (T) of the gas (e.g. Tielens 2010; Draine 2011; Mangum & Shirley 2015; Shirley 2015; Klessen & Glover 2016). The concept of a critical density, above which all the line emission is associated with the gas mass above that critical density, is, however, somewhat limited in lower density gas, as subthermal excitation effects (e.g. Pety et al. 2017) and additional excitation mechanisms can be significant (e.g. see Goldsmith & Kauffmann 2018). None the less, to first order, we consider all gas above a respective critical density to be traced by the respective molecular line emission. We select the density threshold based on the emissivity–density curves derived by Leroy et al. (2017a, their fig. 2). We define the threshold where their normalized emissivity (ϵ) exceeds 50 per cent, i.e. at $n_{\rm eff}(\mathrm{HCN}) = 5 \times 10^4$ cm^{-3} for HCN(1–0) and $n_{\rm eff}(\mathrm{CO}) = 3 \times 10^2$ cm^{-3} for CO(2–1) as illustrated in Fig. 1 (left-hand panels). The value of $n_{\rm eff}$ for HCN has, however, been the subject of some debate in the recent literature (e.g. Kauffmann et al. 2017; Barnes et al. 2020). For example, numerical simulations from Onus et al. (2018) and Jones et al. (2022) find that HCN(1–0) emission traces gas at densities of $n_{\rm eff}(\mathrm{HCN}) = 1 \times 10^3$–$1 \times 10^4$ cm^{-3}, which is around an order of magnitude lower than reported by Leroy et al. (2017a). Note, however, that Leroy et al. (2017a) use a different definition of the effective critical density and that both results may be consistent with each other. Nevertheless, to account for some variation of $n_{\rm eff}$, we adopt a second, lower critical density of $n_{\rm eff}(\mathrm{HCN}) = 5 \times 10^3$ cm^{-3} (dashed line in Fig. 1).[4] We then use these density regimes to infer the gas mass traced by HCN(1–0) or CO(2–1) emission via integration of the mass-weighted PDF:

$$I_{\rm line} \propto \int_{s_{\rm eff(line)}}^{\infty} \frac{n}{n_0}\, p(s)\, \mathrm{d}s, \tag{5}$$

where $s_{\rm eff}$(line) is the effective critical line density in units of $s = \ln(n/n_0)$ corresponding to $n_{\rm eff}$(line). Note that this formalism does not consider radiative transfer modelling and therefore only gives reasonable HCN/CO estimates in terms of comparative analysis.

[4]Note that we adopt a single critical density for CO emission, which could suffer from similar effects. Albeit given its already low critical density, which sits close to the density where molecular gas forms ($\sim 10^2$ cm^{-3}), this effect should be less pronounced than with HCN.

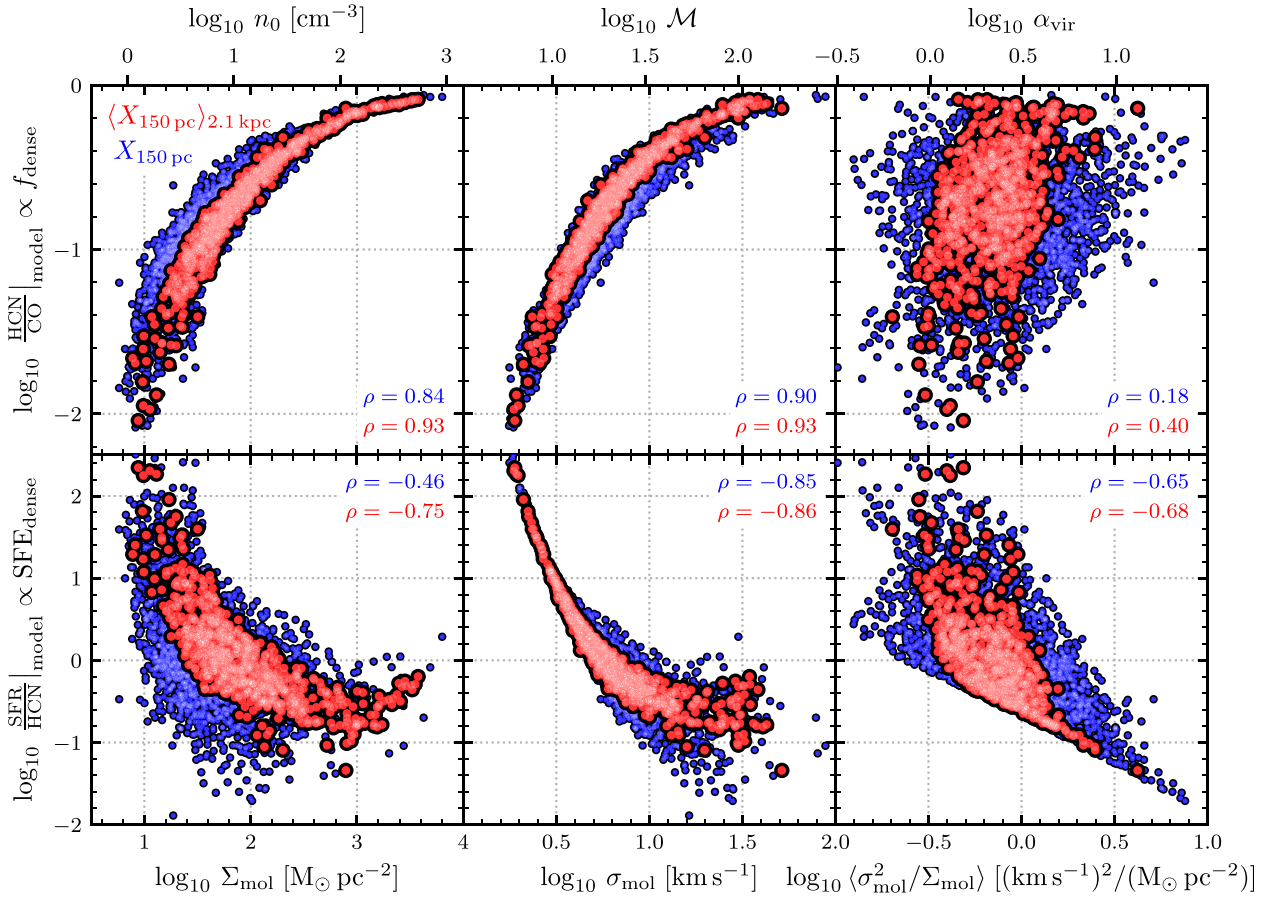

Figure 2. Model predictions of HCN/CO and SFR/HCN against the molecular cloud properties $\Sigma_{\rm mol}$, $\sigma_{\rm mol}$, and $\alpha_{\rm vir}$ (similar to Sun et al. 2018). HCN/CO and SFR/HCN are computed as in equations (6) and (7) based on a lognormal PDF and assuming $n_{\rm eff}({\rm HCN}) = 5 \times 10^3$ cm^{-3}. The PDF parameters (n_0, $\mathcal{M}$, and $\alpha_{\rm vir}$) are inferred from the observed 150 pc molecular gas measurements ($\Sigma_{\rm mol}$, $\sigma_{\rm mol}$, and $\alpha_{\rm vir} \propto \sigma^2_{\rm mol}/\Sigma_{\rm mol}$). The red data points depict the intensity-weighted averages of the 150 pc measurements (blue) at an averaging scale of 2.1 kpc (see Section 4.4 for more details). We show the Pearson correlation coefficient ρ for both the original data and the weighted averages.

2.4 HCN/CO correlations

Turbulent cloud models predict the density distribution and SFR as a function of the molecular cloud properties. In the following, we adopt the description introduced in Section 2.2 and infer simplified line emissivities (Section 2.3). In Fig. 1, we show how variations of molecular cloud properties affect the molecular gas density distribution, i.e. the PDF, and consequently the HCN/CO ratio.

At first, we keep the virial parameter fixed at $\alpha_{\rm vir} = 1.3$ and vary the mean density for fixed Mach number and vice versa. In Fig. 1 (top left-hand panel), we show how the cloud's PDF changes as a function of the mean density (n_0), keeping the Mach number fixed at $\mathcal{M} = 30$ that corresponds to $\sigma_{\rm mol} \approx 5$ km s^{-1} assuming a sound speed of $c_{\rm s} = 0.3$ km s^{-1} (at $T \sim 20$ K; Krumholz & McKee 2005). We adopt typical molecular cloud densities, varying n_0 from 1×10^2 to 1×10^4 cm^{-3} that results in a shift of the PDF to higher densities without changing the width of the PDF. We estimate the expected HCN/CO line ratio based on a simplified emissivity model and critical densities of HCN(1–0) and CO(2–1) discussed above (Section 2.3) by integrating the PDF over the density ranges of the respective lines:

$$\left.\frac{\rm HCN}{\rm CO}\right|_{\rm model} = \frac{\int_{s_{\rm eff}({\rm HCN})}^{\infty} \frac{n}{n_0}\, p(s)\, {\rm d}s}{\int_{s_{\rm eff}({\rm CO})}^{\infty} \frac{n}{n_0}\, p(s)\, {\rm d}s}, \tag{6}$$

where the respective HCN and CO effective critical densities are $n_{\rm eff}({\rm HCN}) = 5 \times 10^4$ cm^{-3} (Leroy et al. 2017a) or $n_{\rm eff}({\rm HCN}) = 5 \times 10^3$ cm^{-3} (Onus et al. 2018) and $n_{\rm eff}({\rm CO}) = 2 \times 10^3$ cm^{-3}. This procedure computes the mass of gas that is traced by the different molecular lines, which serves as a first-order estimate of the expected line intensities assuming a constant mass-to-light ratio. Note that equation (6) does not account for the different HCN(1–0) and CO(2–1) mass-to-light conversion factors. Thus we only claim to predict changes in HCN/CO. Moreover, we assume a fixed effective critical density of HCN(1–0) and that the emissivity of the lines below $n_{\rm eff}$ is zero. However, in reality, $n_{\rm eff}$ can vary and the emissivity below $n_{\rm eff}$ is not zero. Therefore, if the dense gas fraction is low, a significant fraction of the HCN emission could come from lower density gas. Thus, our toy model will predict a steeper correlation at low n_0 and low $\mathcal{M}$.

We find that the HCN/CO line ratio positively correlates with the mean density of the molecular cloud (see top right-hand panel of Fig. 1). The physical explanation is that at low mean densities $n_0 \sim 10^2$ cm^{-3} the CO(2–1) line is easily excited while only a small fraction of the cloud's gas is at densities high enough to produce HCN(1–0) emission producing a low HCN/CO line ratio. Increasing n_0 leads to an increasing fraction of gas at the (effective) critical density of HCN(1–0) thus increasing the HCN(1–0) luminosity while the CO(2–1) luminosity is only marginally affected by increasing n_0

due to its low critical density. Thus, increasing the mean density of the cloud results in a higher HCN/CO line ratio. If we assume the CO(2–1) intensity to be a robust tracer of the surface density of the molecular gas at cloud-scales and further assume that the geometry of the clouds is similar such that surface density traces mean density, we expect a positive correlation between the surface density of molecular clouds and the HCN/CO line ratio as a proxy of the dense gas fraction. The connection between cloud-scale $\Sigma_{\rm mol}$ and HCN/CO has already been tested by Gallagher et al. (2018b), who found a positive correlation, thus supporting the model expectation.

Similarly, we vary the Mach number (and consequently the velocity dispersion) of the molecular cloud adopting typical values of $\mathcal{M} = 10$–100 while keeping the mean density fixed at $n_0 = 10^3$ cm^{-3}. Comparing with Krumholz & Thompson (2007), the range of Mach numbers describes normal ($\mathcal{M} \sim 30$) over intermediate ($\mathcal{M} \sim 50$) to starburst galaxies ($\mathcal{M} \sim 80$). We find that increasing the turbulence of the molecular cloud widens the PDF without significantly shifting its peak ($s_0 = -\sigma_s^2/2$; see bottom left-hand panel of Fig. 1). As a result, at low velocity dispersion the PDF is narrow and centred around a density of order 10^2 cm^{-3} such that only a small fraction of the gas is at high densities. Therefore, the HCN(1–0) intensity is low while the CO(2–1) intensity is high, hence we expect a small HCN/CO line ratio. Increasing the velocity dispersion leads to a widening of the PDF such that a larger fraction of the gas is at higher densities thus increasing the HCN(1–0) luminosity much more than the CO(2–1) that is less affected by the width of the PDF. Thus, assuming that the velocity dispersion is traced by the CO(2–1) line width, we expect a positive correlation between the line width and the HCN/CO line ratio as shown in the bottom right-hand panel of Fig. 1.

As mentioned above, in this simplified model prescription, the actual (theoretical) virial parameter does not affect the PDF thus leaving HCN/CO unchanged. However, the empirical virial parameter, if measured as $\alpha_{\rm vir} \propto \sigma_{\rm mol}^2/\Sigma_{\rm mol}$, might be connected to changes in HCN/CO. Therefore, under the assumption that the virial parameter is proportional to $\sigma_{\rm mol}^2/\Sigma_{\rm mol}$ (see Section 4.3.3), we can study changes of HCN/CO with the empirically inferred virial parameter. In Fig. 2 (upper row), we show how the model HCN/CO varies with the empirically based molecular cloud properties (see Appendix A for the distribution of the measured cloud-scale gas properties). Each data point corresponds to an aperture in one of our target galaxies. Blue dots indicate measurements at 150 pc, while red dots indicate averages over 2.1 kpc apertures using a mass-weighting scheme (see Section 4.4). We predict HCN/CO as described above adopting the following data-to-model parameter conversions. We convert the observationally inferred $\Sigma_{\rm mol}$ into n_0 assuming spherical clouds with radius R, such that the depth of the cloud is given by the beam size, e.g. $2R = 150$ pc, leading to $n_0/[\,{\rm cm}^{-3}] = 3/(4R\mu m_{\rm H})\,\Sigma_{\rm mol} = 0.144 \times \Sigma_{\rm mol}/[{\rm M}_\odot\ {\rm pc}^{-2}]$, where $\mu = 2.8$ is the mean particle weight per hydrogen molecule assuming all hydrogen is H_2 (Kauffmann et al. 2008) and $m_{\rm H}$ is the mass of the hydrogen atom. Assuming a sound speed of $c_{\rm s} = 0.3$ km s^{-1} we obtain $\mathcal{M} = \sqrt{3}\,\sigma_{\rm mol}/c_{\rm s} = 5.8 \times \sigma_{\rm mol}/[{\rm km\,s^{-1}}]$, where we assume an isotropic velocity dispersion, hence the factor $\sqrt{3}$. In accordance with the model predictions above, we find HCN/CO to positively correlate with n_0 and $\mathcal{M}$. In addition, we observe a weak positive correlation of HCN/CO with the virial parameter (Pearson correlation $\rho = 0.14$ for the 150 pc measurements and $\rho = 0.40$ for the 2.1 kpc scale weighted averages). Physically, the virial parameter is a measure of the gravitational boundedness, where higher $\alpha_{\rm vir}$ means less bound. The derived (weak) positive correlation between HCN/CO and $\alpha_{\rm vir}$ implies that less bound clouds tend to have more dense gas per molecular gas that seems counterintuitive given that one might expect a higher dense gas fraction for more bound clouds. However, high HCN/CO is also connected to highly turbulent clouds as is shown above. Indeed, we observe a steeper correlation of HCN/CO with Mach number than with n_0, therefore a positive correlation between HCN/CO and $\alpha_{\rm vir}$ is indeed not surprising.

2.5 SFR/HCN correlations

Similar to the HCN/CO correlations above, we can make predictions about the SFR-to-HCN ratio as a function of molecular cloud properties. We model the SFR using equation (4) where all gas above the threshold density $n_{\rm SF}$ is considered to form stars and $n_{\rm SF}$ is completely determined by the mean density (n_0) and the Mach number ($\mathcal{M}$), $n_{\rm SF} \propto n_0\mathcal{M}^2$ at fixed $\alpha_{\rm vir} = 1.3$. This allows us to compute $n_{\rm SF}$ for any given tuple (n_0, $\mathcal{M}$) or equivalently ($\Sigma_{\rm mol}$, $\sigma_{\rm mol}$). We add $n_{\rm SF}$ as vertical dashed lines in Fig. 1 and consider the cloud's gas above this threshold (hatched area) as the star-forming gas. Similar to HCN/CO and following Krumholz & McKee (2005), we estimate SFR/HCN by integrating the PDF over the relevant density ranges:

$$\left.\frac{\rm SFR}{\rm HCN}\right|_{\rm model} = \frac{\int_{s_{\rm SF}}^{\infty} \frac{n}{\sqrt{n_0}}\, p(s)\,{\rm d}s}{\int_{s_{\rm eff(HCN)}}^{\infty} \frac{n}{n_0}\, p(s)\,{\rm d}s}, \tag{7}$$

where $n_{\rm eff}$(HCN) is defined as in Section 2.4. Equation (7) accounts for the (inverse) dependence of the SFR on the mean free-fall time $t_{\rm ff,0} = \sqrt{3\pi/(32G\rho_0)} \propto \rho_0^{-1/2} \propto n_0^{-1/2}$ (e.g. Padoan et al. 2014). Again, we are only interested in relative changes of SFR/HCN so that the units have no physical meaning. We note that the prescription adopted here assumes a single free-fall time, while other pictures (e.g. Federrath & Klessen 2012) adopt a multi-free-fall approach that include an additional density-dependent factor (a ratio of free-fall times) inside the integral in the numerator of equation (7). Multi-free-fall models can predict that $\rm SFE_{dense}$ increases with Mach number, i.e. the reverse of single-free-fall models predictions and the reverse of the trends found here at low n_0, $\mathcal{M}$ (Fig. 2). Given the sense of observed $\rm SFE_{dense}$ trends examined in this work and by others (Querejeta et al. 2015; Leroy et al. 2017a; Utomo et al., in preparation), we proceed with the single free-fall class of models in the following.

We explore the effect of the molecular cloud properties on SFR/HCN within the same parameter space as of HCN/CO. We find that $\mathcal{M}$ negatively correlates with SFR/HCN, as is shown in the bottom right-hand panel of Fig. 1. This can be understood in the following way. At low velocity dispersion, HCN is a good tracer of the density regime where the stars are expected to form and thus the SFR/HCN ratio is high. For increasing turbulence the HCN luminosity becomes a less ideal tracer of the local overdensities and traces more of the bulk molecular gas leading to a decreasing SFR/HCN. For changes of SFR/HCN with the mean density the model predicts a decreasing trend at low n_0 and an increasing trend at high n_0 and hence no clear correlation between SFR/HCN and n_0. We can understand the different dependencies in the following way. At low $n_0 \ll n_{\rm eff}$ an increase in n_0 leads to HCN tracing more of the bulk molecular gas such that SFR/HCN decreases leading to a negative correlation between SFR/HCN and n_0 similar to $\mathcal{M}$. Though, if n_0 reaches densities comparable to the critical density of HCN(1–0) the ratio between the gas masses above $n_{\rm eff}$(HCN) and $n_{\rm SF}$ is barely affected by changes in n_0. However, the SFR depends on the mean free-fall time such that a higher gas mass is converted into stars within a shorter time ($t_{\rm ff,0} \propto n_0^{-1/2}$) leading to an increase

of SFR/HCN with increasing n_0. As a result, we expect a negative correlation between SFR/HCN at $n_0 \ll n_{\rm eff}$(HCN), $n_{\rm SF}$ and a positive correlation at $n_0 \sim n_{\rm eff}$(HCN), $n_{\rm SF}$.

Analogously to Section 2.4, we additionally infer SFR/HCN for every data-based triplet (n_0, $\mathcal{M}$, $\alpha_{\rm vir}$) meaning for each aperture, n_0 and $\mathcal{M}$ are traced via $\Sigma_{\rm mol}$ and $\sigma_{\rm mol}$, respectively, and $\alpha_{\rm vir}$ is proportional to $\sigma^2_{\rm mol}/\Sigma_{\rm mol}$. The resulting relations (SFR/HCN against cloud properties) are shown in Fig. 2 (lower panels). Remarkably, we find a clear negative correlation between SFR/HCN and n_0 in contrast to the less clear relation shown in Fig. 1, where n_0 is varied at fixed $\mathcal{M}$. There are two reasons that we do not observe the upturn of SFR/HCN at higher n_0. First, the n_0 values inferred from $\Sigma_{\rm mol}$ are $\sim$1–2 dex lower than the adopted values in Fig. 1 so that n_0 is mostly lower than $n_{\rm eff}$ (HCN) or $n_{\rm SF}$ and the dependence on the free-fall time is less important. Second, the strong negative correlation between SFR/HCN and $\mathcal{M}$ in combination with the positive correlation of n_0 and $\mathcal{M}$ can overcompensate the SFR/HCN upturn at higher n_0 thus leading to a negative correlation between SFR/HCN and n_0.

In the KM model description, $\alpha_{\rm vir}$ affects $n_{\rm SF}$ without affecting the PDF and thus the line emissivity. This would result in a negative correlation between SFR/HCN and $\alpha_{\rm vir}$. However, we measure $\alpha_{\rm vir}$ via $\sigma^2_{\rm mol}/\Sigma_{\rm mol}$ assuming a fixed cloud size (see Section 4.3.3). Thus, $\alpha_{\rm vir}$ is constrained by the observational $\Sigma_{\rm mol}$ and $\sigma_{\rm mol}$ values and we want to explore variation of the model's SFR/HCN with $\sigma^2_{\rm mol}/\Sigma_{\rm mol}$. Analogously to Section 2.4, we infer SFR/HCN for every observationally based triplet (n_0, $\mathcal{M}$, $\alpha_{\rm vir}$) based on the same model description as above but also accounting for variations in $\alpha_{\rm vir}$. The resulting relations (SFR/HCN against cloud properties) are shown in Fig. 2 (lower panels). Consistent with the results above we find very strong negative correlations of SFR/HCN with n_0 and $\mathcal{M}$. Moreover, we observe a moderate negative correlation of SFR/HCN with the virial parameter (Pearson correlation $\rho = -0.43$ for the 150 pc scale measurement and $\rho = -0.57$ for the weighted averages). The virial parameter quantifies the gravitational boundedness of the cloud. The derived anticorrelation between $\alpha_{\rm vir}$ and SFR/HCN supports the concept that less bound clouds tend to be less efficient in producing stars from the dense gas (lower SFR/HCN).

3 OBSERVATIONS

In this study, we link the kpc-scale dense gas spectroscopy with the cloud-scale molecular gas properties across 25 nearby galaxies. To enable this we present a new ALMA survey of high critical density molecular lines, which we call ALMOND ('ACA Large-sample Mapping of Nearby galaxies in Dense gas'). ALMOND aimed to detect emission from high critical density lines, HCN(1–0), HCO^+(1–0), and CS(2–1), from targets of the PHANGS–ALMA survey. Following standard practice for extragalactic work (e.g. Gao & Solomon 2004; Usero et al. 2015; Bigiel et al. 2016; Gallagher et al. 2018a; Querejeta et al. 2019), ALMOND initially focuses on HCN(1–0) (hereafter HCN), HCO^+(1–0), and CS(2–1) as our primary tracer of dense molecular gas. We designed ALMOND with the goal of detecting these high critical density tracers, and as a result began by targeting the more massive and actively star-forming PHANGS–ALMA targets. All targets are nearby ($d <$ 25 Mpc), relatively massive ($10^{10} \lesssim M_\star \lesssim 10^{11}$ $M_\odot$) gas-rich ($10^9 \lesssim M_{\rm H_2} \lesssim 10^{10}\,M_\odot$), star-forming ($1 \lesssim$ SFR $\lesssim 10$ $M_\odot$ yr^{-1}) galaxies, selected based on the PHANGS–ALMA CO (2–1) maps and mid-IR emission so that we expected the ACA to be able to achieve significant detections of the high critical density rotational lines near $\nu \approx$ 85–100 GHz, HCN(1–0), HCO^+(1–0), CS(2–1), at least in the galaxy centres and across spiral arms. At these nearby distances, even the moderate angular resolution of the ACA allows us to resolve key environmental features (centre, bar, spiral arms) in both the bulk and dense molecular gas. Our diverse sample covers a variety of morphology, including 16 barred (nine unbarred) galaxies and 11 galaxies containing (14 without) an active galactic nucleus (AGN). Table 1 lists the galaxy sample along with their physical properties. We summarize the used data products in Table 2.

3.1 New HCN(1–0) observations

ALMOND observed 25 nearby galaxies in dense molecular gas tracers using the Morita ACA as part of the ALMA facility. The ACA consists of four 12-m dishes that operate in single-dish ('total power', TP) mode and an array of fourteen 7-m telescopes. The spectral set-up is similar to the one described in Gallagher et al. (2018a), and covers the brightest high critical density lines, HCN(1–0), HCO^+(1–0), and CS(2–1) and a suite of fainter lines. At these frequencies, the ACA has a native resolution of 17–22 arcsec that, for our targets, relates to physical scales of $\sim$1–2 kpc. In total, ALMOND currently includes 7-m + TP observations of 25 targets (projects 2017.1.00230.S, 2018.1.01171.S, and 2019.2.00134.S), which we combine in this analysis with additional 7-m + TP observations of NGC 2903 (project 2021.1.00740.S) and NGC 4321 (project 2017.1.00815.S). The data consist of a homogeneous set of ACA observations of a large sample of 23 galaxies with exceptionally deep observations of NGC 2903 and NGC 4321, for a total of 25 galaxies, which we believe to be the largest or one of the largest ever mapping surveys targeting these high critical density lines. The data reduction was carried out using the PHANGS–ALMA pipeline (for more details see Leroy et al. 2021a), which uses the standard ALMA data reduction package, CASA (CASA Team et al. 2022).

The resulting position–position–velocity (PPV) cubes have typical spectral resolution of 10 km s^{-1} and typical noise per channel of 1 mK for the deeper observations (NGC 2903 and NGC 4321) and $\sim$3 mK for the other 23 galaxies. The good sensitivity of the ACA allows us to detect HCN(1–0), HCO^+(1–0), and CS(2–1) emission in the centres of all targets and in individual locations across the molecular spiral arms in some of the ALMOND galaxies. Across all galaxies, we observe in total 4566 independent sightlines, whereof 242 sightlines show significant HCN emission, i.e. integrated intensities with the signal-to-noise ratio (S/N) ≥ 3.

Beyond the individual detections, the survey covers a large area and we know the likely location and velocity of the faint HCN(1–0) emission. This allows us to achieve widespread detections of these faint lines via stacking, e.g. constructing sensitive radial profiles. In Appendix B, we show that via spectral stacking HCN can be detected in the central 2 kpc in all galaxies, out to 4 and 6 kpc in 21 and 9 of the 25 galaxies, respectively. In Fig. 3, we illustrate this radial stacking spectra procedure and show the integrated intensities for NGC 4321. These are our deepest observations, and so are not typical, but they nicely illustrate the nature of the ALMOND data and the stacking procedures. For more details on the stacking method, see Appendix B. The complete atlas of maps and stacked spectra are made available online.

3.1.1 *CO(2–1) – bulk molecular gas*

We trace the bulk molecular gas via the CO(2–1) emission line as observed by the PHANGS–ALMA survey (Leroy et al. 2021b). ALMA produced CO(2–1) line maps with 1–2 arcsec resolution corresponding to physical scales of 25–180 pc, 2.5 km s^{-1} velocity

Table 1. Galaxy sample.

Galaxy	RA (J2000) (^{h}:^{m}:^{s})	Dec. (J2000) (°:′:″)	d (Mpc)	i (°)	$M_\star$ (10^9 M$_\odot$)	M_{H_2} (10^9 M$_\odot$)	SFR (M$_\odot$ yr^{-1})	SFR/$M_\star$ (10^{-10} yr^{-1})	Bar	AGN
(1)	(2)	(3)	(4)	(5)	(6)	(7)	(8)	(9)	(10)	(11)
NGC 0628	1:36:41.7	15:47:1.1	9.8	8.9	21.94	2.70	1.75	0.80	N	N
NGC 1097	2:46:18.9	−30:16:28.8	13.6	48.6	57.48	5.52	4.74	0.83	Y	Y
NGC 1365	3:33:36.4	−36:08:25.5	19.6	55.4	97.77	18.07	16.90	1.73	Y	Y
NGC 1385	3:37:28.6	−24:30:4.2	17.2	44.0	9.53	1.68	2.09	2.19	N	N
NGC 1511	3:59:36.6	−67:38:2.1	15.3	72.7	8.09	1.47	2.27	2.80	N	N
NGC 1546	4:14:36.3	−56:03:39.2	17.7	70.3	22.39	1.94	0.83	0.37	N	N
NGC 1566	4:20:0.4	−54:56:16.8	17.7	29.5	60.85	5.05	4.54	0.75	Y	Y
NGC 1672	4:45:42.5	−59:14:50.1	19.4	42.6	53.61	7.24	7.60	1.42	Y	Y
NGC 1792	5:5:14.3	−37:58:50.0	16.2	65.1	40.96	6.64	3.70	0.90	N	N
NGC 2566	8:18:45.6	−25:29:58.3	23.4	48.5	51.21	7.17	8.72	1.70	Y	N
NGC 2903	9:32:10.1	21:30:3.0	10.0	66.8	43.02	3.74	3.08	0.71	Y	N
NGC 2997	9:45:38.8	−31:11:27.9	14.1	33.0	54.06	6.79	4.37	0.81	N	N
NGC 3059	9:50:8.2	−73:55:19.9	20.2	29.4	23.87	2.43	2.38	1.00	Y	N
NGC 3521	11:5:48.6	−0:02:9.4	13.2	68.8	105.21	5.90	3.72	0.35	N	N
NGC 3621	11:18:16.3	−32:48:45.4	7.1	65.8	11.38	1.15	0.99	0.87	N	Y
NGC 4303	12:21:54.9	4:28:25.5	17.0	23.5	33.39	8.12	5.33	1.60	Y	Y
NGC 4321	12:22:54.9	15:49:20.3	15.2	38.5	55.61	7.77	3.56	0.64	Y	N
NGC 4535	12:34:20.3	8:11:52.7	15.8	44.7	33.96	3.99	2.16	0.64	Y	N
NGC 4536	12:34:27.1	2:11:17.7	16.2	66.0	25.07	2.62	3.45	1.37	Y	N
NGC 4569	12:36:49.8	13:9:46.4	15.8	70.0	64.04	4.55	1.32	0.21	Y	Y
NGC 4826	12:56:43.6	21:40:59.1	4.4	59.1	17.40	0.41	0.20	0.12	N	Y
NGC 5248	13:37:32.0	8:53:6.7	14.9	47.4	25.49	4.54	2.29	0.90	Y	N
NGC 5643	14:32:40.8	−44:10:28.6	12.7	29.9	21.69	2.66	2.59	1.20	Y	Y
NGC 6300	17:16:59.5	−62:49:14.0	11.6	49.6	29.45	1.90	1.89	0.64	Y	Y
NGC 7496	23:9:47.3	−43:25:40.3	18.7	35.9	9.92	1.81	2.26	2.28	Y	Y

Note. Column (2): right ascension; column (3): declination; column (4): distance (Anand et al. 2021); column (5): inclination angle (Lang et al. 2020); column (6): global stellar mass; column (7): global H_2 mass; and column (8): global star formation rate. Integrated galaxy properties in columns (6)–(8) are taken from Leroy et al. (2021b). Columns (10) and (11) specify if a galaxy is barred (Y) or unbarred (N) (Querejeta et al. 2021) and if it contains an AGN (Y) or not (N) (Véron-Cetty & Véron 2010).

resolution, and 0.2–0.3 K noise per channel. It combines interferometric and single-dish data from the 12-m array and the ACA consisting of the 7-m array and four 12-m dishes observing in total power mode. Thus, it should recover information on all physical scales. In Section 4.3, we infer various dynamical properties of the molecular gas following a series of studies (Sun et al. 2018, 2020a,b) that extensively analysed the molecular gas in PHANGS–ALMA.

3.2 UV + IR – star formation rate

We use star formation rate (SFR) maps from the 'z = 0 Multiwavelength Galaxy Synthesis' (z0MGS) study (Leroy et al. 2019) adopting a combination of 22 μm (*Wide-field Infrared Survey Explorer – WISE4*) and *Galaxy Evolution Explorer* (*GALEX*)-FUV 154 nm emission. Leroy et al. (2019) present an atlas of IR and UV images of ∼15 750 local ($d \lesssim 50$ Mpc) galaxies at a matched resolution of 7.5 and 15 arcsec. Leroy et al. (2019) find a linear combination of *WISE4* and FUV to be their most robust tracer of the SFR:

$$\left(\frac{\Sigma_{\rm SFR}}{\rm M_\odot\,yr^{-1}\,kpc^{-2}}\right) \approx (T_{\rm WISE4} + T_{\rm FUV})\,\cos i, \tag{8}$$

where

$$T_{\rm WISE4} = 3.24\times10^{-3}\left(\frac{\log_{10} C_{\rm WISE4}}{-42.7}\right)\left(\frac{I_{\rm WISE4}}{\rm MJy\,sr^{-1}}\right) \tag{9}$$

and

$$T_{\rm FUV} = 1.04\times10^{-1}\left(\frac{\log_{10} C_{\rm FUV}}{-43.42}\right)\left(\frac{I_{\rm FUV}}{\rm MJy\,sr^{-1}}\right). \tag{10}$$

We refer to Kennicutt & Evans (2012) for a comparative discussion of SFR tracers. In equation (8), i is the galaxy's inclination as listed in Table 1 and the cos i term corrects for the projection effect due to the galaxy's inclination. For galaxies without *GALEX* coverage, Leroy et al. (2019) also prescribe formulas using only *WISE4*. Table 2 lists the available SFR tracers for our sample. The coefficients $\log_{10} C_{\rm WISE4}$ depend on the galaxy and were benchmarked to Salim et al. (2016) and Salim, Boquien & Lee (2018) (see Leroy et al. 2019 for details). We downloaded the SFR maps for our galaxy sample at a resolution of 15 arcsec from the public z0MGS repository.[5] These maps are then convolved to the spatial resolution of the ACA maps (2.1 kpc ∼ 20 arcsec).

4 METHODS

The aim of this work is to compare the kpc-scale dense gas and SFR observations with the cloud-scale molecular gas properties. To do so we need to determine the integrated intensities of each line (Section 4.1). We then estimate the cloud-scale properties from the 150 pc scale CO(2–1) data (Section 4.3), and the dense gas quantities from the coarser HCN(1–0) and SFR data at 2.1 kpc scale (Section 4.2). Next, we explain the weighted-averaging method, which is used to compare these two scales (Section 4.4), and the data binning that is used to improve S/N (Section 4.5). Finally, we introduce the fitting scheme, which is used to constrain a first-order relation between the kpc- and cloud-scale quantities.

[5] irsa.ipac.caltech.edu/data/WISE/z0MGS

Table 2. Data/observations.

Galaxy	CO observations			HCN observations			SFR tracers
	Survey	Res. (arcsec)	Res. (pc)	Survey	Res. (arcsec)	Res. (kpc)	
(1)	(2)	(3)	(4)	(5)	(6)	(7)	(8)
NGC 0628	PHANGS–ALMA	1.12	53	ALMOND	18.6	0.89	*WISE4*, FUV
NGC 1097	PHANGS–ALMA	1.70	112	ALMOND	19.4	1.28	*WISE4*, FUV
NGC 1365	PHANGS–ALMA	1.38	131	ALMOND	20.6	1.96	*WISE4*, FUV
NGC 1385	PHANGS–ALMA	1.27	106	ALMOND	19.9	1.67	*WISE4*, FUV
NGC 1511	PHANGS–ALMA	1.45	107	ALMOND	17.6	1.30	*WISE4*, FUV
NGC 1546	PHANGS–ALMA	1.28	110	ALMOND	19.0	1.63	*WISE4*, FUV
NGC 1566	PHANGS–ALMA	1.25	108	ALMOND	19.8	1.69	*WISE4*, FUV
NGC 1672	PHANGS–ALMA	1.93	182	ALMOND	17.7	1.67	*WISE4*, FUV
NGC 1792	PHANGS–ALMA	1.92	151	ALMOND	18.8	1.47	*WISE4*, FUV
NGC 2566	PHANGS–ALMA	1.28	145	ALMOND	18.6	2.11	*WISE4*
NGC 2903	PHANGS–ALMA	1.45	71	ALMOND	18.4	0.89	*WISE4*, FUV
NGC 2997	PHANGS–ALMA	1.77	121	ALMOND	20.4	1.39	*WISE4*, FUV
NGC 3059	PHANGS–ALMA	1.22	120	ALMOND	16.8	1.64	*WISE4*
NGC 3521	PHANGS–ALMA	1.33	85	ALMOND	21.2	1.36	*WISE4*
NGC 3621	PHANGS–ALMA	1.82	62	ALMOND	18.9	0.65	*WISE4*, FUV
NGC 4303	PHANGS–ALMA	1.81	149	ALMOND	20.3	1.67	*WISE4*, FUV
NGC 4321	PHANGS–ALMA	1.67	123	ALMOND	19.7	1.45	*WISE4*, FUV
NGC 4535	PHANGS–ALMA	1.56	119	ALMOND	22.9	1.75	*WISE4*, FUV
NGC 4536	PHANGS–ALMA	1.48	116	ALMOND	21.6	1.70	*WISE4*, FUV
NGC 4569	PHANGS–ALMA	1.69	129	ALMOND	19.3	1.47	*WISE4*, FUV
NGC 4826	PHANGS–ALMA	1.26	27	ALMOND	18.8	0.40	*WISE4*, FUV
NGC 5248	PHANGS–ALMA	1.29	93	ALMOND	19.9	1.44	*WISE4*, FUV
NGC 5643	PHANGS–ALMA	1.30	80	ALMOND	18.1	1.11	*WISE4*
NGC 6300	PHANGS–ALMA	1.08	60	ALMOND	17.7	1.00	*WISE4*
NGC 7496	PHANGS–ALMA	1.68	152	ALMOND	17.9	1.63	*WISE4*, FUV

Note. Columns (2)–(4): CO(2–1) data from PHANGS–ALMA (Leroy et al. 2021b) along with their native resolutions (full width at half-maximum – FWHM) in arcsec and pc; columns (5)–(7): analogous for the HCN(1–0) data taken from ALMOND (this work); and column (8): applied star formation rate tracers from the *Wide-field Infrared Survey Explorer* (*WISE*; Wright et al. 2010) and the *Galaxy Evolution Explorer* (*GALEX*; Martin et al. 2005). The data have been spatially homogenized. The CO observations from PHANGS–ALMA have been convolved to a physical resolution of 150 pc and the HCN observations from ALMOND and the SFR maps have been convolved to 2.1 kpc.

Figure 4 shows a compilation of these data products for the galaxy NGC 4321.

4.1 Integrated intensity maps

We produce integrated intensity maps from the original CO(2–1), HCN(1–0) (analogously with HCO^+(1–0), CS(2–1)) PPV cubes for all galaxies. At first, we convolve the data cubes to the target resolution using the respective cloud-scale resolution for the CO(2–1) data and the kpc-scale resolution for the CO(2–1) and HCN(1–0) (HCO^+(1–0), CS(2–1)) cubes. Then, we put the voxels on hexagonal grids, using one sample per beam (full width at half-maximum – FWHM) for the kpc-scale maps, and two samples per beam (FWHM) for the cloud-scale maps. We use a higher sampling rate (satisfying the Nyquist–Shannon sampling theorem) for the cloud-scale maps in order to avoid losing information in computing the weighted averages (see Section 4.4). After conducting the weighted averages, we resample to match the kpc-resolution maps that are sampled at the beam size to get statistically independent data points for further processing.

We use the CO(2–1) data to create PPV masks, where we apply customized scripts that have been utilized in previous large program studies (e.g. EMIR Multi-Line Probe of the ISM Regulating Galaxy Evolution – EMPIRE; Jiménez-Donaire et al. 2019) and is based on the methodology introduced by Rosolowsky & Leroy (2006). We first identify pixels with high S/N (S/N $\geq$ 4) in at least three adjacent velocity channels. In addition, we build a low S/N mask requiring at least three adjacent velocity channels with S/N $\geq$ 2. Then we iteratively grow the identified high-S/N regions to include adjoining regions with moderate S/N as defined by the low-S/N mask. In doing so, we recover the more extended 2σ detection belonging to a 4σ core and thus recover regions of bright CO emission that one would also identify by eye. Finally, we collapse the masked data cubes along the velocity axis by summing the mask-selected channels (in K) multiplied by the channel width (in km s^{-1}) to produce integrated intensity maps (in K km s^{-1}).

We extract the HCN (analogously with HCO^+ and CS) emission via the CO-based PPV masks and produce the integrated intensity maps as described above. CO(2–1) is easy to excite and the brightest line observed here, being detected with a much higher S/N compared to the faint dense gas tracers, e.g. HCN. As such, CO emission unveils the regions of molecular gas where we also expect to find emission of the dense molecular gas as traced by HCN(1–0) (or HCO^+(1–0), CS(2–1)).

For each line of sight (LOS), we compute the statistical uncertainties in the integrated intensity $\sigma_{\rm I}$ from the rms in the emission-free (not selected by the mask) channels via

$$\left(\frac{\sigma_{\rm I}}{\rm K\,km\,s^{-1}}\right) = \left(\frac{\rm rms}{\rm K}\right)\left(\frac{\Delta v_{\rm channel}}{\rm km\,s^{-1}}\right)\sqrt{N}, \tag{11}$$

where $\Delta v_{\rm channel}$ is the channel width and N is the number of mask-selected voxels along the LOS.

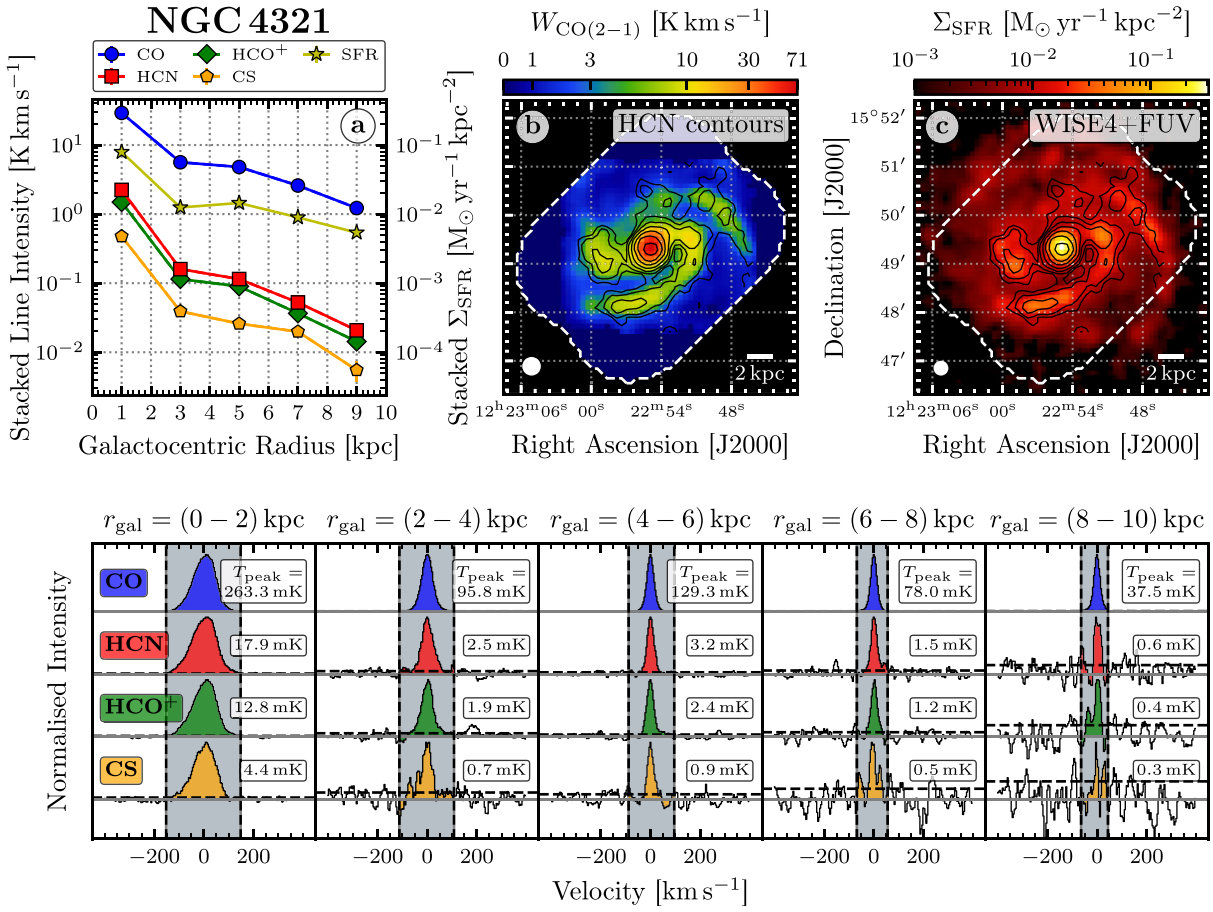

Figure 3. Spectral stacking across NGC 4321. (a) Integrated intensities of radially stacked spectra in bins of $r_{gal} = 2$ kpc. Shown are CO(2–1) from PHANGS–ALMA (Leroy et al. 2021b), HCN(1–0), HCO^+(1–0), and CS(2–1) from ALMOND (this work), and SFR surface density from z = 0 Multiwavelength Galaxy Synthesis (z0MGS; Leroy et al. 2019). Solid points indicate significant data (S/N > 3). (b) CO(2–1) moment-0 map, computed as described in Section 4.1, overlaid with HCN(1–0) contours in S/N levels of 2^n for $n \in \{0, 1, 2, ..., 7\}$, both at a common spatial resolution of 19.7 arcsec. (c) SFR map at 15 arcsec resolution, computed as described in Section 3.2 from a linear combination of the *WISE4*-IR and *GALEX*-FUV data. Bottom: stacked spectra, obtained as described in Appendix B corresponding to the integrated intensities shown in panel (a). The grey shaded area indicates the velocity-integration mask. The spectra are normalized by their peak intensity for each bin and each line individually. The respective peak intensities (measured inside the integration mask) are shown in the box next to each spectra. The horizontal dotted line indicates the rms, i.e. the standard deviation of the spectrum outside the integration mask. We made the above plot for all 25 galaxies available online.

4.2 kpc-scale dense gas properties

4.2.1 Dense gas fraction

In Sections 5 and 6, we focus on the observed ratio $W_{HCN}/W_{CO(2-1)}$, which we expect to be sensitive to density with some additional dependence on physical parameters like abundances, temperature, and opacities. In the Discussion section we also comment on implications for the actual dense gas fraction (f_{dense}), which is a simple recasting of this ratio using common mass-to-light ratios for both lines. We compute f_{dense} as the ratio of the dense gas surface density (Σ_{dense}) and the molecular gas surface density (Σ_{mol}) that is traced by $W_{HCN}/W_{CO(2-1)}$:

$$f_{dense} = \frac{\Sigma_{dense}}{\Sigma_{mol}} = \frac{\alpha_{HCN} W_{HCN}}{\alpha_{CO} R_{21}^{-1} W_{CO(2-1)}} \approx 2.1 \frac{W_{HCN}}{W_{CO(2-1)}}. \quad (12)$$

The kpc-scale integrated intensity maps are obtained as described in Section 4.1. Σ_{mol} is measured via $W_{CO(2-1)}$ assuming a constant mass-to-light ratio $\alpha_{CO} = 4.3\,M_\odot\,pc^{-2}\,(K\,km\,s^{-1})^{-1}$ (Bolatto, Wolfire & Leroy 2013) and a CO(2–1)-to-CO(1–0) line ratio of $R_{21} = 0.64$ (den Brok et al. 2021; Leroy et al. 2022). For more details on α_{CO} and R_{21}, see Section 4.3.1. Similarly, Σ_{dense} is obtained via W_{HCN} adopting a more uncertain $\alpha_{HCN} \approx 14\,M_\odot\,pc^{-2}\,(K\,km\,s^{-1})^{-1}$ (uncertain by at least ∼0.3 dex) tracing gas above $n_{H_2} \approx 5 \times 10^3\,cm^{-3}$ (Onus et al. 2018). For comparison, but not used in this work, previous studies assumed a lower value of $\alpha_{HCN} \approx 10\,M_\odot\,pc^{-2}\,(K\,km\,s^{-1})^{-1}$ and that HCN traces gas above a higher density of $3 \times 10^4\,cm^{-3}$ (following Gao & Solomon 2004, also see Jones et al. 2022).

4.2.2 Dense gas star formation efficiency

We compute the star formation efficiency of the dense gas via the ratio of SFR surface density and dense gas surface density:

$$SFE_{dense} = \frac{\Sigma_{SFR}}{\Sigma_{dense}} = \alpha_{HCN}^{-1} \frac{\Sigma_{SFR}}{W_{HCN}}. \quad (13)$$

Note that here Σ_{mol}, Σ_{SFR}, and Σ_{dense} are not corrected for the galaxies' inclinations because we are only interested in the ratio of surface densities such that the deprojection term $\cos i$ cancels out. For typical units and by adopting $\alpha_{HCN} \approx 14\,M_\odot\,pc^{-2}\,(K\,km\,s^{-1})^{-1}$

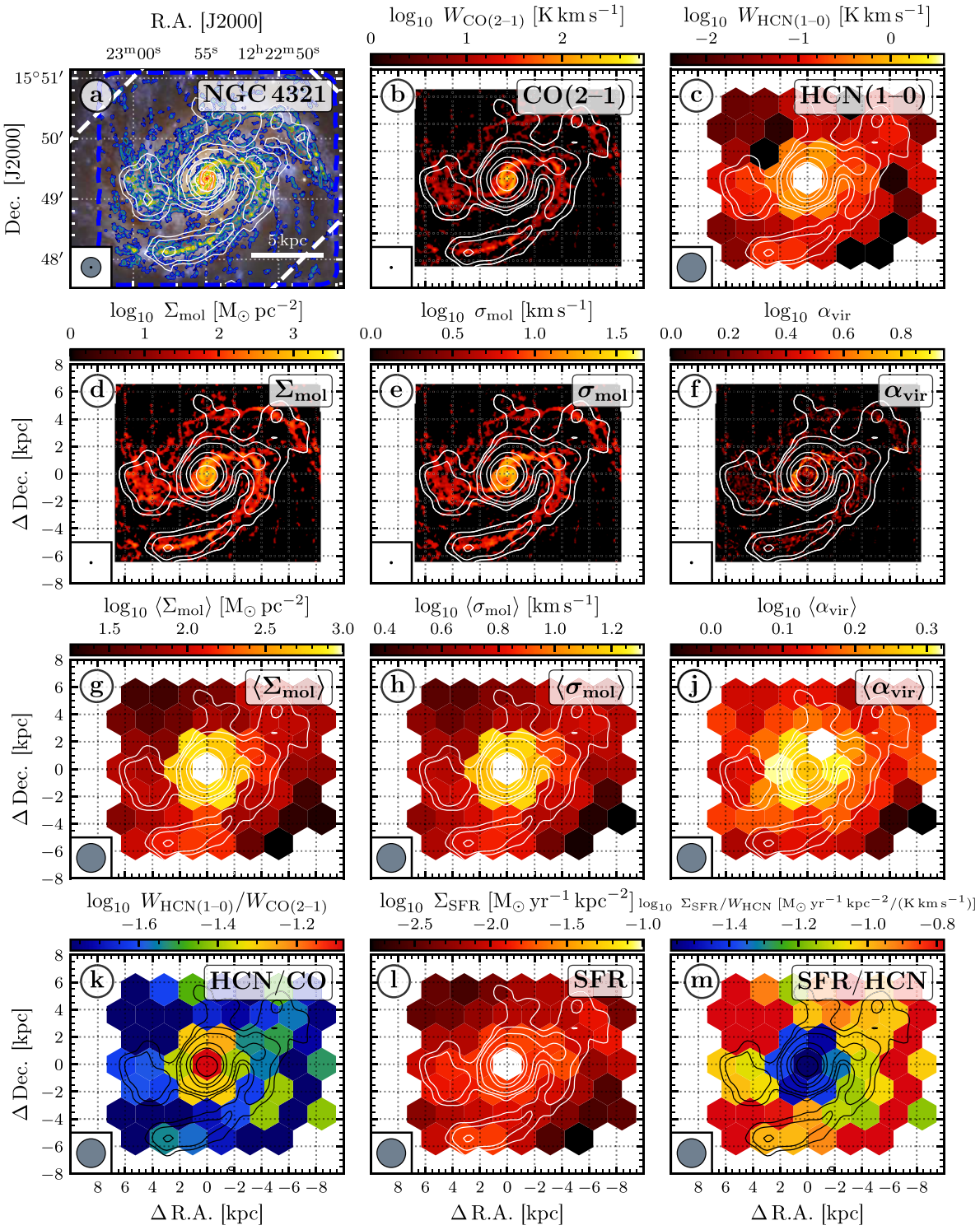

Figure 4. Data products compilation of NGC 4321 (one of the deepest observations) at cloud- and kpc-scale resolutions 150 pc and 2.1 kpc, respectively. (a) ESO three-colour image composed of 648 nm (red), 544 nm (green), and 433 nm (blue) wideband emission (image credit: ESO/IDA/Danish 1.5 m/R. Gendler, J.-E. Ovaldsen, C. C. Thöne, and C. Féron). Overlaid are coloured CO(2–1) contours and white HCN(1–0) contours, respectively, in S/N levels of 3, 5, 10, 30, 50, 100, 300 (the same HCN contours are used throughout the other maps). The white and blue dashed contour indicate the ALMOND and PHANGS–ALMA FOV, respectively. (b) Integrated CO(2–1) intensity at 150 pc resolution from PHANGS–ALMA. (c) Integrated HCN(1–0) intensity at 2.1 kpc resolution from ALMOND as obtained from the data cubes according to Section 4.1. (d)–(f) cloud-scale properties of the molecular gas (molecular gas surface density $\Sigma_{\rm mol}$, velocity dispersion $\sigma_{\rm mol}$, and virial parameter $\alpha_{\rm vir}$) computed from CO(2–1) as described in Section 4.3. (g)–(i) CO(2–1) intensity weighted averages $\langle\Sigma_{\rm mol}\rangle$, $\langle\sigma_{\rm mol}\rangle$, $\langle\alpha_{\rm vir}\rangle$ of the above cloud-scale properties based on the formalism described in Section 4.4. (k) HCN/CO tracing $f_{\rm dense}$. (l) SFR surface density from FUV (*GALEX*). (m) IR (*WISE*) and SFR/HCN tracing $\rm SFE_{dense}$ following Section 4.2.

like in Section 4.2.2, above equation (13) becomes

$$\left(\frac{\mathrm{SFE}_{\mathrm{dense}}}{\mathrm{Myr}^{-1}}\right) = 7.1 \times 10^{-1} \left(\frac{\Sigma_{\mathrm{SFR}}}{\mathrm{M}_{\odot}\,\mathrm{yr}^{-1}\,\mathrm{kpc}^{-2}}\right) \left(\frac{W_{\mathrm{HCN}}}{\mathrm{K\,km\,s}^{-1}}\right)^{-1}. \tag{14}$$

4.3 Cloud-scale molecular gas properties

We compute the four cloud-scale properties molecular gas surface density (Σ_{mol}), velocity dispersion (σ_{mol}), virial parameter (α_{vir}), and internal turbulent pressure (P_{turb}) using PHANGS–ALMA CO(2–1) data (see Section 3.1.1) following Sun et al. (2018). We measure the cloud-scale properties at beam sizes of 150 pc using pixel-by-pixel values instead of identifying individual molecular clouds. Based on comparisons of the two approaches by Sun et al. (2020b) and Rosolowsky et al. (2021), statistically we expect similar results for the molecular gas properties as measured at cloud-scale compared to cloud properties as obtained for individually identified clouds. In Appendix F, we also discuss subsamples, where we have access to higher resolutions, i.e. 75 pc for five galaxies and 120 pc for 12 galaxies, respectively. We confirm that the results do not significantly depend on the resolution at which the cloud-scale properties are measured.

4.3.1 Molecular gas surface density

We trace Σ_{mol} at 150 pc resolution via $W_{\mathrm{CO(2-1)}}$ using a constant mass-to-light ratio conversion factor:

$$\Sigma_{\mathrm{mol}} = \alpha_{\mathrm{CO}}\, R_{21}^{-1}\, W_{\mathrm{CO(2-1)}}. \tag{15}$$

We adopt a constant, MW-like CO-to-H_2 conversion factor of $\alpha_{\mathrm{CO}} = 4.3\,\mathrm{M}_{\odot}\,\mathrm{pc}^{-2}\,(\mathrm{K\,km\,s}^{-1})^{-1}$ (uncertainty of ± 0.1 dex) as suggested by Bolatto et al. (2013) and a constant CO(2–1)-to-CO(1–0) line ratio of $R_{21} = 0.64$ (uncertainty of ± 0.06 dex) as recently constrained by den Brok et al. (2021) and for a larger sample including many of these targets by Leroy et al. (2022), which yields

$$\left(\frac{\Sigma_{\mathrm{mol}}}{\mathrm{M}_{\odot}\,\mathrm{pc}^{-2}}\right) = 6.7 \times 10^{2} \left(\frac{W_{\mathrm{CO(2-1)}}}{10^{2}\,\mathrm{K\,km\,s}^{-1}}\right). \tag{16}$$

Note that some of the α_{CO} and R_{21} uncertainty can be attributed to variations as a function of the galactocentric radius, where α_{CO} is found to be lower in the centres of galaxies (Sandstrom et al. 2013), while R_{21} is higher towards galaxy centres (den Brok et al. 2021). To account for systematic variations of α_{CO} with metallicity Z',[6] recent studies (as in Sun et al. 2020b) adopt a metallicity-dependent $\alpha_{\mathrm{CO}} \propto Z'^{-1.6}$, which leads to lower α_{CO} in the central region of galaxies. However, metallicity variations can only partly explain the low α_{CO} in centres. Sandstrom et al. (2013) conclude that the physical conditions in the centres of galaxies (ISM pressure, gas temperature) are responsible for lowering α_{CO} by roughly a factor of 2. Thus, by adopting a constant α_{CO}, we may overestimate Σ_{mol} in the central regions of galaxies and underestimate Σ_{mol} at larger galactocentric radii. We still adopt a constant α_{CO} in analogy to previous studies (e.g. Gallagher et al. 2018a,b; Sun et al. 2018) and discuss in Section 6.1 how lowering α_{CO} by a factor of 2 in the centres of galaxies affects the studied relations.

[6] Z' is the metallicity normalized to the solar metallicity [$12 + \log_{10}(\mathrm{O/H}) = 8.69$] (Allende Prieto, Lambert & Asplund 2001).

4.3.2 Velocity dispersion

We characterize the line width using the 'effective width' according to the prescription of Heyer, Carpenter & Snell (2001), calculated via

$$\sigma_{\mathrm{measured}} = \frac{W_{\mathrm{CO(2-1)}}}{\sqrt{2\pi}\,T_{\mathrm{peak}}}, \tag{17}$$

where T_{peak} (in units of K) is obtained as the maximum intensity of the cubes' spectra for each LOS. Then, for a Gaussian line profile with peak intensity T_{peak} the effective width is equal to the rms velocity dispersion of the line (σ_{mol}). In order to correct for the line broadening caused by the instrument (finite channel width, spectral response curve width), we subtract the contribution of the instrument's response following Rosolowsky & Leroy (2006) and Sun et al. (2018):

$$\sigma_{\mathrm{mol}} = \sqrt{\sigma^2_{\mathrm{measured}} - \sigma^2_{\mathrm{response}}}. \tag{18}$$

Here, $\sigma_{\mathrm{response}}$ is estimated from the channel width and the channel-to-channel correlation coefficient, following Leroy et al. (2016) and Sun et al. (2018).

4.3.3 Virial parameter

The virial parameter of GMCs is typically defined as $\alpha_{\mathrm{vir}} \equiv 2K/U_{\mathrm{g}}$, where K is the kinetic energy and U_{g} is its self-gravitational potential energy of the cloud such that α_{vir} quantifies deviations from virial equilibrium. Virialized clouds have $\alpha_{\mathrm{vir}} = 1$, if surface pressure or magnetic support can be neglected. For unbound clouds α_{vir} moves to higher values.

Following Bertoldi & McKee (1992), under the assumption of spherical clouds, the virial parameter can be expressed as[7]

$$\alpha_{\mathrm{vir}} \equiv \frac{2K}{U_{\mathrm{g}}} = \frac{5\sigma^2_{\mathrm{mol}} R}{fGM}, \tag{19}$$

where M, R, and σ_{mol} are the cloud's mass, radius, and velocity dispersion, G is the gravitational constant, and f is a geometrical factor specifying the density profile of the cloud. We adopt $f = 10/9$ that assumes a density profile of the form $\rho \propto r^{-1}$ (e.g. following Rosolowsky & Leroy 2006). Given that the cloud-scale resolutions are at the scale of GMCs we take the beam size as the relevant size scale ($R = D_{\mathrm{beam}}/2$), such that equation (19) implies

$$\alpha_{\mathrm{vir}} = \frac{5}{2fG} \frac{\sigma^2_{\mathrm{mol}} D_{\mathrm{beam}}}{\Sigma_{\mathrm{mol}} A_{\mathrm{beam}}} = \frac{10 \ln 2}{\pi f G} \frac{\sigma^2_{\mathrm{mol}}}{\Sigma_{\mathrm{mol}} D_{\mathrm{beam}}}. \tag{20}$$

Here, Σ_{mol} is the molecular gas surface density, computed in Section 4.3.1, σ_{mol} is the velocity dispersion (see Section 4.3.2), and D_{beam} is the FWHM of the beam, i.e. 150 pc. Normalizing by typical numbers, we obtain

$$\alpha_{\mathrm{vir}} = 3.1 \left(\frac{\Sigma_{\mathrm{mol}}}{10^{2}\,\mathrm{M}_{\odot}\,\mathrm{pc}^{-2}}\right)^{-1} \left(\frac{\sigma_{\mathrm{mol}}}{10\,\mathrm{km\,s}^{-1}}\right)^{2} \left(\frac{D_{\mathrm{beam}}}{150\,\mathrm{pc}}\right)^{-1}. \tag{21}$$

Note that above formalism is likely to produce uncertainties in α_{vir} reaching factors of a few. However, following the approach of e.g. Sun et al. (2018, 2020b), we are interested in measuring $\sigma^2_{\mathrm{mol}}/\Sigma_{\mathrm{mol}}$ for comparative analysis and consider it as a tracer of α_{vir}, where the conversion factor is uncertain by a factor of a few. In other words, we measure α_{vir} in units of $\sigma^2_{\mathrm{mol}}/\Sigma_{\mathrm{mol}}$ for fixed physical scale.

[7] Note that this approach neglects contributions from the magnetic energy density or the cosmic ray flux. Moreover, it ignores any surface terms (see e.g. McKee & Zweibel 1992; Ballesteros-Paredes 2006).

4.3.4 Internal turbulent pressure

We infer the internal turbulent pressure, $P_{\rm turb}$, from the CO(2–1) observations. Following Sun et al. (2018), the internal pressure in molecular gas with LOS depth $\sim 2R$ can be expressed as

$$P_{\rm turb} \approx \rho_{\rm mol}\sigma^2_{\rm mol} \approx \frac{1}{2R}\Sigma_{\rm mol}\sigma^2_{\rm mol}. \tag{22}$$

Similar to the virial parameter computation in Section 4.3.3, we aim to measure the quantity $\Sigma_{\rm mol}\sigma^2_{\rm mol}$ in order to trace $P_{\rm turb}$ at a scale of $R = D_{\rm beam}/2$ with the purpose of comparative analysis. $P_{\rm turb}$ is linked to $\Sigma_{\rm mol}\sigma^2_{\rm mol}$ via a proportionality factor:

$$\left(\frac{P_{\rm turb}}{k_{\rm B}\,{\rm K\,cm^{-3}}}\right) \approx 3.3\times10^5 \left(\frac{\Sigma_{\rm mol}}{10^2\,{\rm M_\odot\,pc^{-2}}}\right) \times \left(\frac{\sigma_{\rm mol}}{10\,{\rm km\,s^{-1}}}\right)^2 \left(\frac{D_{\rm beam}}{150\,{\rm pc}}\right)^{-1}, \tag{23}$$

where $\Sigma_{\rm mol}$ and $\sigma_{\rm mol}$ are taken from Sections 4.3.1 and 4.3.2, respectively.

4.4 Weighted averages

In order to connect the cloud-scale – $\Sigma_{\rm mol}$, $\sigma_{\rm mol}$, $\alpha_{\rm vir}$, and $P_{\rm turb}$ – measurements to the kpc-scale – $f_{\rm dense}$ and $\rm SFE_{dense}$ – measurements, we calculate the intensity-weighted averages of $\Sigma_{\rm mol}$, $\sigma_{\rm mol}$, $\alpha_{\rm vir}$, and $P_{\rm turb}$ inside each kpc-scale beam. These weighted averages – $\langle\Sigma_{\rm mol}\rangle$, $\langle\sigma_{\rm mol}\rangle$, $\langle\alpha_{\rm vir}\rangle$, and $\langle P_{\rm turb}\rangle$ – measure the cloud-scale $\Sigma_{\rm mol}$, $\sigma_{\rm mol}$, $\alpha_{\rm vir}$, and $P_{\rm turb}$, respectively, from which the average CO photon emerges within the kpc-scale resolution beam. In practice we compute (following Leroy et al. 2016)

$$\langle X\rangle = \frac{(X\,W_{\rm CO(2-1)})*\Omega}{W_{\rm CO(2-1)}*\Omega}. \tag{24}$$

Here, $W_{\rm CO(2-1)}$ is the CO(2–1) integrated intensity and X is the quantity to be averaged, both at cloud-scale resolution (in this work, 150 pc). X is weighted with $W_{\rm CO(2-1)}$ (via multiplication) and convolved to the kpc-scale resolution (here, 2.1 kpc) indicated by the asterisk using a Gaussian kernel Ω. Finally, the weighted average, $\langle X\rangle$, is obtained by division with the convolved weights. Consequently, $\langle X\rangle$ is at kpc-scale resolution and can easily be compared to the kpc-scale $f_{\rm dense}$ and $\rm SFE_{dense}$ measurements pixel-by-pixel.

The above formalism was introduced by Leroy et al. (2016) and is designed to connect high-resolution to low-resolution measurements such as conducted in this study, having the advantage of preserving the high-resolution information and downweighting empty regions. As such it was utilized by e.g. Gallagher et al. (2018b) who performed a similar comparison as the one presented in this work. Sun et al. (2020a) computed the weighted averages in terms of equation (24) applying a top-hat kernel to the cloud-scale data and then computed the weighted averages in each of these apertures. Here, we follow the Gaussian convolution approach using equation (24) in order to make the weighted averages similarly comparable to the kpc-scale observations. We highlight the difference between the two approaches in the Appendix C.

We estimate the propagated uncertainties in the weighted averages via Monte Carlo computations. We start with the $\Sigma_{\rm mol}$, $\sigma_{\rm mol}$, $\alpha_{\rm vir}$, and $P_{\rm turb}$ maps, add random Gaussian noise with amplitudes taken from the cloud-scale maps. Then we run the noise-added maps through the weighted averages procedure and repeat this process 100 times. Finally, we take the standard deviation in $\langle\Sigma_{\rm mol}\rangle$, $\langle\sigma_{\rm mol}\rangle$, $\langle\alpha_{\rm vir}\rangle$, and $\langle P_{\rm turb}\rangle$ over all realizations as the uncertainty estimate.

4.5 Data binning

We detect integrated HCN intensity (analogously for $\rm HCO^+$ and CS) with S/N ≥ 3 only in the brightest regions of the galaxies. In order to recover the low S/N information hidden in the data, we bin the HCN data by $\langle\Sigma_{\rm mol}\rangle$, or equivalently $\langle W_{\rm CO(2-1)}\rangle$ (following Gallagher et al. 2018a). $\langle\Sigma_{\rm mol}\rangle$ is detected at high significance across much of the galaxy discs in all 25 targets.

We bin each galaxy's data individually, choosing a fixed number of 20 bins, equally spaced in $\langle\Sigma_{\rm mol}\rangle$, over the full data range of each galaxy. Adapting the binning to each galaxy individually allows us to recover more of the low S/N signal. We choose the number of 20 bins because it increases the number of HCN detections at low $\langle\Sigma_{\rm mol}\rangle$ without averaging over too large intervals thus maximizing the dynamic range in the x-axis variable ($\langle\Sigma_{\rm mol}\rangle$). In each bin, we compute the binned ratio – $W_{\rm HCN}/W_{\rm CO(2-1)}$ or $\Sigma_{\rm SFR}/W_{\rm HCN}$ – as the mean of the nominator's data in that bin divided by the mean of the denominator's data in that bin (as in Schruba et al. 2011; Jiménez-Donaire et al. 2017):

$$\left.\frac{W_{\rm HCN}}{W_{\rm CO(2-1)}}\right|_{\rm bin} = \frac{\rm mean(W_{HCN})|_{bin}}{\rm mean(W_{CO(2-1)})|_{bin}}, \tag{25}$$

$$\left.\frac{\Sigma_{\rm SFR}}{W_{\rm HCN}}\right|_{\rm bin} = \frac{\rm mean(\Sigma_{SFR})|_{bin}}{\rm mean(W_{HCN})|_{bin}}. \tag{26}$$

This means that for each bin we take the ratio of the bin means and not the bin mean of the ratios. The binning process extends the dynamic range of significant HCN data and has the advantage of reducing the linear regression bias that is naturally induced by converting from linear to logarithmic scale (for more details see Appendix D).

We propagate the measurement uncertainties from the individual integrated intensity (and SFR) data points that enter the binning using Gaussian error propagation. As we sample the integrated intensities at the beam size (one sample per beam FWHM), we do not need to account for oversampling in the error propagation. In doing so, for each bin the propagated uncertainty roughly decreases as $1/\sqrt{N}$, where N is the number of points in the bin. However, the binned measurements can often still have low S/N. Considering binned data detected if the S/N ≥ 3 and censored (non-detected) if S/N < 3, we can define upper and lower limits on the binned data. The binned integrated CO(2–1) intensities and SFR surface densities are significant (S/N ≥ 3) across the whole galactic disc for the full sample of galaxies. Thus, the S/N is purely dominated by the HCN data. Therefore, we define upper limits (UL) in the binned HCN/CO(2–1) data via

$${\rm UL}|_{\rm bin} = \frac{3\,I_{\rm HCN,\,unc}|_{\rm bin}}{W_{\rm CO(2-1)}|_{\rm bin}}, \tag{27}$$

where $I_{\rm HCN,\,unc}$ is the (propagated) uncertainty of the integrated HCN intensity in each bin. For SFR/HCN we compute lower limits (LL) via

$${\rm LL}|_{\rm bin} = \frac{\Sigma_{\rm SFR}|_{\rm bin}}{3\,I_{\rm HCN,\,unc}|_{\rm bin}}. \tag{28}$$

Although UL and LL are regarded (by definition) non-significant, they are still an important part of the data distribution and we use them in our linear regression analysis (Section 4.6).

4.6 Linear regression and correlation

To investigate the correlations we fit a linear regression model to the log-scale binned data, resulting from the data processing described above (Section 3). We perform the linear regression by making use

of the LINMIX package[8] that is based on the Bayesian approach to linear regression proposed by Kelly (2007). In this approach, a likelihood function of the linear regression model is built and Markov chain Monte Carlo (MCMC) simulations are run using a Gibbs sampler exploring the posterior distribution of the regression parameters. Here, we force the MCMC simulation to take at least 10 000 steps after convergence was reached, i.e. close to the global maximum of the posterior distribution where every iteration can be considered a random draw from the posterior. The model accounts for heteroscedastic uncertainties in the data on both coordinates, intrinsic scatter and censored data, i.e. upper (or lower) limits in the independent variable.[9] Because of its statistical nature in exploring the parameter space, it naturally provides trustworthy uncertainty estimates and credibility intervals of the regression parameters. Moreover, it computes the Pearson correlation coefficient ρ (and the p-value) using both detected and censored data. We choose this linear regression method because it accounts for non-detections, determines meaningful fit uncertainties, and leads to less biased regression parameter estimates (see Appendix D).

We perform the linear regression by fitting the following linear function to the data in log–log scale:

$$\log_{10} Y = b_{y,x} + m_{y,x} \left[\log_{10} \langle X \rangle - x_{\mathrm{off,x}}\right], \tag{29}$$

where Y are the kpc-scale measurements (HCN/CO or SFR/HCN) and $\langle X \rangle$ are the weighted averages of the cloud-scale molecular gas properties (Σ_{mol}, σ_{mol}, and P_{turb})[10] in their respective units. $b_{y,x}$ and $m_{y,x}$ are the intercept and slope of the fit line, where $y = \{f, S\}$, $x = \{\Sigma, \sigma, P\}$ indicate the corresponding kpc-scale (HCN/CO, SFR/HCN) and cloud-scale quantities (Σ_{mol}, σ_{mol}, and P_{turb}). We recentre the distribution in the x-axis coordinate to minimize the covariance between the slope and intercept, applying $x_{\mathrm{off},x} \equiv \{2.5, 1.1, 6.5\}$ for $x = \{\Sigma, \sigma, P\}$ which is near the middle of the data range. Note that this has no effect on the fitting scheme. In addition, we compute the scatter of the data about the best-fitting line as the standard deviation of the fit residuals, i.e. the standard deviation in the y-axis data after the fit line has been removed. Here, we only consider significant data (S/N $\geq$ 3) and give the scatter in units of dex.

5 RESULTS

In Section 5.1, we present the dense gas-star formation law (Fig. 5). Next, being the main result of this work, we analyse the dependence of the ratios $W_{\mathrm{HCN}}/W_{\mathrm{CO(2-1)}}$ (hereafter HCN/CO) and $\Sigma_{\mathrm{SFR}}/W_{\mathrm{HCN}}$ (hereafter SFR/HCN) as a function of the cloud-scale molecular gas properties Σ_{mol}, σ_{mol}, α_{vir}, and P_{turb}. HCN/CO is used as a proxy for the dense gas fraction (f_{dense}) and SFR/HCN as a proxy for the star formation efficiency of the dense gas ($\mathrm{SFE}_{\mathrm{dense}} = \mathrm{SFR}/M_{\mathrm{dense}}$), both at 2.1 kpc physical scale, albeit with some important caveats (see Sections 2.3 and 4.2.1), The cloud-scale properties are inferred from the CO(2–1) measurements at a fixed physical scale of 150 pc. We use the CO(2–1) intensity to trace Σ_{mol} and the CO(2–1) line width to trace σ_{mol}. We trace α_{vir} and P_{turb} via $\sigma^2_{\mathrm{mol}}/\Sigma_{\mathrm{mol}}$ and $\sigma^2_{\mathrm{mol}}\Sigma_{\mathrm{mol}}$, respectively (Section 4.3). Fig. 6 shows the observed relationships. The upper panels show the HCN/CO correlations with the three molecular cloud properties (Σ_{mol}, σ_{mol}, and α_{vir}) from left to right, which are discussed in Section 5.2. Similarly, the lower panels display the SFR/HCN correlations discussed in Section 5.3. For each relation we perform linear regression fitting to the data in logarithmic scale as described in Section 4.6. Moreover, we determine the Pearson correlation and corresponding p-value and compute the scatter in the fit residuals.

In addition, we examine the impact of resolution in Appendix F and find consistent results across all adopted resolutions, i.e. varying cloud-scale and kpc-scale from 75 to 150 pc and 1.0 to 2.1 kpc, respectively. Moreover, we show the same relationships taking $\mathrm{HCO^+}$(1–0) or CS(2–1) as a tracer of the denser molecular gas (see Appendices G and H).

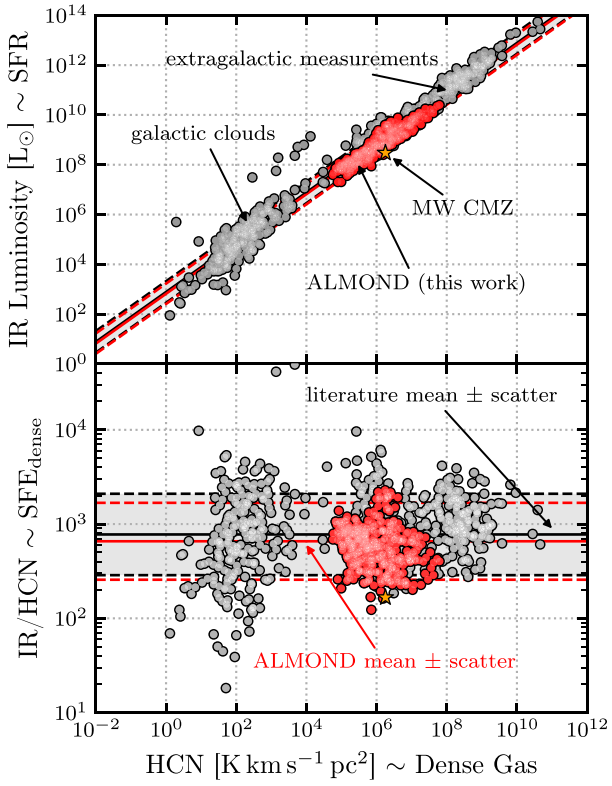

Figure 5. Relation between (total) IR luminosity, tracing SFR, and HCN(1–0) luminosity, tracing dense gas mass. We show our new ALMOND data, where S/N $\geq$ 5 along with MW clouds (Wu et al. 2010; Stephens et al. 2016), the CMZ, GMCs in the Small Magellanic Cloud (SMC), Large Magellanic Cloud (LMC), and other low-metallicity environments (Chin et al. 1997, 1998; Braine et al. 2017) and GMCs in other galaxies (Brouillet et al. 2005; Buchbender et al. 2013; Chen et al. 2017). Furthermore, we add other extragalactic observations, i.e. resolved nearby galaxy discs (Kepley et al. 2014; Bigiel et al. 2015; Chen et al. 2015; Usero et al. 2015; Gallagher et al. 2018a) and whole galaxies (Gao & Solomon 2004; Gao et al. 2007; Graciá-Carpio et al. 2008; Krips et al. 2008; Juneau et al. 2009; García-Burillo et al. 2012; Privon et al. 2015). The solid black line indicates the mean SFR/HCN of $10^{2.89}\,\mathrm{L_\odot\,(K\,km\,s^{-1})^{-1}\,pc^{-2}}$ from Jiménez-Donaire et al. (2019) over their literature compilation, with the dashed lines showing the scatter of ±0.37 dex. In addition, we show the mean ($10^{2.82}\,\mathrm{L_\odot\,(K\,km\,s^{-1})^{-1}\,pc^{-2}}$) and scatter (±0.41 dex) computed from the significant (S/N $\geq$ 5) ALMOND data.

[8] https://linmix.readthedocs.io/en/latest/index.html

[9] Note that LINMIX can also account for the covariance between uncertainties in the x- and y-axis coordinates. One may expect that the uncertainties of HCN/CO and $\langle \Sigma_{\mathrm{mol}} \rangle$ are correlated since both axis depend on the CO(2–1) measurements. However, the HCN/CO uncertainties are completely dominated by the HCN(1–0) measurement uncertainties. Therefore, the uncertainties between the axes show no significant correlation and we neglect the covariance term in the fitting scheme.

[10] We skip α_{vir} here, because we do not find any significant correlation with α_{vir} and thus do not perform the linear regression.

5.1 Dense gas star formation relation

In Fig. 5, we show the relation between HCN luminosity and total IR luminosity, measured at the native resolution of the HCN observations, as has been reported in many previous works (e.g. Lada & Lada 2003; Gao & Solomon 2004; Jiménez-Donaire et al. 2019). We inferred the total IR (TIR) luminosity from the SFR maps using the following equation (Murphy et al. 2011):

$$\frac{\Sigma_{\rm SFR}}{\rm M_\odot\,yr^{-1}\,kpc^{-2}} = 1.48\times10^{-10}\,\frac{\Sigma_{\rm TIR}}{\rm L_\odot\,kpc^{-2}}. \quad (30)$$

Overall, our HCN and SFR measurements are in agreement with previous works confirming the, to zeroth-order, linear relation between HCN inferred dense gas mass and IR inferred SFR. Certainly, our data are on average 0.07 dex lower than the mean value of $\rm SFE_{dense} = 776\,L_\odot\,(K\,km\,s^{-1})^{-1}\,pc^{-2}$ reported by Jiménez-Donaire et al. (2019) and in fact consistent with the low $\rm SFE_{dense}$ found in the MW's CMZ.

5.2 HCN/CO versus molecular cloud properties

5.2.1 HCN/CO versus molecular gas surface mass density

Assuming that cloud-scale surface density traces mean volume density, we expect a positive correlation between the surface density of the molecular cloud ($\Sigma_{\rm mol}$) and the HCN/CO line ratio as laid out in Section 2.4. The upper left-hand panel of Fig. 6 shows the observed relationship between HCN/CO and $\langle\Sigma_{\rm mol}\rangle$ (significant data points and upper limits). The underlying red shaded region shows the model expectations that are in good agreement with the data if shifted by −1.0 dex in HCN/CO. At lower $\langle\Sigma_{\rm mol}\rangle$, the model produces a steeper relation than the data. This discrepancy is expected and can be attributed to the simplified model, which does not account for systematic variations of the HCN emission as a function of the cloud density (see Section 2.4). Our model does not take into account the CO(2–1) or HCN(1–0) light-to-mass conversion factors $\alpha_{\rm CO(2-1)}$ and $\alpha_{\rm HCN}$, respectively. Hence, the employed shift would imply a ratio between the conversion factors of $\alpha_{\rm HCN}/\alpha_{\rm CO(2-1)} \sim 10$. In agreement with the model expectations and expanding the results by Gallagher et al. (2018b), we find a strong positive correlation between HCN/CO and $\langle\Sigma_{\rm mol}\rangle$ (see Fig. 6) with Pearson correlation coefficient $\rho = 0.88$ (p-values smaller than 10^{-5}) and a linear regression slope of $m_{\rm f,\,\Sigma} = 0.35 \pm 0.02$. We find small scatter of 0.11 dex about the fit line pointing towards a tight correlation.

For subsamples of galaxies, where higher resolutions (i.e. 120, 75 pc cloud-scale and 1.5, 1.0 kpc averaging-scale) can be accessed, we find comparable correlations with $\rho = 0.88$–0.97, $m_{\rm f,\,\Sigma} = 0.35$–$0.49$ (see Appendix F1). In general, we find that the derived relationship can change significantly depending on which galaxies are included in the sample. However, for a fixed sample of galaxies the correlations are consistent for different resolutions, where smaller scales seem to show steeper slopes (a more detailed discussion is found in Appendix F1).

5.2.2 HCN/CO versus velocity dispersion

Similar to the HCN/CO versus $\Sigma_{\rm mol}$ correlation, turbulent cloud models predict a positive correlation between HCN/CO and $\sigma_{\rm mol}$ assuming the effective line width traces the turbulent Mach number (see Section 2.4). Consistent with the model expectations, we report a positive correlation between HCN/CO and $\langle\sigma_{\rm mol}\rangle$ with Pearson correlation coefficient $\rho = 0.85$ and small p-value $< 10^{-5}$. The regression slope is $m_{\rm f,\,\sigma} = 0.66 \pm 0.04$ and we find small scatter of 0.12 dex indicating a strong and tight correlation. Variations in the correlation at different resolutions (see Appendix F1) are consistent for the same sample of galaxies and follow similar systematics as seen for HCN/CO versus $\langle\Sigma_{\rm mol}\rangle$ that is expected due to the strong correlation between $\Sigma_{\rm mol}$ and $\sigma_{\rm mol}$ (see e.g. Sun et al. 2020b; Rosolowsky et al. 2021).

Tracing the velocity dispersion via the line width is appropriate for the discs of galaxies but may lead to biased estimates in the galactic centres (e.g. Henshaw et al. 2016). In Section 6.1, we additionally inspect the correlations for the central regions (defined as the central pixel of each galaxy, i.e. the inner ∼2.1 kpc) and the discs separately (the fit parameters are listed in Table 3). We find that the correlations as obtained from the central regions are slightly offset by <0.1 dex from the correlations associated with the discs suggesting that the kpc-scale centres are not statistically distinct to the discs.

5.2.3 HCN/CO versus virial parameter

As discussed in Section 2.4, the connection between HCN/CO and the virial parameter is complex. In the simple KM theory, $\alpha_{\rm vir}$ does not affect the PDF and thus keeps HCN/CO unchanged. However, the empirical $\alpha_{\rm vir}$ (equation 19), which assumes a fixed cloud size, correlates with $\sigma_{\rm mol}$ and anticorrelates with $\Sigma_{\rm mol}$ such that, given the observed cloud-scale properties, variations in $\alpha_{\rm vir} \propto \sigma^2_{\rm mol}/\Sigma_{\rm mol}$ might be correlated with HCN/CO as shown in Fig. 2.

In accordance with the model picture, we find a weak positive ($\rho = 0.21$, $p = 0.028$), but no significant correlation between HCN/CO and $\sigma^2_{\rm mol}/\Sigma_{\rm mol}$ tracing the virial parameter. Here, the correlation coefficient was computed using only the significant data points (i.e. where SNR ≥ 3, hence not including censored data as for $\Sigma_{\rm mol}$ or $\sigma_{\rm mol}$), because the fitting algorithm does not converge.

We consistently find positive correlation coefficients, spanning $\rho = 0.21$–0.77, at different resolutions that support a positive correlation between HCN/CO and $\sigma^2_{\rm mol}/\Sigma_{\rm mol}$, especially for individual galaxies (e.g. NGC 2903 or NGC 4321, which are also the ones with the highest S/N) and at smaller scales (75 pc cloud-scale and 1.0 kpc averaging-scale). However, including the complete sample of 25 galaxies, our data do not confidently suggest any correlation between HCN/CO and $\sigma^2_{\rm mol}/\Sigma_{\rm mol} \propto \alpha_{\rm vir}$.

5.2.4 HCN/CO versus internal turbulent pressure

The internal turbulent pressure, or equivalently the kinetic energy density, measures the turbulence of the gas, $\sigma^2_{\rm mol}$, weighted by the amount of molecular gas, $\Sigma_{\rm mol}$, so that $P_{\rm turb} \propto \Sigma_{\rm mol}\sigma^2_{\rm mol}$ (see equation 22). We have shown in Sections 5.2.1 and 5.2.2 that HCN/CO positively correlates with $\langle\Sigma_{\rm mol}\rangle$ and $\langle\sigma_{\rm mol}\rangle$. Thus, also agreeing with model predictions, we expect a positive correlation between HCN/CO and $\langle P_{\rm turb}\rangle$. The HCN/CO versus $P_{\rm turb}$ relation plot is not shown in Fig. 6 because it directly follows from and is almost identical to the $\Sigma_{\rm mol}$ and $\sigma_{\rm mol}$ relations. Though, the linear regression results are listed in Table I1 and the plot is shown in the Appendix F1.

As expected, we find a strong positive correlation between HCN/CO and $\langle P_{\rm turb}\rangle$ with correlation coefficient $\rho = 0.88$ and $p < 10^{-5}$ that are very similar to the correlation coefficients found for $\langle\Sigma_{\rm mol}\rangle$ ($\rho = 0.88$) and $\langle\sigma_{\rm mol}\rangle$ ($\rho = 0.85$). Though, the regression slope is small ($m_{\rm f,\,P} = 0.17 \pm 0.01$ due to the huge dynamic range in $\langle P_{\rm turb}\rangle$ spanning five orders of magnitude. The scatter in the correlation is small (0.11 dex) indicating a tight correlation. Variations in the correlations as a function of resolution configurations show similar trends as for $\langle\Sigma_{\rm mol}\rangle$ (Section 5.2.1) and $\langle\sigma_{\rm mol}\rangle$ (Section 5.2.2).

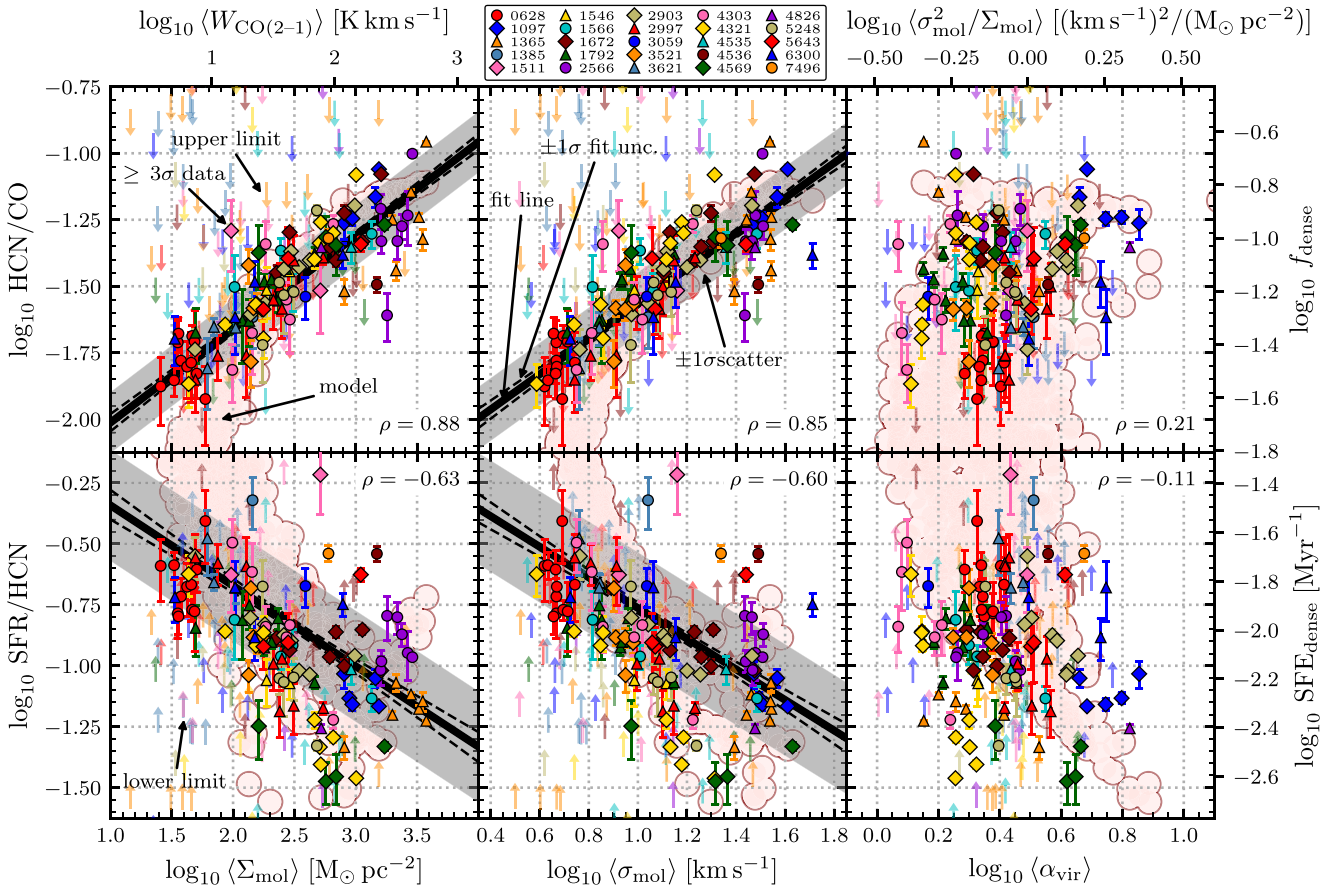

Figure 6. HCN/CO versus $\langle X \rangle$ and SFR/HCN versus $\langle X \rangle$ (cloud-scale = 150 pc, kpc-scale = 2.1 kpc). Top: HCN/CO as a proxy of dense gas fraction against molecular cloud properties ($\langle \Sigma_{\rm mol} \rangle$, $\langle \sigma_{\rm mol} \rangle$, and $\langle \alpha_{\rm vir} \rangle$) as obtained from CO(2–1) data from left to right. The data are binned according to Section 4.5. Filled points specify significant data with SNR(HCN/CO) ≥ 3 and downward pointing arrows indicate 3σ upper limits on HCN/CO. The thick solid line denotes the best-fitting linear regression, i.e. the median realization of the MCMC simulation. The dashed lines indicate the 1σ credibility interval of the MCMC realizations. The grey shaded area shows the scatter of the significant data about the fit line. For $\langle \alpha_{\rm vir} \rangle$ we do not observe a correlation and thus do not fit a line to the data. Bottom: analogous to the upper panels, SFR/HCN as a proxy of the star formation efficiency of the dense gas versus molecular cloud properties from left to right. Here, upward pointing arrows denote 3σ lower limits in SFR/HCN. Again, the linear regression to $\langle \alpha_{\rm vir} \rangle$ was not determined due to lack of correlation. The light red shaded areas show the model prediction, equivalent to the red data in Fig. 2, but shifted by −1.0 dex in HCN/CO and −0.6 dex in SFR/HCN to visually overlap with the observational results.

5.3 SFR/HCN versus molecular cloud properties

5.3.1 SFR/HCN versus molecular gas surface mass density

Based on simple turbulent models of star formation (e.g. KM theory; Section 2.2), we expect a negative correlation between SFR/HCN and $\langle \Sigma_{\rm mol} \rangle$. The main driver of the negative correlation is that with increasing mean density of the cloud, HCN traces more of the bulk molecular gas thus decreasing SFR/HCN (Section 2.5). The lower left-hand panel of Fig. 6 shows the relationship between SFR/HCN and $\langle \Sigma_{\rm mol} \rangle$. The underlying model predictions (red area) is in good agreement with the data if shifted by 0.6 dex in SFR/HCN. In accordance with the model expectations, we find a negative correlation between SFR/HCN and $\langle \Sigma_{\rm mol} \rangle$ with Pearson correlation coefficient $\rho = -0.63$ and p-value smaller than 10^{-3}. The regression slope is $m_{\rm S,\,\Sigma} = -0.33 \pm 0.04$ indicating a sublinear anticorrelation, where the scatter is 0.23 dex. Note, however, that the scatter is larger at higher $\langle \Sigma_{\rm mol} \rangle$ and can be up to ∼0.5 dex at $\langle \Sigma_{\rm mol} \rangle \sim 10^3$ M$_\odot$ pc^{-2}. In comparison with the HCN/CO correlations (Section 5.2.1) the SFR/HCN correlation with $\langle \Sigma_{\rm mol} \rangle$ is weaker, but still significant. Furthermore, the scatter is roughly twice as large compared to the HCN/CO relation as also indicated by the model. The stronger scatter can be explained by the non-monotonic relation between SFR/HCN and n_0. We find consistent results among different resolutions (for fixed galaxy sample) with the same trend of steeper correlation at smaller scales (see Appendix F2 for more details).

5.3.2 SFR/HCN versus velocity dispersion

As described in Section 2.5, turbulent cloud models can predict a negative correlation between SFR/HCN and the turbulence of the molecular gas due to the widening of the density PDF resulting in a lower SFR/HCN ratio. We find a negative correlation between SFR/HCN and $\langle \sigma_{\rm mol} \rangle$ with Pearson correlation coefficient $\rho = -0.60$ and p-value smaller than 10^{-3}. We report a regression slope of $m_{\rm S,\,\sigma} = -0.63 \pm 0.07$ with moderate scatter 0.23 dex. Similar to the $\langle \Sigma_{\rm mol} \rangle$ relation, the scatter is larger at higher $\langle \sigma_{\rm mol} \rangle$.

The correlation coefficients are very similar to the ones found for SFR/HCN versus $\langle \Sigma_{\rm mol} \rangle$, as expected due to the strong correlation between $\Sigma_{\rm mol}$ and $\sigma_{\rm mol}$. The measured correlations vary with resolution and sample, where the steepness of the correlation tends to increase with the resolution, i.e. with decreasing physical scale (see Appendix F2).

Table 3. HCN/CO and SFR/HCN correlations.

Cloud-scale Property	Environment	HCN/CO				SFR/HCN			
		Slope (unc.)	Interc. (unc.)[a]	Corr. ρ (p)	Scatter	Slope (unc.)	Interc. (unc.)[a]	Corr. ρ (p)	Scatter
(1)	(2)	(3)	(4)	(5)	(6)	(7)	(8)	(9)	(10)
$\langle\Sigma_{\rm mol}\rangle$	Centres + discs	0.35 (0.02)	−1.49 (0.01)	0.88 (0.0)	0.11	−0.33 (0.04)	−0.84 (0.02)	−0.63 (0.0)	0.23
	Centres	0.33 (0.05)	−1.42 (0.03)	0.82 (0.0)	0.11	−0.20 (0.14)	−0.90 (0.08)	−0.31 (0.136)	0.30
	Discs	0.32 (0.02)	−1.50 (0.01)	0.86 (0.0)	0.14	−0.35 (0.04)	−0.85 (0.02)	−0.66 (0.0)	0.21
$\langle\sigma_{\rm mol}\rangle$	Centres + discs	0.66 (0.04)	−1.5 (0.01)	0.85 (0.0)	0.12	−0.63 (0.07)	−0.83 (0.02)	−0.60 (0.0)	0.23
	Centres	0.51 (0.13)	−1.43 (0.04)	0.69 (0.0)	0.14	−0.31 (0.27)	−0.89 (0.09)	−0.26 (0.203)	0.31
	Discs	0.64 (0.05)	−1.50 (0.01)	0.83 (0.0)	0.14	−0.74 (0.08)	−0.86 (0.02)	−0.65 (0.0)	0.20
$\langle\alpha_{\rm vir}\rangle$	Centres + discs	...	...	0.21 (0.028)	...	...	...	−0.11 (0.226)	...
	Centres	...	...	−0.12 (0.572)	...	...	...	0.19 (0.363)	...
	Discs	...	...	0.25 (0.011)	...	...	...	−0.23 (0.019)	...
$\langle P_{\rm turb}\rangle$	Centres + discs	0.17 (0.01)	−1.49 (0.01)	0.88 (0.0)	0.11	−0.15 (0.02)	−0.83 (0.02)	−0.62 (0.0)	0.22
	Centres	0.15 (0.03)	−1.41 (0.03)	0.75 (0.0)	0.12	−0.09 (0.07)	−0.90 (0.08)	−0.29 (0.160)	0.31
	Discs	0.16 (0.01)	−1.50 (0.01)	0.89 (0.0)	0.14	−0.17 (0.02)	−0.84 (0.02)	−0.67 (0.0)	0.20

Note. Fit parameters resulting from the linear regression of HCN/CO (tracing $f_{\rm dense}$) and SFR/HCN (tracing $\rm SFE_{dense}$) both at 2.1 kpc scale versus molecular cloud properties ($\Sigma_{\rm mol}$, $\sigma_{\rm mol}$, $\alpha_{\rm vir}$, and $P_{\rm turb}$) at 150 pc scale. Column (2) indicates the environment considered for the fit, where centre + disc means the whole galaxy as in Fig. 6. Centre and disc are defined as introduced in Section 6.1 and are shown in Fig. 7. Columns (3) and (4) list the slope and intercept with corresponding uncertainty estimates as determined by the linear regression tool. Column (5) shows the Pearson correlation coefficient ρ and its corresponding p-value. Column (6) displays the y-axis scatter of the data about the best-fitting line measured in units of dex. Because of the lack of correlation between HCN/CO, SFR/HCN and the virial parameter, we do not show linear regression results for $\langle\alpha_{\rm vir}\rangle$, but only list the correlation coefficients and p-values based on the significant data points. Note that for the other cloud-scale properties, the correlations coefficient (and the p-value) are determined using both the censored and the significant data.

[a]Note that the intercept is measured at ca. the median of the respective cloud-scale property as described in Section 4.6.

5.3.3 SFR/HCN versus virial parameter

Naively, one could expect that a cloud with lower virial parameter and thus higher gravitational boundedness could form stars more efficiently, suggesting an anticorrelation between SFR/HCN and $\alpha_{\rm vir}$. Moreover, assuming $\alpha_{\rm vir}$ to have only little effect on the PDF, based on equation (4), increasing $\alpha_{\rm vir}$ would shift the star formation density threshold ($n_{\rm SF}$) to higher densities hence decreasing SFR. In this consideration, we would expect an anticorrelation between SFR/HCN and $\alpha_{\rm vir}$. In the model description adopted here (Section 2), it is less obvious to explore the effect of $\alpha_{\rm vir}$ on the lognormal PDF, the SFR, and hence SFR/HCN. Yet, by assuming that $\alpha_{\rm vir}$ traces $\sigma^2_{\rm mol}/\Sigma_{\rm mol}$, we explore variations of HCN/CO as a function of empirically based $\sigma^2_{\rm mol}/\Sigma_{\rm mol}$ values (red area in Fig. 6) and predicted a small positive correlation ($\rho = -0.68$) with significant scatter.

In our data we find no correlation ($\rho = -0.11, p = 0.226$) between SFR/HCN and $\langle\sigma^2_{\rm mol}/\Sigma_{\rm mol}\rangle$ tracing $\langle\alpha_{\rm vir}\rangle$, suggesting that SFR/HCN and $\langle\alpha_{\rm vir}\rangle$ are uncorrelated. However, for the subsample that includes the five closes galaxies, we find $\rho = -0.53$ and $p = 0.003$ indicating a moderate negative correlation accordance with the model predictions at least for some galaxies (Appendix F2).

5.3.4 SFR/HCN versus internal turbulent pressure

Following the same reasoning as in Section 5.2, the effect of the turbulent pressure ($P_{\rm turb}$) on SFR/HCN can be inferred from the expected correlations of SFR/HCN with $\Sigma_{\rm mol}$ and $\sigma_{\rm mol}$, using $P_{\rm turb} \propto \Sigma_{\rm mol}\sigma^2_{\rm mol}$. Hence, we expect a negative correlation between SFR/HCN and $\langle P_{\rm turb}\rangle$ due to the negative correlation of SFR/HCN with both $\langle\Sigma_{\rm mol}\rangle$ and $\langle\sigma_{\rm mol}\rangle$. We report a negative correlation finding a Pearson correlation coefficient of $\rho = -0.62$ with p-value $< 10^{-3}$. Because of the huge dynamic range of $\langle P_{\rm turb}\rangle$ the regression slope is shallow ($m_{\rm S,\,P} = -0.15 \pm 0.02$). The scatter about the fit line is 0.22 dex very similar to the scatter seen in the $\langle\Sigma_{\rm mol}\rangle$ and $\langle\sigma_{\rm mol}\rangle$ relations. Similar to the SFR/HCN versus $\langle\Sigma_{\rm mol}\rangle$ and SFR/HCN versus $\langle\sigma_{\rm mol}\rangle$ correlations, we find a steeper correlation with increasing resolution, but consistent results among the same sample of galaxies (Appendix F2).

5.4 HCO^+ and CS

Analogously to HCN(1–0) (Sections 5.2 and 5.3), we perform the same analysis using HCO^+(1–0) and CS(2–1) as a tracer of the denser molecular medium. These molecular lines have expected excitation densities comparable to HCN(1–0). Therefore, we expect to find similar (anti) correlations. Accordingly, we study how HCO^+/CO, CS/CO and SFR/HCO^+, SFR/CS vary with the cloud-scale molecular gas properties. The detailed results are shown in the Appendices G and H.

We find that both HCO^+/CO and CS/CO positively correlate with $\langle\Sigma_{\rm mol}\rangle$, $\langle\sigma_{\rm mol}\rangle$, and $\langle P_{\rm turb}\rangle$ with Pearson correlation coefficients ∼0.8 and negligible p-values $< 10^{-5}$. In general, we find very similar slopes for the HCO^+/CO and CS/CO relations as for the HCN/CO relations showing that HCN, HCO^+, and CS are likewise sensitive to variations of the cloud-scale molecular gas properties. The scatter in the HCO^+/CO data is slightly larger that can be explained by the slightly larger HCO^+ measurement uncertainties. The CS/CO relations are shifted to lower values due to the lower CS brightness compared to HCN or HCO^+. We also observe larger scatter due to the larger CS measurement uncertainties. These results show that not only HCN/CO but also HCO^+/CO and CS/CO at kpc-scale are good proxies of the average density structure of the molecular gas.

As for SFR/HCN, we find that both SFR/HCO^+ and SFR/CS anticorrelate with $\langle\Sigma_{\rm mol}\rangle$, $\langle\sigma_{\rm mol}\rangle$, and $\langle P_{\rm turb}\rangle$ with $\rho \sim 0.5$ ($p < 10^{-3}$). This suggests that HCN, HCO^+, and CS are a similarly tracing the star-forming gas and that the ratios with SFR are likewise affected by variations of the cloud-scale molecular gas properties.

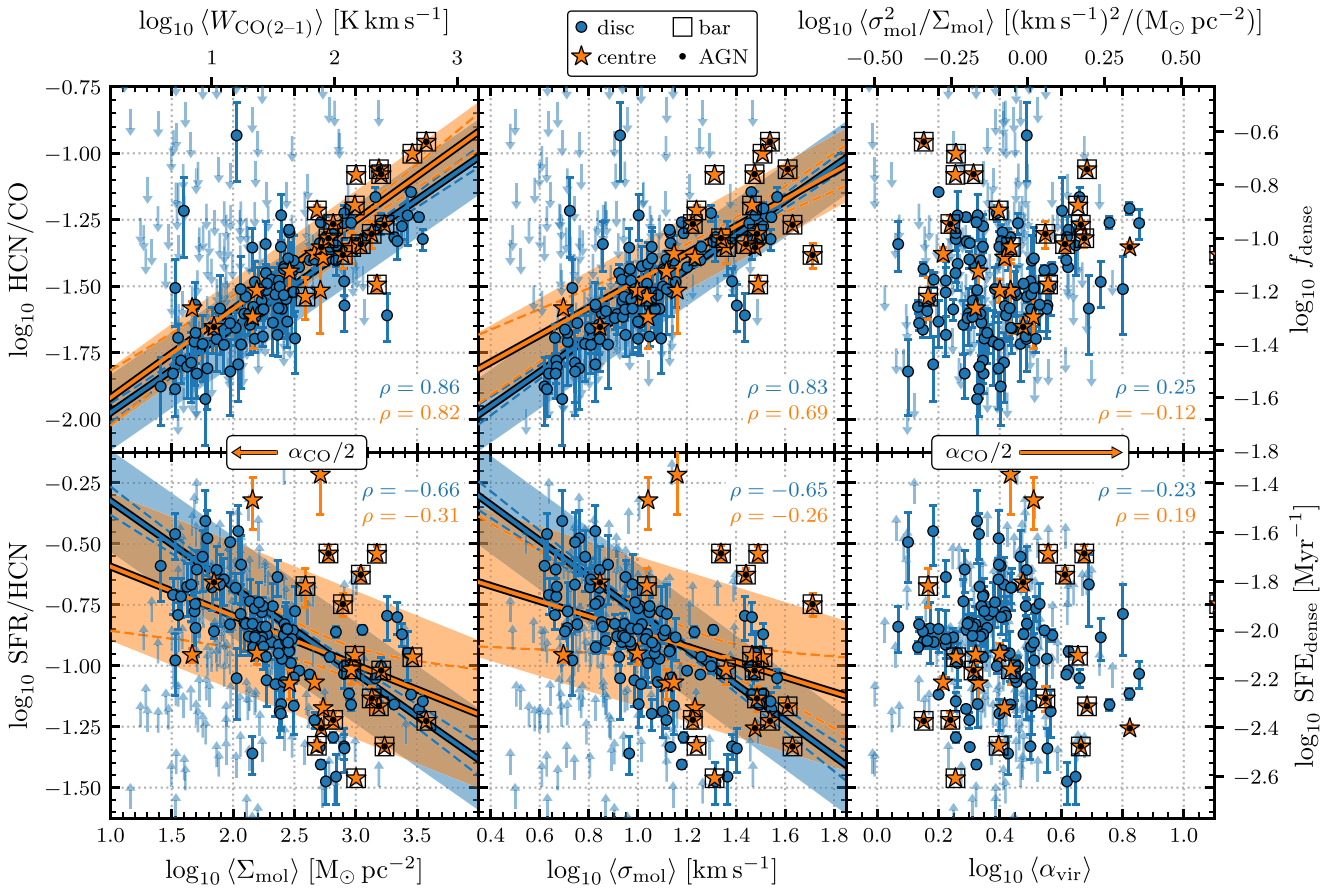

Figure 7. HCN/CO versus $\langle X \rangle$ and SFR/HCN versus $\langle X \rangle$ (cloud-scale = 150 pc, kpc-scale = 2.1 kpc) HCN/CO (top) and SFR/HCN (bottom) against molecular cloud properties – $\langle \Sigma_{\rm mol} \rangle$, $\langle \sigma_{\rm mol} \rangle$, and $\langle \alpha_{\rm vir} \rangle$ – from left to right, separately fitted for galaxy discs (blue circles) and central regions (orange stars). The shaded areas indicate the scatter and the dotted lines the 1σ credibility areas of the linear regression realizations (see Table 3 for details on the fit results). The central regions are taken as the single pixel at the galaxy centre, i.e. the inner 2.1 kpc. The remaining data points are referred to as 'disc' and processed as in Section 4.5. For the central regions we indicate if the galaxies are barred (black squares) and/or contain an AGN (black circle). The length of the orange arrow labelled with $\alpha_{\rm CO}/2$ indicates the shift of the data points in the $\Sigma_{\rm mol}$ and $\alpha_{\rm vir}$ plots if $\alpha_{\rm CO}$ would decrease by a factor of 2.

6 CORRELATION WITH LOCAL ENVIRONMENT

In the following, we study how the observed correlations may depend on the environment of the galaxies, where we separate the central kpc-scale regions from the discs (Section 6.1). We perform the analysis focusing on the same resolution configuration, i.e. 150 pc cloud-scale and 2.1 kpc kpc-scale, as in Section 5.

6.1 Central regions versus discs

The central regions of galaxies (M51, Querejeta et al. 2019; NGC 253, Jiang et al. 2020; NGC 6946, Eibensteiner et al. 2022) and the galactic CMZ (Longmore et al. 2013; Kruijssen et al. 2014; Barnes et al. 2017) are typically much denser and less efficient at forming stars from the dense gas, making them a particularly interesting environment to study as they form an interesting contrast to the discs. Therefore, we study the same relations as in Section 5 separately for the central regions and the discs. We define the central region (also referred to as 'centre' throughout this section) as the single kpc-scale (i.e. 2.1 kpc) pixel at the centre of each galaxy. Note that the physical size of the galaxy centres is typically a factor of ∼3 smaller (median size of the centre, i.e. small bulge or nucleus of the PHANGS galaxies is ∼600 pc; Querejeta et al. 2021) compared to the 1–2 kpc size adopted here. Therefore, we may underestimate the difference between the centres and the discs in our analysis. Given that we are sampling the maps with one sample per beam, the centre is one single pixel and consequently we do not bin the centres data. For the remaining pixels (i.e. all pixels except the centre) we perform the binning procedure as described in Section 4.5, but use 18 instead of 20 bins that results in similar bin sizes for the discs data compared to the binning of the full data. Finally, we separately fit linear functions to the data for the discs and the centres, analogous to the procedure used in Section 5 (see Fig. 7).

In agreement with other studies, we find that, on average, centres appear to have higher HCN/CO by about 0.17 dex (KS p-value:[11] $p_{\rm KS} = 0.001$) and lower SFR/HCN by about 0.14 dex ($p_{\rm KS} = 0.011$) across our sample of 25 nearby galaxies (see Fig. 8). None the less, centres also have higher $\Sigma_{\rm mol}$ and $\sigma_{\rm mol}$, and, hence, are found to follow similar HCN/CO and SFR/HCN relations as are observed in the discs, i.e. in agreement with the model expectations and the correlations found in Section 5. This suggests that the

[11]The two-sample Kolmogorov–Smirnov (KS) test quantifies the significance of the difference between the distributions of two samples (Hodges 1958). Here, we test the probability $p_{\rm KS}$ again the null hypothesis that e.g. centres have lower HCN/CO than discs.

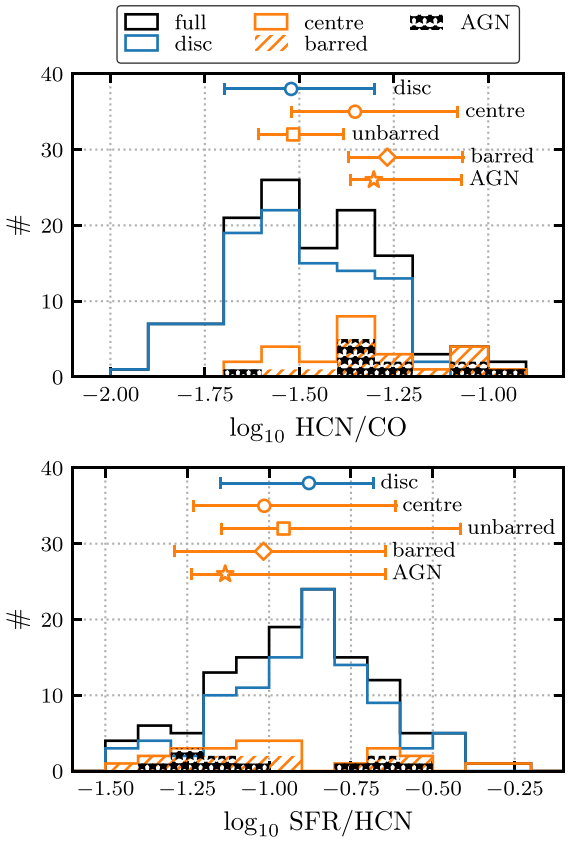

Figure 8. Histograms of HCN/CO (top) and SFR/HCN (bottom) at 2.1 kpc scale in different environments. The full data are shown in black. Centres and discs are coloured in orange and blue in analogy with Fig. 7. In addition, for the centres, we denote galaxies with a bar (diagonal hatching) or an AGN (starred hatching). The markers and lines above the histogram indicate the median and 16–84 percentiles of the respective data.

physical connection between molecular cloud properties, density distribution, and star formation is, to first order and on kpc scales, valid independent of the local environment.

In detail, the HCN/CO against $\langle\Sigma_{\rm mol}\rangle$ or $\langle\sigma_{\rm mol}\rangle$ relations show very similar linear regression slopes for the centres compared to the discs (Fig. 7). It is worth noting that we do see a minor offset between HCN/CO versus $\langle\Sigma_{\rm mol}\rangle$ for centres and discs of about ∼0.1 dex (measured as the difference in the intercepts of the fit lines at $\Sigma_{\rm mol} = 10^{2.5}$ $M_\odot$ pc^{-2}). On the one hand, this may suggest that there are other physical parameters at play that systematically affect $f_{\rm dense}$ and hence HCN/CO at fixed $\langle\Sigma_{\rm mol}\rangle$ and $\langle\sigma_{\rm mol}\rangle$. These parameters could be connected to the galaxy's environment such as the dynamical equilibrium pressure or shear (see e.g. Federrath et al. 2016; Kruijssen et al. 2019). On the other hand, offsets in $f_{\rm dense}$ or $\Sigma_{\rm mol}$ may be connected to systematic variations of the $\alpha_{\rm CO}$ and $\alpha_{\rm HCN}$ conversion factors (see Section 6.3). Overall, although the centres are slightly (to within 1σ–2σ) offset to higher HCN/CO values, they follow the same trends with the cloud-scale molecular gas properties. Thus, also in the centres, HCN/CO appears to be a good first-order tracer of mean molecular gas density.

For the SFR/HCN correlations we do not find a significant offset between the centres and the discs as is observed for the HCN/CO correlations. However, we find a flatter slope and significantly larger scatter for the centres (∼0.3 dex) compared to the discs (∼0.2 dex), especially at high $\langle\Sigma_{\rm mol}\rangle$ or $\langle\sigma_{\rm mol}\rangle$. This increasing scatter is also seen in the model predictions (Fig. 2) and is caused by the decrease of the free-fall time at large cloud densities that results in an increase of SFR/HCN at large $\Sigma_{\rm mol}$. Therefore, the KM theory can predict both a lower and a higher SFR/HCN in the centres of galaxies depending on the turbulence of the molecular clouds. Certainly, there are alternative explanations for large variations of SFR and $\rm SFE_{dense}$ in galaxy centres. One idea is that star formation in galaxy centres is episodic due to stellar feedback cycles (e.g. Krumholz & Kruijssen 2015). In addition, the accretion of dense gas to the galaxy centre may vary, leading to SFR fluctuations (Seo et al. 2019; Sormani et al. 2020; Moon et al. 2022).

6.2 Impact of bars and AGN

In addition to separating the centre from the disc, we want to study the impact of a bar or an AGN on the kpc-scale dense gas quantities in the centres of galaxies (the classifications are listed in Table 1). Sun et al. (2020b) analysed the molecular gas properties at 150 pc scale in a larger sample of 70 PHANGS galaxies and found that gas in centres of barred galaxies have higher surface density $\Sigma_{\rm mol}$ and velocity dispersion $\sigma_{\rm mol}$ compared to gas in centres of unbarred galaxies (as noted above, the defined sizes of the centres in Sun et al. 2020b are typically smaller than the central regions studied here). In this work, we also find that centres of barred galaxies tend to show higher HCN/CO by about 0.25 dex ($p_{\rm KS} = 0.0002$) (see Figs 7 and 8). SFR/HCN is only insignificantly lower ($p_{\rm KS} = 0.436$) in barred galaxies by about 0.06 dex. Moreover, we find that molecular gas in centres of unbarred galaxies is similar in terms of HCN/CO and SFR/HCN to the values found in discs (a result reported for the molecular cloud properties by Sun et al. 2018).

Moreover, we examine how an AGN may affect the (dense) molecular gas in the central region of galaxies. Our sample contains 11 AGN galaxies (14 without AGN). Note that there is a significant overlap between AGN and barred galaxies, so we cannot easily discriminate the impact of bars and AGN. On average, the AGN seems to boost HCN/CO in the centres of galaxies. We find 0.12 dex higher median HCN/CO ($p_{\rm KS} = 0.040$) in the centres of AGN galaxies compared to the centres that do not harbour an AGN. These results suggest that centres of AGN galaxies have higher molecular gas surface densities and turbulence, which, following the correlations found in this work, lead to higher HCN/CO. It is less clear how AGNs affect SFR/HCN, which is only insignificantly ($p_{\rm KS} = 0.208$) lower by 0.17 dex. Also, in some AGN galaxies, we observe higher SFR/HCN in the central regions. This could be explained by the increase of SFR/HCN at very high $\Sigma_{\rm mol}$ as seen in models, or point at more complex gas dynamics in centres.

6.3 Conversion factors

In Section 4.3.1, we discussed how the CO-to-H_2 conversion factor $\alpha_{\rm CO}$ can vary with local environment. Most notable, $\alpha_{\rm CO}$ has been observed to be lower in the centres of galaxies compared to the disc that is linked to the high surface density, turbulence, and temperature yielding a brighter CO emission (see e.g. Shetty et al. 2011a,b; Watanabe et al. 2011; Papadopoulos et al. 2012; Bolatto et al. 2013; Sandstrom et al. 2013; Israel 2020; Teng et al. 2022). We note that $\alpha_{\rm CO}$ can be 3–10 times lower in galaxy centres compared to the default MW value that is also adopted here (Israel 2020). Sandstrom et al. (2013) report a factor of ∼2 lower $\alpha_{\rm CO}$ in the central kpc regions compared to the average disc value in their sample of 26 nearby star-forming galaxies. Therefore, we indicate how lowering $\alpha_{\rm CO}$ by a factor of 2 in the central regions of galaxies affects the data points in

the correlations studied here. In the first instance, we only consider changes in the cloud-scale properties and leave the y-axis coordinate unchanged. As denoted by the orange arrows in Fig. 7, reducing $\alpha_{\rm CO}$ by 0.3 dex decreases $\Sigma_{\rm mol}$ and increases $\alpha_{\rm vir}$ by 0.3 dex. This has only little effect on the correlations with $\langle\Sigma_{\rm mol}\rangle$, but would increase the offset in the correlations between the centres and the discs. Though, it would slightly increase the strength of the correlations with $\langle\alpha_{\rm vir}\rangle$ due to making the clouds in the centres much less bound, such that we would find $\rho = 0.33$ for HCN/CO versus $\langle\alpha_{\rm vir}\rangle$ and $\rho = -0.12$ for SFR/HCN versus $\langle\alpha_{\rm vir}\rangle$. However, if we would account for the power-law extension of the lognormal PDF, bound clouds would always have higher dense gas fraction thus counteracting the shift to higher virial parameter values for the centres. In the end, variations with $\alpha_{\rm vir}$ remain complex and we cannot infer a clear conclusion whether HCN/CO or SFR/HCN varies significantly with $\alpha_{\rm vir}$.

We investigate how decreasing $\alpha_{\rm CO}$ for the centres may affect the y-axis coordinates if HCN/CO and SFR/HCN are converted to $f_{\rm dense}$ and SFE$_{\rm dense}$, respectively. In contrast to $\alpha_{\rm CO}$, there is very little information on environmental variations of $\alpha_{\rm HCN}$ in the literature. We could assume that $\alpha_{\rm HCN}$ varies similarly as $\alpha_{\rm CO}$, which might be justified because $\alpha_{\rm HCN}$ becomes optically thick towards centres (see e.g. Jiménez-Donaire et al. 2019) yielding stronger HCN emission. Then, $f_{\rm dense}$ would be unaffected, while SFE$_{\rm dense}$ would increase in the centres of galaxies thus decreasing the correlation with the cloud-scale molecular as properties. We could also assume that $\alpha_{\rm CO}$ varies much more than $\alpha_{\rm HCN}$ and thus neglect $\alpha_{\rm HCN}$ variations. In this case, SFE$_{\rm dense}$ would be unaffected, while $f_{\rm dense}$ would increase in the centres of galaxies that increases the observed correlation, but also significantly enhances the offset between centres and galaxies. The centre–disc offset could only be dissolved if $\alpha_{\rm HCN}$ is lowered even more than $\alpha_{\rm CO}$ in the centres thus yielding a lower $f_{\rm dense}$.

Overall, variations of $\alpha_{\rm CO}$ and $\alpha_{\rm HCN}$ will eventually change the slope and strength of the correlations, but only at the 0.3 dex level, which is not sufficient to change the direction of the relations. Primarily, the correlations are driven by the discs, which are much less affected by variations of the conversion factors than the centres. We thus, highlight that our findings show significant systematic variations of HCN/CO and SFR/HCN with cloud-scale gas properties. Independent of whether HCN/CO and SFR/HCN can be accurately translated to $f_{\rm dense}$ and SFE$_{\rm dense}$, respectively, they are very useful tools to trace the mean density structure of molecular gas.

7 SUMMARY AND DISCUSSION

In this work, we investigate the connection of the density-sensitive kpc-scale (2.1 kpc) HCN/CO and SFR/HCN ratios with various structural and dynamical properties ($\Sigma_{\rm mol}$, $\sigma_{\rm mol}$, $\alpha_{\rm vir}$, and $P_{\rm turb}$) of the cloud-scale (150 pc) molecular gas across 25 nearby galaxies. In the literature, HCN/CO and SFR/HCN are often synonymous with the dense gas fraction and dense gas star formation efficiency, respectively. This is based on the assumption that CO and HCN emission is originating from molecular gas differing within different (often fixed) density regimes. However, observations (e.g. Kauffmann et al. 2017; Pety et al. 2017; Barnes et al. 2020; Evans et al. 2020) and simulations (e.g. Mangum & Shirley 2015; Shirley 2015; Leroy et al. 2017a; Onus et al. 2018; Jones et al. 2022) highlight that there is still a significant uncertainty in the exact density thresholds and their mass conversion factors. In this study, we focus on the quantities HCN/CO and SFR/HCN and are careful to draw conclusions from the less certain physical quantities, i.e. $f_{\rm dense}$ and SFE$_{\rm dense}$.

In Section 2, we lay out qualitative predictions about the direction of the studied correlations based on single free-fall time turbulent cloud models (e.g. the KM theory; Krumholz & McKee 2005). We find that molecular cloud properties affect the density distribution of the molecular gas such that, within this simplified model description, HCN/CO is expected to correlate and SFR/HCN to anticorrelate with molecular cloud properties like the mean density, traced by the surface density, or the Mach number, traced by the velocity dispersion of the molecular gas. The underlying physical mechanisms are that the mean density shifts the density PDF, while the Mach number affects the width of the PDF that in return affects the line emissivity of molecular lines like CO(2–1) and HCN(1–0) and the SFR.

We compare the cloud scale properties to the kpc-scale HCN/CO and SFR/HCN via intensity-weighted averaging (Section 4.4). To quantitatively analyse the correlations, we fit a linear regression model to the data in log–log scale in order to determine a first-order power-law dependence. We measure the strength of the correlation by computing the Pearson correlation coefficient and the corresponding p-value (Section 5). Moreover, we study the correlation with local environment by separately analysing the central kpc-scale regions to contrast with the discs (Section 6). In the following we summarize and interpret our main findings.

(i) We report systematic variations of HCN/CO with cloud-scale molecular gas properties (Fig. 6 and Section 5.2). Building up on the works of Gallagher et al. (2018a,b), we find a strong positive correlation ($\rho \approx 0.9$) between HCN/CO and the cloud-scale surface density $\Sigma_{\rm mol}$ as traced by the CO(2–1) line intensity adopting a fixed line-to-mass conversion factor $\alpha_{\rm CO} = 4.3\,{\rm M}_\odot\,{\rm pc}^{-2}\,({\rm K\,km\,s}^{-1})^{-1}$ (Bolatto et al. 2013) and a fixed CO(2–1)-to-CO(1–0) line ratio $R_{21} = 0.64$ (den Brok et al. 2021). The results are in agreement with the model predictions, where the mean density (assumed to be traced by $\Sigma_{\rm mol}$) affects the median of the density PDF without altering its shape such that higher n_0 leads to higher HCN/CO. This is a powerful indication that both HCN/CO and cloud-scale CO trace density. Moreover, we observe a strong positive correlation ($\rho \approx 0.9$) between HCN/CO and the cloud-scale velocity dispersion as traced by the CO(2–1) line width in agreement with our simplified model, in which the Mach number (traced by $\sigma_{\rm mol}$) affects the width of the density PDF such that higher $\mathcal{M}$ leads to higher HCN/CO. These correlations also imply that HCN/CO positively correlates with the cloud-scale internal turbulent pressure as traced via $P_{\rm turb} \propto \Sigma_{\rm mol}\sigma^2_{\rm mol}$. Furthermore, we find a weak ($\rho \approx 0.2$, p-value < 0.03) positive correlation between HCN/CO and the virial parameter as measured via $\alpha_{\rm vir} \propto \sigma^2_{\rm mol}/\Sigma_{\rm mol}$ that is supported by models if n_0 and $\mathcal{M}$ are traced by the cloud-scale CO intensity and line width, respectively.

(ii) We report that SFR/HCN systematically varies with cloud-scale molecular gas properties (Fig. 6 and Section 5.3) finding a negative correlation ($\rho \approx 0.6$) between SFR/HCN and the cloud-scale $\Sigma_{\rm mol}$ and $\sigma_{\rm mol}$. These results are in agreement with turbulent cloud models, in which stars are assumed to form from the dense gas above some threshold density $n_{\rm SF} \propto n_0\alpha_{\rm vir}\mathcal{M}^2$. Our findings show that, although SFR linearly correlates with HCN over several orders of magnitude, SFR/HCN varies systematically as a function of the cloud-scale molecular gas properties, thus disclaiming the constant SFE$_{\rm dense}$ hypothesis put forward by Gao & Solomon (2004). Extending the works of Longmore et al. (2013), Kruijssen et al. (2014), Bigiel et al. (2016), Barnes et al. (2017), Gallagher et al. (2018a,b), Jiménez-Donaire et al. (2019), Querejeta et al. (2019), Jiang et al. (2020), and Eibensteiner et al. (2022) who showed that the amount of dense gas is not enough to set the SFR, we conclude that SFR/HCN is significantly affected by the density distribution of molecular clouds that, based on turbulent cloud models, affects both the emissivity of dense gas tracers like HCN and the SFR and hence

SFR/HCN. Moreover, we find no universal evidence for a correlation between SFR/HCN and $\sigma^2_{\rm mol}/\Sigma_{\rm mol}$ tracing $\alpha_{\rm vir}$ ($\rho \approx -0.1$, p-value ~ 0.2). For some galaxies (e.g. NGC 2903) we find indications of a negative correlation between SFR/HCN and $\alpha_{\rm vir}$ ($\rho \approx -0.5$, p-value < 0.01) This trend is supported by the model predictions (Fig. 2) and would point towards less bound clouds being less efficient in forming stars from a fixed fraction of dense gas.

(iii) Using HCO^+ or CS as a tracer of the dense molecular gas, we find the same correlations with the cloud-scale molecular gas properties as seen with HCN. This is a powerful indicator that not only HCN, but also other tracers with critical densities in excess of that of low-J CO lines like HCO^+ or CS, observed at kpc-scale, are sensitive to the density structure of the cloud-scale molecular gas.

(iv) Separating the central ∼kpc regions from the rest of the galaxy discs. We find that centres have significantly higher HCN/CO and lower SFR/HCN compared to discs (Fig. 8 and Section 6.1). None the less, both environments follow similar HCN/CO and SFR/HCN trends against the cloud-scale properties (Fig. 7). This suggests that the physical connection between molecular cloud properties, density distribution, and star formation is independent of the local environment and extends from low density, less turbulent clouds as predominantly found in the disc to high density and turbulent clouds as found in the centres of galaxies. We also studied the impact of bars and AGN on the central regions of galaxies, finding typically higher HCN/CO and lower SFR/HCN for barred and AGN galaxies compared to their complements (unbarred and without AGN), respectively. This suggests that bars and AGNs boost HCN/CO and lower SFR/HCN in the centres of galaxies. Differences are though small ∼0.1–0.2 dex and only significant for HCN/CO. Throughout this work we assumed a constant $\alpha_{\rm CO}$ conversion factor. We study whether these scaling relations change when we assume that centres have systematically lower $\alpha_{\rm CO}$ than discs that has been reported in the literature (Sandstrom et al. 2013). Adopting $\alpha_{\rm CO}/2$ for the central regions, we find no significant effect on either the HCN/CO or the SFR/HCN relations with the cloud-scale properties.

Our findings demonstrate that density, cloud-scale molecular gas properties, and star formation appear interrelated in a coherent way and one that agrees reasonably well with current models. Our results also strongly reinforce the view that HCN/CO and similar line ratios (e.g. HCO^+/CO or CS/CO) are sensitive measures of the density distribution of the molecular gas and thus powerful tools in extragalatic studies. Regardless of physical interpretation, we observe clear correlations between molecular cloud properties and line ratios sampling different physical densities. These should represent significant observational constraints on any theory attempting to relate star formation, gas density, and the ISM in galaxies. Many previous studies (e.g. Chin et al. 1997, 1998; Gao & Solomon 2004; Brouillet et al. 2005; Lada, Lombardi & Alves 2010; Wu et al. 2010; Rosolowsky, Pineda & Gao 2011; García-Burillo et al. 2012; Buchbender et al. 2013; Longmore et al. 2013; Kepley et al. 2014; Chen et al. 2015, 2017; Usero et al. 2015; Bigiel et al. 2016; Shimajiri et al. 2017; Gallagher et al. 2018a; Jiménez-Donaire et al. 2019; Bešlić et al. 2021) show that HCN luminosity (tracing dense gas mass) and SFR are strongly correlated probing scales ranging from nearby galactic cloud to entire galaxy spanning ∼8 orders of magnitude. Therefore, Shimajiri et al. (2017) propose a quasi-universal $\rm SFE_{dense}$. Our results support this picture. However, all previous works and our results show a ∼1 dex scatter in $\rm SFE_{dense}$. Here, we show that this scatter is not random, but that SFR/HCN correlates with the properties of the molecular gas, i.e. $\Sigma_{\rm mol}$ and $\sigma_{\rm mol}$, at 150 pc scale. It is still much of an open question what drives $\rm SFE_{dense}$ in galaxy centres, where we observe typically lower $\rm SFE_{dense}$ but also large scatter. Ultimately, we need high-resolution (cloud-scale), high-sensitivity spectroscopic mapping of a large sample of galaxies in order to resolve and study the effect of local environment on the dense molecular gas and star formation. This work also motivates to further investigate how spiral arms, bars and AGN may affect the density distribution of molecular gas in galaxy centres.

ACKNOWLEDGEMENTS

We would like to thank the referee for their constructive feedback that helped improve the paper. This work was carried out as part of the PHANGS Collaboration. ATB, JP, JSdB and FB would like to acknowledge funding from the European Research Council (ERC) under the European Union's Horizon 2020 Framework Programme (grant agreement no. 726384/Empire). The work of AKL and MJG on the early parts of this work was partially supported by the National Science Foundation under grants no. 1615105, 1615109, and 1653300. MC gratefully acknowledges funding from the Deutsche Forschungsgemeinschaft (DFG) through an Emmy Noether Research Group (grant number CH2137/1-1). COOL Research DAO is a Decentralized Autonomous Organization supporting research in astrophysics aimed at uncovering our cosmic origins. MC and JMDK gratefully acknowledge funding from the Deutsche Forschungsgemeinschaft (DFG) through an Emmy Noether Research Group (grant no. KR4801/1-1) and the DFG Sachbeihilfe (grant no. KR4801/2-1), as well as from the European Research Council (ERC) under the European Union's Horizon 2020 Framework Programme via the ERC Starting Grant MUSTANG (grant agreement no. 714907). CE gratefully acknowledges funding from the Deutsche Forschungsgemeinschaft (DFG) Sachbeihilfe, grant no. BI1546/3-1. RSK and SCOG acknowledge support from the Deutsche Forschungsgemeinschaft (DFG) in the Collaborative Research Centre (SFB 881, ID 138713538) 'The Milky Way System' (subprojects A1, B1, B2, and B8) and from the Heidelberg Cluster of Excellence (EXC 2181, ID 390900948) 'STRUCTURES: A unifying approach to emergent phenomena in the physical world, mathematics, and complex data', funded by the German Excellence Strategy. RSK also thanks for funding form the European Research Council in the ERC Synergy Grant 'ECOGAL – Understanding our Galactic ecosystem: From the disk of the Milky Way to the formation sites of stars and planets' (ID 855130). RSK and SCOG also benefit from computing resources provided by the State of Baden-Württemberg through bwHPC and DFG through grant INST 35/1134-1 FUGG, and from the data storage facility SDS@hd supported through grant INST 35/1314-1 FUGG, and they thank resources provided by the Leibniz Computing Centre (LRZ) for project pr74nu. MQ acknowledges support from the Spanish grant PID2019-106027GA-C44, funded by MCIN/AEI/10.13039/501100011033. ER acknowledges the support of the Natural Sciences and Engineering Research Council of Canada (NSERC), funding reference number RGPIN-2022-03499. The work of JS is partially supported by the Natural Sciences and Engineering Research Council of Canada (NSERC) through the Canadian Institute for Theoretical Astrophysics (CITA) National Fellowship. Y-HT acknowledges funding support from NRAO Student Observing Support Grant SOSPADA-012 and from the National Science Foundation (NSF) under grant no. 2108081. MCS acknowledges financial support from the European Research Council via the ERC Synergy Grant 'ECOGAL – Understanding our Galactic ecosystem: from the disk of the Milky Way to the formation sites of stars and planets' (grant no. 855130). TGW and ES acknowledge funding from

the European Research Council (ERC) under the European Union's Horizon 2020 Framework Programme (grant agreement no. 694343). AU acknowledges support from the Spanish grants PGC2018-094671-B-I00, funded by MCIN/AEI/10.13039/501100011033 and by 'ERDF A way of making Europe', and PID2019-108765GB-I00, funded by MCIN/AEI/10.13039/501100011033. KG is supported by the Australian Research Council through the Discovery Early Career Researcher Award (DECRA) Fellowship DE220100766 funded by the Australian Government. KG is supported by the Australian Research Council Centre of Excellence for All Sky Astrophysics in 3 Dimensions (ASTRO 3D), through project number CE170100013. JeP acknowledges support by the French Agence Nationale de la Recherche through the DAOISM grant ANR-21-CE31-0010, and by the Programme National 'Physique et Chimie du Milieu Interstellaire' (PCMI) of INSU,CNRS with INC/INP, cofunded by CEA and CNES.

This paper makes use of the following ALMA data, which have been processed as part of the ALMOND and PHANGS–ALMA surveys:

ADS/JAO.ALMA#2012.1.00650.S, ADS/JAO.ALMA #2013.1.01161.S, ADS/JAO.ALMA#2015.1.00925.S, ADS/JAO.ALMA#2015.1.00956.S, ADS/JAO.ALMA #2017.1.00230.S, ADS/JAO.ALMA#2017.1.00392.S, ADS/JAO.ALMA#2017.1.00766.S, ADS/JAO.ALMA #2017.1.00815.S, ADS/JAO.ALMA#2017.1.00886.L, ADS/JAO.ALMA#2018.1.01171.S, ADS/JAO.ALMA #2018.1.01651.S, ADS/JAO.ALMA#2018.A.00062.S, ADS/JAO.ALMA#2019.2.00134.S, and ADS/JAO.ALMA #2021.1.00740.S. ALMA is a partnership of ESO (representing its member states), NSF (USA), and NINS (Japan), together with NRC (Canada), NSC and ASIAA (Taiwan), and KASI (Republic of Korea), in cooperation with the Republic of Chile. The Joint ALMA Observatory is operated by ESO, AUI/NRAO, and NAOJ. The National Radio Astronomy Observatory (NRAO) is a facility of the National Science Foundation operated under cooperative agreement by Associated Universities, Inc.

This work makes use of data products from the *Wide-field Infrared Survey Explorer* (*WISE*), which is a joint project of the University of California, Los Angeles, and the Jet Propulsion Laboratory/California Institute of Technology, funded by NASA.

This work is based in part on observations made with the *Galaxy Evolution Explorer* (*GALEX*). *GALEX* is a NASA Small Explorer, whose mission was developed in cooperation with the Centre National d'Etudes Spatiales (CNES) of France and the Korean Ministry of Science and Technology. *GALEX* is operated for NASA by the California Institute of Technology under NASA contract NAS5-98034.

Facilities: ALMA, *WISE*, *GALEX*

Software: NumPy (Harris et al. 2020), SciPy (Virtanen et al. 2020), astropy (Astropy Collaboration 2018), pandas (The Pandas Development Team 2021), matplotlib (Hunter 2007), colorcet (Kovesi 2015), LinMix (Kelly 2007).

DATA AVAILABILITY

The data used within this paper will be provided on reasonable request to the corresponding author.

REFERENCES

Allende Prieto C., Lambert D. L., Asplund M., 2001, ApJ, 556, L63
Anand G. S. et al., 2021, MNRAS, 501, 3621
André P., Di Francesco J., Ward-Thompson D., Inutsuka S. I., Pudritz R. E., Pineda J. E., 2014, in Beuther H., Klessen R. S., Dullemond C. P., Henning T., eds, Protostars and Planets VI. Univ. Arizona Press, Tucson, AZ, p. 27
Astropy Collaboration, 2018, AJ, 156, 123
Ballesteros-Paredes J., 2006, MNRAS, 372, 443
Barnes A. T., Longmore S. N., Battersby C., Bally J., Kruijssen J. M. D., Henshaw J. D., Walker D. L., 2017, MNRAS, 469, 2263
Barnes A. T. et al., 2020, MNRAS, 497, 1972
Bemis A., Wilson C. D., 2019, AJ, 157, 131
Bertoldi F., McKee C. F., 1992, ApJ, 395, 140
Bešlić I. et al., 2021, MNRAS, 506, 963
Bigiel F., Leroy A., Walter F., Brinks E., de Blok W. J. G., Madore B., Thornley M. D., 2008, AJ, 136, 2846
Bigiel F., Leroy A. K., Blitz L., Bolatto A. D., da Cunha E., Rosolowsky E., Sandstrom K., Usero A., 2015, ApJ, 815, 103
Bigiel F. et al., 2016, ApJ, 822, L26
Bolatto A. D., Wolfire M., Leroy A. K., 2013, ARA&A, 51, 207
Braine J., Shimajiri Y., André P., Bontemps S., Gao Y., Chen H., Kramer C., 2017, A&A, 597, A44
Brouillet N., Muller S., Herpin F., Braine J., Jacq T., 2005, A&A, 429, 153
Buchbender C. et al., 2013, A&A, 549, A17
Burkhart B., 2018, ApJ, 863, 118
CASA Team et al., 2022, PASP, 134, 114501
Chen H., Gao Y., Braine J., Gu Q., 2015, ApJ, 810, 140
Chen H., Braine J., Gao Y., Koda J., Gu Q., 2017, ApJ, 836, 101
Chin Y. N., Henkel C., Whiteoak J. B., Millar T. J., Hunt M. R., Lemme C., 1997, A&A, 317, 548
Chin Y. N., Henkel C., Millar T. J., Whiteoak J. B., Marx-Zimmer M., 1998, A&A, 330, 901
den Brok J. S. et al., 2021, MNRAS, 504, 3221
Draine B. T., 2011, Physics of the Interstellar and Intergalactic Medium. Princeton Univ. Press, Princeton, NJ
Eibensteiner C. et al., 2022, A&A, 659, A173
Evans N. J. I., Kim K.-T., Wu J., Chao Z., Heyer M., Liu T., Nguyen-Lu'o'ng Q., Kauffmann J., 2020, ApJ, 894, 103
Federrath C., Klessen R. S., 2012, ApJ, 761, 156
Federrath C., Klessen R. S., 2013, ApJ, 763, 51
Federrath C., Klessen R. S., Schmidt W., 2008, ApJ, 688, L79
Federrath C., Roman-Duval J., Klessen R. S., Schmidt W., Mac Low M. M., 2010, A&A, 512, A81
Federrath C. et al., 2016, ApJ, 832, 143
Fuente A., Schmidt M., 1959, ApJ, 129, 243
Gallagher M. J. et al., 2018a, ApJ, 858, 90
Gallagher M. J. et al., 2018b, ApJ, 868, L38
Gao Y., Solomon P. M., 2004, ApJ, 606, 271
Gao Y., Carilli C. L., Solomon P. M., Vanden Bout P. A., 2007, ApJ, 660, L93
García-Burillo S., Usero A., Alonso-Herrero A., Graciá-Carpio J., Pereira-Santaella M., Colina L., Planesas P., Arribas S., 2012, A&A, 539, A8
Girichidis P., Konstandin L., Whitworth A. P., Klessen R. S., 2014, ApJ, 781, 91
Goldsmith P., Kauffmann J., 2018, Am. Astron. Soc. Meeting Abstr., #231, 130.06
Graciá-Carpio J., García-Burillo S., Planesas P., Fuente A., Usero A., 2008, A&A, 479, 703
Harris C. R. et al., 2020, Nature, 585, 357
Hennebelle P., Chabrier G., 2011, ApJ, 743, L29
Henshaw J. D. et al., 2016, MNRAS, 457, 2675
Heyer M. H., Carpenter J. M., Snell R. L., 2001, ApJ, 551, 852
Hodges J. L., 1958, Arkiv Matematik, 3, 469
Hunter J. D., 2007, Comput. Sci. Eng., 9, 90
Israel F. P., 2020, A&A, 635, A131
Jiang X.-J. et al., 2020, MNRAS, 494, 1276
Jiménez-Donaire M. J. et al., 2017, MNRAS, 466, 49
Jiménez-Donaire M. J. et al., 2019, ApJ, 880, 127
Jones G. H., Clark P. C., Glover S. C. O., Hacar A., 2023, MNRAS, 520, 1005

Juneau S., Narayanan D. T., Moustakas J., Shirley Y. L., Bussmann R. S., Kennicutt R. C. J., Vanden Bout P. A., 2009, ApJ, 707, 1217
Kainulainen J., Beuther H., Henning T., Plume R., 2009, A&A, 508, L35
Kauffmann J., Bertoldi F., Bourke T. L., Evans N. J. I., Lee C. W., 2008, A&A, 487, 993
Kauffmann J., Goldsmith P. F., Melnick G., Tolls V., Guzman A., Menten K. M., 2017, A&A, 605, L5
Kelly B. C., 2007, ApJ, 665, 1489
Kennicutt R. C. J., 1998, ApJ, 498, 541
Kennicutt R. C., Evans N. J., 2012, ARA&A, 50, 531
Kepley A. A., Leroy A. K., Frayer D., Usero A., Marvil J., Walter F., 2014, ApJ, 780, L13
Klessen R. S., Glover S. C. O., 2016, in Revaz Y., Jablonka P., Teyssier R., Mayer L., eds, Saas-Fee Advanced Course Vol. 43, Star Formation in Galaxy Evolution: Connecting Numerical Models to Reality. Springer-Verlag, Berlin, p. 85
Kovesi P., 2015, preprint (arXiv:1509.03700)
Krips M., Neri R., García-Burillo S., Martín S., Combes F., Graciá-Carpio J., Eckart A., 2008, ApJ, 677, 262
Kruijssen J. M. D., Longmore S. N., Elmegreen B. G., Murray N., Bally J., Testi L., Kennicutt R. C., 2014, MNRAS, 440, 3370
Kruijssen J. M. D. et al., 2019, MNRAS, 484, 5734
Krumholz M. R., Kruijssen J. M. D., 2015, MNRAS, 453, 739
Krumholz M. R., McKee C. F., 2005, ApJ, 630, 250
Krumholz M. R., Thompson T. A., 2007, ApJ, 669, 289
Lada C. J., Lada E. A., 2003, ARA&A, 41, 57
Lada C. J., Lombardi M., Alves J. F., 2010, ApJ, 724, 687
Lang P. et al., 2020, ApJ, 897, 122
Leroy A. K. et al., 2009, AJ, 137, 4670
Leroy A. K. et al., 2013, AJ, 146, 19
Leroy A. K. et al., 2016, ApJ, 831, 16
Leroy A. K. et al., 2017a, ApJ, 835, 217
Leroy A. K. et al., 2017b, ApJ, 846, 71
Leroy A. K. et al., 2019, ApJS, 244, 24
Leroy A. K. et al., 2021a, ApJS, 255, 19
Leroy A. K. et al., 2021b, ApJS, 257, 43
Leroy A. K. et al., 2022, ApJ, 927, 149
Longmore S. N. et al., 2013, MNRAS, 429, 987
Mangum J. G., Shirley Y. L., 2015, PASP, 127, 266
Martin D. C. et al., 2005, ApJ, 619, L1
McKee C. F., Zweibel E. G., 1992, ApJ, 399, 551
Molina F. Z., Glover S. C. O., Federrath C., Klessen R. S., 2012, MNRAS, 423, 2680
Moon S., Kim W.-T., Kim C.-G., Ostriker E. C., 2022, ApJ, 925, 99
Murphy E. J. et al., 2011, ApJ, 737, 67
Onus A., Krumholz M. R., Federrath C., 2018, MNRAS, 479, 1702
Padoan P., Federrath C., Chabrier G., Evans N. J. I., Johnstone D., Jørgensen J. K., McKee C. F., Nordlund Å., 2014, in Beuther H., Klessen R. S., Dullemond C. P., Henning T., eds, Protostars and Planets VI. Univ. Arizona Press, Tucson, AZ, p. 77
Padoan P., Nordlund Å., 2002, ApJ, 576, 870
Padoan P., Nordlund Å., 2011, ApJ, 730, 40
Papadopoulos P. P., van der Werf P., Xilouris E., Isaak K. G., Gao Y., 2012, ApJ, 751, 10
Pety J. et al., 2017, A&A, 599, A98
Privon G. C. et al., 2015, ApJ, 814, 39
Querejeta M. et al., 2015, ApJS, 219, 5
Querejeta M. et al., 2019, A&A, 625, A19
Querejeta M. et al., 2021, A&A, 656, A133
Rosolowsky E., Leroy A., 2006, PASP, 118, 590
Rosolowsky E., Pineda J. E., Gao Y., 2011, MNRAS, 415, 1977
Rosolowsky E. et al., 2021, MNRAS, 502, 1218
Salim S. et al., 2016, ApJS, 227, 2
Salim S., Boquien M., Lee J. C., 2018, ApJ, 859, 11
Sánchez-García M., Garcia-Burillo S., Pereira-Santaella M., Colina L., Usero A., Querejeta M., Alonso-Herrero A., Fuente A., 2022, A&A, 660, A83
Sandstrom K. M. et al., 2013, ApJ, 777, 5
Schneider N. et al., 2015, A&A, 578, A29
Schruba A. et al., 2011, AJ, 142, 37
Seo W.-Y., Kim W.-T., Kwak S., Hsieh P.-Y., Han C., Hopkins P. F., 2019, ApJ, 872, 5
Shetty R., Glover S. C., Dullemond C. P., Klessen R. S., 2011a, MNRAS, 412, 1686
Shetty R., Glover S. C., Dullemond C. P., Ostriker E. C., Harris A. I., Klessen R. S., 2011b, MNRAS, 415, 3253
Shimajiri Y. et al., 2017, A&A, 604, A74
Shirley Y. L., 2015, PASP, 127, 299
Sormani M. C., Tress R. G., Glover S. C. O., Klessen R. S., Battersby C. D., Clark P. C., Hatchfield H. P., Smith R. J., 2020, MNRAS, 497, 5024
Stephens I. W., Jackson J. M., Whitaker J. S., Contreras Y., Guzmán A. E., Sanhueza P., Foster J. B., Rathborne J. M., 2016, ApJ, 824, 29
Sun J. et al., 2018, ApJ, 860, 172
Sun J. et al., 2020a, ApJ, 892, 148
Sun J. et al., 2020b, ApJ, 901, L8
Teng Y.-H. et al., 2022, ApJ, 925, 72
The Pandas Development Team, 2021, pandas-dev/pandas: Pandas 1.3.4 (v1.3.4). Zenodo
Tielens A. G. G. M., 2010, The Physics and Chemistry of the Interstellar Medium. Cambridge Univ. Press, Cambridge
Usero A. et al., 2015, AJ, 150, 115
Utomo D. et al., 2018, ApJ, 861, L18
Véron-Cetty M. P., Véron P., 2010, A&A, 518, A10
Virtanen P. et al., 2020, Nat. Methods, 17, 261
Watanabe Y., Sorai K., Kuno N., Habe A., 2011, MNRAS, 411, 1409
Wong T., Blitz L., 2002, ApJ, 569, 157
Wright E. L. et al., 2010, AJ, 140, 1868
Wu J., Evans Neal J. I., Gao Y., Solomon P. M., Shirley Y. L., Vanden Bout P. A., 2005, ApJ, 635, L173
Wu J., Evans Neal J. I., Shirley Y. L., Knez C., 2010, ApJS, 188, 313

SUPPORTING INFORMATION

Supplementary data are available at *MNRAS* online.

Paper_ALMOND_supplements.pdf

Please note: Oxford University Press is not responsible for the content or functionality of any supporting materials supplied by the authors. Any queries (other than missing material) should be directed to the corresponding author for the article.

APPENDIX A: CLOUD-SCALE MOLECULAR GAS PROPERTIES

Fig. A1 displays the velocity dispersion of the molecular gas ($\sigma_{\rm mol}$) against its surface density ($\Sigma_{\rm mol}$) for all individual sightlines across the full sample of 22 galaxies at 150 pc resolution (blue data points) similar to fig. 1 in Sun et al. (2020b). $\sigma_{\rm mol}$ and $\Sigma_{\rm mol}$ are inferred from the CO(2–1) observations as described in Sections 4.3.1 and 4.3.2, respectively. The plot also shows loci of constant virial parameter ($\alpha_{\rm vir}$) and internal turbulent pressure ($P_{\rm turb}$) as obtained from the CO(2–1) observations as described in Sections 4.3.3 and 4.3.4, respectively, such that $\alpha_{\rm vir} \propto \sigma_{\rm mol}^2/\Sigma_{\rm mol}$ and $P_{\rm turb} \propto \Sigma_{\rm mol}\sigma_{\rm mol}^2$ at fixed scale (here 150 pc). Moreover, we indicate the intensity-weighted averages (red points) of the 150 pc measurements at 2.1 kpc averaging scale following Section 4.4. We find that the distribution of the weighted averages in the $\sigma_{\rm mol}$–$\Sigma_{\rm mol}$ plane resembles the distribution of the (original) high-resolution measurements very well, providing similar dynamic range in both $\sigma_{\rm mol}$ and $\Sigma_{\rm mol}$. However, the weighted averages show significantly lower dynamic range in $\alpha_{\rm vir}$. Note that the loci of constant $\alpha_{\rm vir}$ and $P_{\rm turb}$ are not valid for the weighted averages, because we take the weighted averages of the cloud-scale properties individually for each quantity, such that $\langle\alpha_{\rm vir}\rangle \not\propto \langle\sigma_{\rm mol}\rangle^2/\langle\Sigma_{\rm mol}\rangle$ and $\langle P_{\rm turb}\rangle \not\propto \langle\Sigma_{\rm mol}\rangle\langle\sigma_{\rm mol}\rangle^2$.

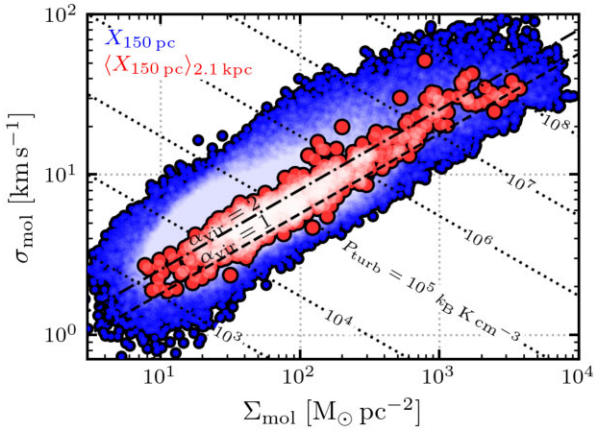

Figure A1. Molecular gas velocity dispersion ($\sigma_{\rm mol}$) against surface density ($\Sigma_{\rm mol}$) at 150 pc scale across 22 nearby galaxies. The blue points denote the original 150 pc resolution measurements, while the red points are the intensity-weighted averages obtained at 2.1 kpc apertures. The loci of constant virial parameter ($\alpha_{\rm vir}$) and internal turbulent pressure ($P_{\rm turb}$) are obtained assuming fixed cloud size, i.e. $\alpha_{\rm vir} \propto \sigma^2_{\rm mol}/\Sigma_{\rm mol}$ (equation 19), $P_{\rm turb} \propto \Sigma_{\rm mol}\sigma^2_{\rm mol}$ (equation 22), and are only valid for the original 150 pc measurements.

APPENDIX B: SPECTRAL STACKING

In order to recover more emission, in particular outside of galaxy centres, we perform spectral stacking of the HCN(1–0), HCO$^+$(1–0), and CS(2–1) cubes as in Schruba et al. (2011), Jiménez-Donaire et al. (2017, 2019), and Bešlić et al. (2021). The basic idea is that the spectral axis is matched with a known velocity field from a high significance prior, i.e. here CO(2–1). After shuffling the velocities, we average the spectra in bins defined by the galactocentric radius ($r_{\rm gal}$). We select five bins up to $r_{\rm gal} = 5$ kpc with bin widths of 2 kpc. In Fig. 3, we show the resulting stacked spectra (bottom panels) and stacked integrated intensities (a). A complete atlas of all galaxies is presented online. The spectral stacking results demonstrate that, despite the low detection rate at the pixel level across much of the molecular gas discs, we are able to recover significant emission of HCN(1–0) HCO$^+$(1–0), and CS(2–1) outside of galaxy centres via stacking at the expense of spatial information. We detect significant HCN emission out to 6 kpc in more than a third (9/25) of the galaxies compared to only 3 per cent for individual sightlines (Table B1), which demonstrates that stacking can successfully unveil HCN emission across most of the molecular gas discs. In particular, these results motivate the binning approach described in Section 4.5, where we average the HCN data in bins of $\langle W_{\rm CO(2-1)}\rangle$.

Table B1. HCN detection fraction across the 25 ALMOND galaxies.

$r_{\rm gal}$ (kpc)	Sightlines		Stacking	
	$N_{\rm det}/N_{\rm tot}$	$N_{\rm frac}$ (per cent)	$N_{\rm det}/N_{\rm tot}$	$N_{\rm frac}$ (per cent)
0–2	79/171	46.3	25/25	100
2–4	78/473	16.6	21/25	84
4–6	49/601	8.1	9/25	36
6–8	19/696	2.8	5/25	20
8–10	6/705	0.9	2/25	8

Note. HCN(1–0) detection fraction as a function galactocentric radius. $N_{\rm det}$ is the number of detected spectra for individual lines of sight (left), or the radially stacked spectra (right), where the S/N of the integrated intensity $>3\sigma$. $N_{\rm tot}$ is the total number of spectra inside the radial bin. $N_{\rm frac} = N_{\rm det}/N_{\rm tot}$ depicts the detection fraction.

The two approaches, binning and stacking, yield very similar results within ∼10 per cent, on average, and without bias (Gallagher et al. 2018b).

APPENDIX C: WEIGHTED AVERAGES

In Section 4.4, we explain the idea of computed intensity-weighted averages from the high-resolution CO data in order to compare with the coarse-scale dense gas observations using the following equation:

$$\langle X\rangle_{\rm Conv.} = \frac{(X\,W_{\rm CO(2-1)}) * \Omega}{W_{\rm CO(2-1)} * \Omega}, \tag{C1}$$

where X is the high-resolution quantity (e.g. $\Sigma_{\rm mol}$) and Ω is the convolution kernel to go from the high to the coarse resolution. Sun et al. (2020a) computed the weighted averages inside sharp apertures, such that

$$\langle X\rangle_{\rm Aper.} = \frac{\sum_{i\,\in\,\rm Aper.} X_i\,I_{{\rm CO(2-1)},i}}{\sum_{i\,\in\,\rm Aper.} I_{{\rm CO(2-1)},i}}. \tag{C2}$$

We compare the two methods for the galaxy NGC 2903 in Fig. C1. While both methods lead to very similar results in the centre or along the bar, there are large discrepancies for the adjacent pixels, where the aperture method produces much lower values. The aperture approach is not affected by any Gaussian kernel dilution and thus useful if the aperture-based weighted averages are used to study individually or for comparison with other aperture-based weighted averages. However, comparison with observations performed at or convolved to the averaging scale should only be done using the convolution-based method, which is symmetrically affected by beam dilution.

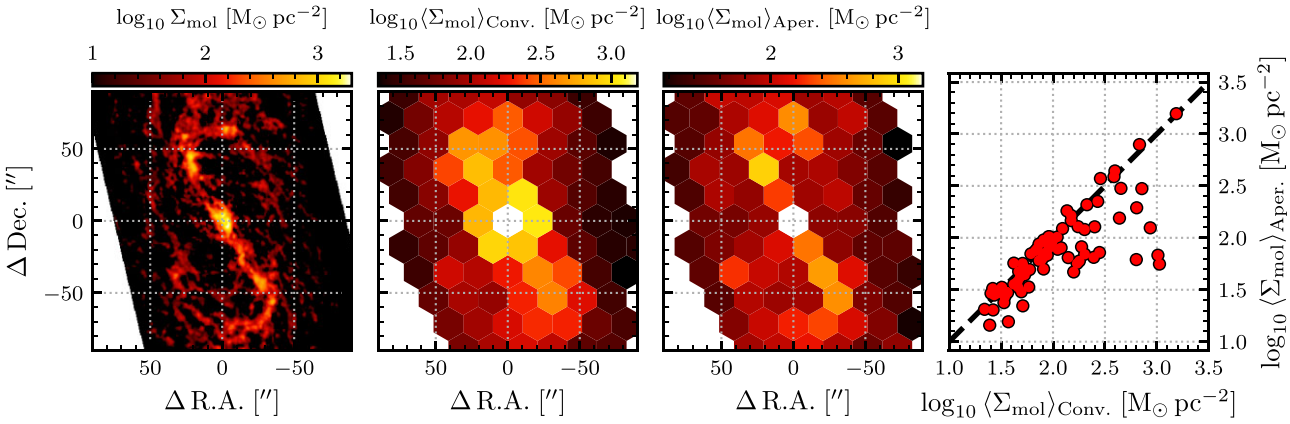

Figure C1. Comparison between different approaches of computing intensity-weighted averages. Left: molecular gas surface density ($\Sigma_{\rm mol}$) map of NGC 2903 at 75 pc resolution. Centre left: intensity-weighted average $\Sigma_{\rm mol}$ map at 1 kpc scale based on the Gaussian convolution as defined by equation (24). This method is employed in this work to compare with the native kpc-scale observations, i.e. the HCN data. Centre right: intensity-weighted averages based on sharp apertures defined as the hexagonal-shaped pixels. This method has been applied by e.g. Sun et al. (2020b). Right: pixel-by-pixel comparison between the aperture- and convolution-based approaches.

APPENDIX D: LINEAR REGRESSION

Linear regression of astronomical data is far from trivial and it is crucial to apply a linear fitting routine that is tailored to the science question and the noise properties of the data appropriately. Here, we ask the question of how the cloud-scale molecular gas properties (x data) affect the dense gas fraction and star formation efficiency (y data). Statistically speaking, the x data can be considered as the independent variable and the y data as the dependent variable, such that we seek to constrain $y(x) = b + m \cdot x$, where $b, m = \text{const}$. In principle one could also ask the inverted question, i.e. how x depends on y and thus constrain $x(y) = b' + m' \cdot y$ ($b', m' = \text{const}$). However, based on the formulated science question and given that the x data are detected significantly throughout most of the discs of all galaxies, as opposed to the y data, where about 50 per cent of the data points are censored (here we consider the fully processed, binned data that enter the fitting routine), it is well grounded to consider x as the independent variable.

We detect HCN significantly (S/N $\geq$ 3) only for about 50 per cent of the binned data points. Hence, we have many censored data points, which result in upper limits (HCN/CO) or lower limits (SFR/HCN). Although these data are not significant, it is still valuable information: we know with high certainty (99.7 per cent) that the emission of that data point cannot be larger than 3σ thus providing an upper limit. This information should be taken into account in the fitting routine to better constrain the assumed correlation and linear dependence. In addition, conversion to log–log scale can generate a bias in the estimated linear regression if censored data are not taken into account. Moreover, the true correlation most likely does not perfectly follow a linear correlation. Also, there is not necessarily a physical model that predicts a linear dependence (power law in linear scale) between the x and y data. Thus, we need to account for an intrinsic scatter in the correlation. Even more so, it is important to account for the intrinsic scatter and the data uncertainties separately, in order to get reasonable regression uncertainties (Kelly 2007).

Given our science question and the properties of our data, we want to use a linear regression tool that constrains the linear correlation of the dependent variable y as a function of the independent variable x, while taking into account measurement uncertainties in both variables, intrinsic scatter about the regression and censored y data.

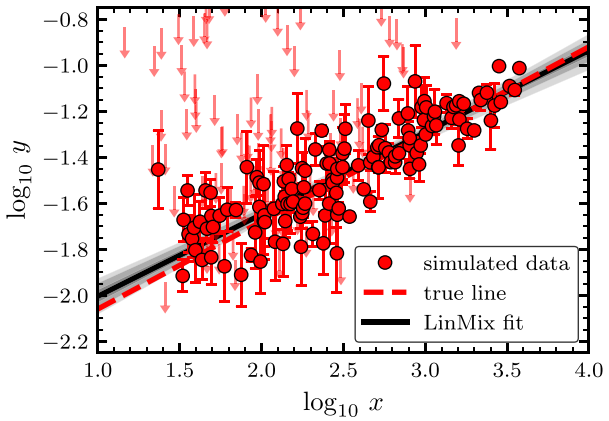

Figure D1. Bias estimation of the linear regression results. Adapted to the HCN/CO (y data) versus $\langle\Sigma_{\rm mol}\rangle$ (x data) correlation, we use the $\langle\Sigma_{\rm mol}\rangle$ data and create perfectly correlated (linear relation) y data, indicated by the red dotted line. Then we add Gaussian noise using the measurement uncertainties in HCN/CO, $\langle\Sigma_{\rm mol}\rangle$, and also add intrinsic scatter based on the estimated intrinsic scatter of the measured data. Finally, we apply the LinMix fitting routine to determine the best-fitting linear regression (black solid line) and the $\{1\sigma, 2\sigma, 3\sigma\}$ credibility regions (grey shaded areas).

All of these requirements are met by the PYTHON regression tool LinMix that implements the Bayesian approach to linear regression introduced by Kelly (2007). The tool assumes that the true data distribution is sampled from a superposition of Gaussians in x and y. It performs an MCMC simulation using the Gibbs sampler to explore the posterior distribution, i.e. the true distribution of the regression parameters. LinMix is capable of computing the Pearson correlation coefficient using both the significant and the censored data. Because of its statistical approach, the tool naturally finds trustworthy constraints on the regression parameters (intercept and slope) and also gives credibility areas, which we use to illustrate the uncertainty of the linear fits.

In astronomy it is very common to determine the power law of two astronomical quantities by converting the data from linear to logarithmic scale and fitting a line through the data. However, this procedure has some drawbacks. First, conversion to logarithmic

scale is only valid for positive data, and negative data (i.e. negative intensities that arise from the data reduction and represent mostly noise) is removed. As a consequence the log-scale data are biased towards positive values and thus bias the linear regression. We can mitigate this bias by using a linear regression tool that can handle censored data and thus takes the insignificant and negative data into account. Next, conversion to logarithmic scale produces asymmetric uncertainties, i.e. if the uncertainties are symmetric in linear scale, they appear shorter in the positive and larger in the negative direction. Again, this will bias the linear regression if the regression tool assumes symmetric uncertainties, because it either overestimates the uncertainties in positive direction or underestimates the uncertainties in negative direction. We note that the fitting routine applied here is affected by this bias. Though, we are not aware of any regression tool that can take into account asymmetric uncertainties in addition to handling censored data. Moreover, we estimated the expected log-scale-induced bias with the following simulation: to estimate the bias of the linear regression we start with the measured x data and produce perfectly correlated y data in logarithmic scale. Then we convert to linear scale and add Gaussian noise with amplitudes matching the measurement uncertainties. We also add Gaussian intrinsic scatter with amplitude as obtained from the linear regression of the observed data. Finally, we convert back to logarithmic scale and run the fitting algorithm. Fig. D1 shows the result customized to the HCN/CO versus $\langle W_{\rm CO(2-1)}\rangle$ correlation. We find that the determined linear regression slope is in fact biased towards lower values by about ∼10 per cent. In general, repeating this procedure for the other correlations, we find that the determined slopes are probably ∼10 per cent flatter compared to the true correlation, if it were perfectly correlated.

APPENDIX E: LINE-OF-SIGHT CORRELATIONS

In Section 4.5, we explain how we bin the data via $\langle W_{\rm CO(2-1)}\rangle$ to recover more emission, especially in the low $\langle W_{\rm CO(2-1)}\rangle$ regime. We show in Appendix B, that averaging data via a high significant prior, i.e. CO(2–1), is effectively unveiling more emission in the CO-emitting regions. As a consequence, the binning method allows us to constrain the relations between HCN/CO, SFR/HCN, and the cloud-scale properties with higher significance and with a higher weighting of the significant measurements. However, binning is expected to reduce the scatter in the binned quantities, i.e. HCN/CO and SFR/HCN, thus potentially reducing the scatter and increasing the measured correlation. Therefore, we also present the HCN/CO and SFR/HCN correlations with $\langle\Sigma_{\rm mol}\rangle$, $\langle\sigma_{\rm mol}\rangle$, $\langle\alpha_{\rm vir}\rangle$ using the individual line-of-sight (LOS) measurements (Fig. E1). We perform the linear regression on the LOS measurements analogous to Section 5, i.e. taking into account measurement uncertainties, intrinsic scatter, and censored data. Qualitatively, we find the same results for the LOS data as for the binned data, i.e. a positive (negative) correlation between HCN/CO (SFR/HCN) with the cloud-scale molecular gas properties. Certainly, we find lower correlations and higher scatter (Table E1). The lower correlation is however partly due to the higher

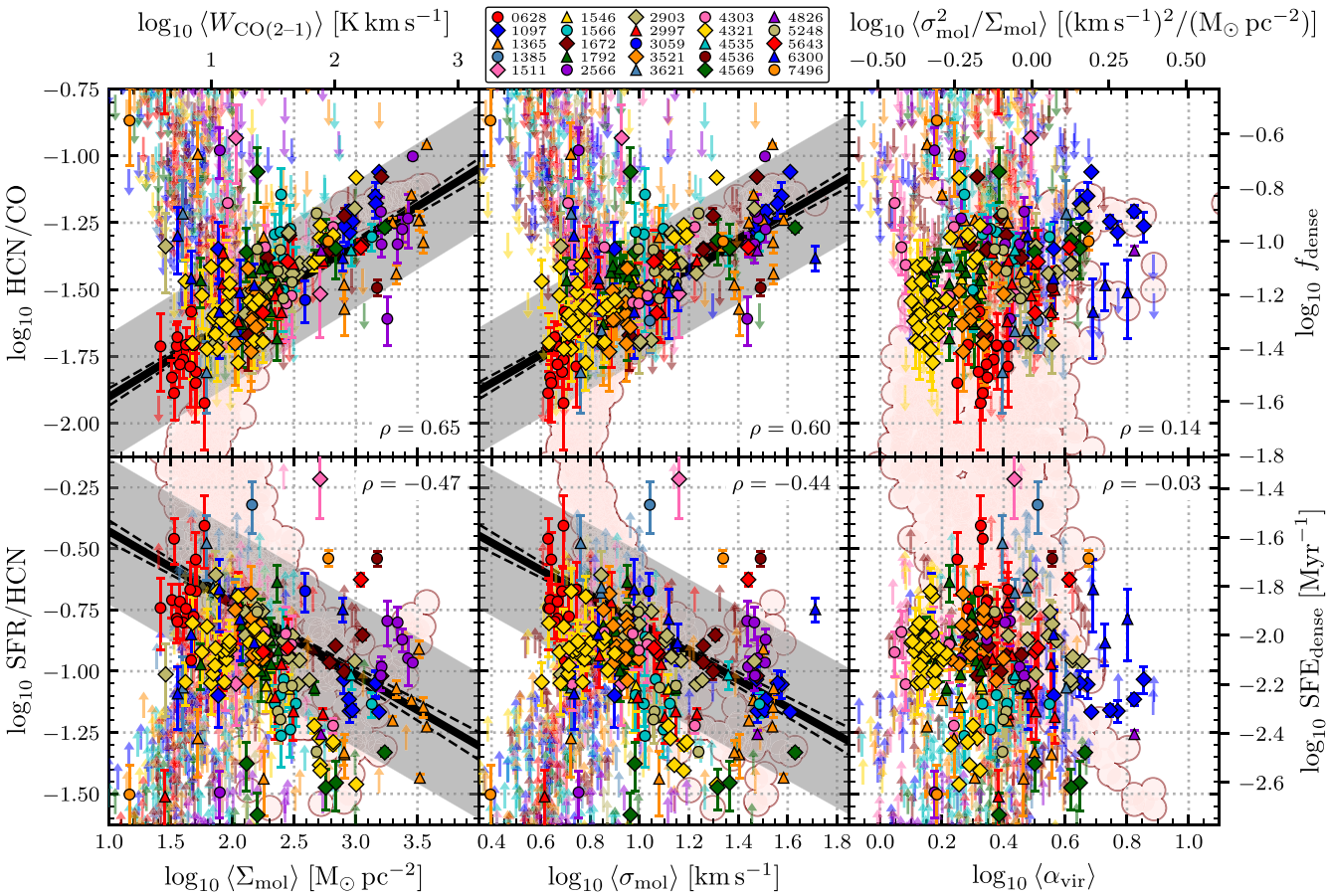

Figure E1. Analogous to Fig. 6, but for individual LOS measurements, i.e. without binning the data.

Table E1. HCN/CO and SFR/HCN correlations.

Cloud-scale Property	Data	HCN/CO				SFR/HCN			
		Slope (unc.)	Interc. (unc.)[a]	Corr. ρ (p)	Scatter	Slope (unc.)	Interc. (unc.)[a]	Corr. ρ (p)	Scatter
$\langle\Sigma_{\rm mol}\rangle$	Sightlines	0.28 (0.02)	−1.47 (0.01)	0.65 (0.0)	0.24	−0.29 (0.03)	−0.87 (0.02)	−0.47 (0.0)	0.30
	Binned	0.35 (0.02)	−1.49 (0.01)	0.88 (0.0)	0.11	−0.33 (0.04)	−0.84 (0.02)	−0.63 (0.0)	0.23
$\langle\sigma_{\rm mol}\rangle$	Sightlines	0.53 (0.04)	−1.48 (0.01)	0.60 (0.0)	0.23	−0.56 (0.06)	−0.87 (0.02)	−0.44 (0.0)	0.30
	Binned	0.66 (0.04)	−1.5 (0.01)	0.85 (0.0)	0.12	−0.63 (0.07)	−0.83 (0.02)	−0.60 (0.0)	0.23
$\langle\alpha_{\rm vir}\rangle$	Sightlines	...	...	0.14 (0.059)	...	...	...	−0.03 (0.643)	...
	Binned	...	...	0.21 (0.028)	...	...	...	−0.11 (0.226)	...
$\langle P_{\rm turb}\rangle$	Sightlines	0.13 (0.01)	−1.48 (0.01)	0.66 (0.0)	0.23	−0.14 (0.02)	−0.86 (0.02)	−0.48 (0.0)	0.30
	Binned	0.17 (0.01)	−1.49 (0.01)	0.88 (0.0)	0.11	−0.15 (0.02)	−0.83 (0.02)	−0.62 (0.0)	0.22

Note. Linear regression parameters analogous to Table I1 using lowres resolution configuration [HCN/CO, SFR/HCN at 2.1 kpc scale; molecular cloud properties ($\Sigma_{\rm mol}$, $\sigma_{\rm mol}$, $\alpha_{\rm vir}$, $P_{\rm turb}$) at 150 pc scale]. The table shows results obtained from individual LOS measurements corresponding to Fig. E1, as well as from binned data corresponding to Fig. 6. [a]Note that the intercept is measured at ca. the median of the respective cloud-scale property as described in Section 4.6.

statistical weight of the censored data (higher fraction of censored data taken into account in the fit).

APPENDIX F: VARIATION WITH RESOLUTION

We study the HCN/CO and SFR/HCN correlations as a function of the cloud-scale and large-scale resolutions choosing three cloud-scale physical resolutions (75, 120, and 150 pc) associated with the CO(2–1) data and three large-scale physical resolutions (1.0, 1.5, and 2.1 kpc) associated with the HCN data defined as the highest available common resolutions for galaxies inside 11.6 kpc ('highres'; three galaxies), 15.3 kpc ('midres'; nine galaxies), 23.4 kpc ('lowres'; 22 galaxies), respectively. In addition, we measure the correlations at the native angular resolutions of the CO(2–1) and HCN observations ('natres'; 22 galaxies). This defines the finest resolution configuration available but accesses different physical scales. The adopted resolution configurations are listed in Table F1.

The resolution configurations introduced above include different galaxy samples. In order to investigate the dependence of the correlations on the adopted resolutions for fixed samples of galaxies, we introduce subsamples of the natres, lowres, and midres configurations marked by the suffixed 'midtar' and 'hightar'. Midtar and hightar denote the subsample of galaxies that are included in the midres and highres sample, respectively. For instance lowres-hightar denotes the lowres resolution configuration (150 pc cloud scale, 2.1 kpc large scale), but only includes the subsample of three galaxies that are also included in highres. Fig. I1 shows a compilation of the HCN/CO and SFR/HCN correlations for the different resolution configurations. Complementary, Table I1 lists the linear regression results for all adopted resolution configurations.

Overall, we report similar HCN/CO and SFR/HCN correlations with the cloud-scale molecular gas properties across all resolution configurations, where the linear regression parameters are in agreement with each other if the galaxy sample is fixed. For varying samples of galaxies we observe significant deviations in the linear regression slope in some cases indicating galaxy-to-galaxy variations in the HCN/CO and SFR/HCN relations.

F1 HCN/CO versus molecular cloud properties

For the physically homogenized resolution configurations we consistently find strong positive correlations between HCN/CO and $\langle\Sigma_{\rm mol}\rangle$, $\langle\sigma_{\rm mol}\rangle$, and $\langle P_{\rm turb}\rangle$ (see Fig. I1, top, and Table I1, left) with Pearson correlation coefficients ranging from $\rho = 0.70$ to 0.82, 0.61 to 0.79, and 0.60 to 0.79, respectively, with p-values all smaller than 10^{-5}. For any given correlation (e.g. HCN/CO versus $\langle\Sigma_{\rm mol}\rangle$), the regression slopes vary among different physical resolution configurations and samples of galaxies, spanning $m_{\rm f,\,\Sigma} = 0.35$–$0.54$, $m_{\rm f,\,\sigma} = 0.51$–$0.93$, and $m_{\rm f,\,P} = 0.12$–0.24. Though, the linear regression parameters are in agreement within the 1σ uncertainties for fixed galaxy sample, meaning resolution does not significantly affect the observed relation between HCN/CO and the molecular cloud properties. For instance, for the HCN/CO versus $\langle\Sigma_{\rm mol}\rangle$ correlation we find $\rho = 0.70$, 0.73, and 0.81 and $m_{\rm f,\,\Sigma} = 0.35 \pm 0.09$, 0.37 ± 0.09, and 0.51 ± 0.10 for lowres-hightar, midres-hightar, and highres, respectively, all in agreement within the 1σ uncertainty limits. In contrast, for fixed resolution but varying sample we observe slopes deviating more than 1σ, e.g. midres and midres-hightar lead to $m_{\rm f,\,\Sigma} = 0.54 \pm 0.06$ and 0.37 ± 0.09. This points towards a galaxy-to-galaxy variation of the studied HCN/CO relations. However, these variations are not huge, because within the 2σ uncertainty range all resolution configuration are again consistent. In general, we find the trend of increasing correlation and steeper slopes for decreasing scale, i.e. at higher resolution, suggesting a small but systematic resolution dependence of the correlations. For the correlation of HCN/CO with the virial parameter ($\langle\alpha_{\rm vir}\rangle$) we find much lower correlation coefficients spanning $\rho = 0.17$–0.59 and p-values from 10^{-3} to 0.10 suggesting a weak positive correlation between HCN/CO and $\langle\alpha_{\rm vir}\rangle$. However, the stronger positive correlation seen in the hightar configurations is mainly produced by one galaxy, i.e. NGC 2903, and is not confidently seen in the other targets. Note also that the dynamic range in $\langle\alpha_{\rm vir}\rangle$ is barely 1 dex so that we might be insensitive to any potentially existing correlation with $\alpha_{\rm vir}$. In the end, we have no convincing evidence for a correlation between HCN/CO and $\langle\alpha_{\rm vir}\rangle$.

Above all, studying the HCN/CO correlations with molecular cloud properties at different resolutions leads to consistent results that confidently demonstrate a positive correlation between HCN/CO and $\langle\Sigma_{\rm mol}\rangle$, $\langle\sigma_{\rm mol}\rangle$, and $\langle P_{\rm turb}\rangle$, with the trend of increasing correlation with increasing resolution (decreasing scale). The correlation of HCN/CO with $\langle\alpha_{\rm vir}\rangle$ remains less clear. But consistently positive correlation coefficients point towards weak positive correlation between HCN/CO and $\langle\alpha_{\rm vir}\rangle$.

F2 SFR/HCN versus molecular cloud properties

We consistently find negative correlations between SFR/HCN and the cloud-scale properties $\langle\Sigma_{\rm mol}\rangle$, $\langle\sigma_{\rm mol}\rangle$, and $\langle P_{\rm turb}\rangle$ across all adopted resolution configurations (see Fig. I1, bottom, and Table I1, right, where Pearson correlation coefficients range from −0.45 to −0.63 ($\langle\Sigma_{\rm mol}\rangle$), −0.33 to −0.56 ($\langle\sigma_{\rm mol}\rangle$), and −0.32 to

Table F1. Resolutions.

Sample	Galaxies	Resolution			
		Lowres	Midres	Highres	Natres
		$\langle 150\,\mathrm{pc}\rangle_{2.1\,\mathrm{kpc}}$	$\langle 120\,\mathrm{pc}\rangle_{1.5\,\mathrm{kpc}}$	$\langle 75\,\mathrm{pc}\rangle_{1.0\,\mathrm{kpc}}$	$\langle \sim 1\,\mathrm{arcsec}\rangle_{\sim 20\,\mathrm{arcsec}}$
Full	NGC 0628, NGC 1097, NGC 1365, NGC 1385, NGC 1511, NGC 1546, NGC 1566, NGC 1672, NGC 1792, NGC 2566, NGC 2903, NGC 2997, NGC 3059, NGC 3521, NGC 3621, NGC 4303, NGC 4321, NGC 4535, NGC 4536, NGC 4569, NGC 4826, NGC 5248, NGC 5643, NGC 6300, NGC 7496	✓	✗	✗	✓
Midtar	NGC 0628, NGC 1097, NGC 1511, NGC 2903, NGC 2997, NGC 3521, NGC 3621, NGC 4321, NGC 4826, NGC 5248, NGC 5643, NGC 6300	✓	✓	✗	✓
Hightar	NGC 0628, NGC 2903, NGC 3621, NGC 4826, NGC 6300	✓	✓	✓	✓

Note. Column 2 shows the galaxies included in the respective (sub) samples resulting from the accessible galaxies at given resolutions. The full sample can reach 150 pc cloud-scale and 2.1 kpc kpc-scale resolution. For the midtar and hightar samples the accessible resolutions are 120 pc cloud-scale, 1.5 kpc kpc-scale and 75 pc cloud-scale, 1.0 kpc kpc-scale, respectively.

-0.59 ($\langle P_{\mathrm{turb}}\rangle$) and slopes span $m_{\mathrm{S},\Sigma} = -0.23$ to -0.49, $m_{\mathrm{S},\sigma} = -0.27$ to -0.78, and $m_{\mathrm{S,P}} = -0.06$ to -0.21 for the physically homogenized resolutions. Compared to the HCN/CO correlations, the strength of the SFR/HCN correlation is about 0.2 lower and the intrinsic scatter about the median regression line is 2–3 times as large, indicating a weaker correlation and suggesting potentially other physical processes in setting SFR/HCN. Still, we find strong evidence for a negative correlation between SFR/HCN and the aforementioned cloud properties at all resolutions. Moreover, the lack of correlation between SFR/HCN and $\langle \alpha_{\mathrm{vir}}\rangle$ found at the lowest resolution (lowres) is also supported at higher resolution. In fact, the correlation coefficients are $|\rho| < 0.2$ at maximum with p-values as large as 0.98 indicating a very weak negative or no correlation with the virial parameter. The dependence on resolution follows similar systematics as of HCN/CO meaning the correlation increases and the slope steepens for increasing resolution, i.e. decreasing physical scale.

Overall, based on different resolution configurations we find strong evidence for a negative correlation between SFR/HCN tracing $\mathrm{SFE}_{\mathrm{dense}}$ and molecular cloud properties $\langle \Sigma_{\mathrm{mol}}\rangle$, $\langle \sigma_{\mathrm{mol}}\rangle$, and $\langle P_{\mathrm{turb}}\rangle$, where the correlation and steepness of the slope seem to increase with increasing resolution. Furthermore, we find no correlation between SFR/HCN and $\langle \alpha_{\mathrm{vir}}\rangle$. The opposite sign in the correlations compared to HCN/CO points towards an anticorrelation between SFR/HCN and HCN/CO and thus $\mathrm{SFE}_{\mathrm{dense}}$ and $\mathrm{SFE}_{\mathrm{dense}}$.

APPENDIX G: HCO$^+$/CO AND SFR/HCO$^+$ CORRELATIONS

In analogy to the HCN/CO and the SFR/HCN correlations we show the results of the determined HCO$^+$/CO and SFR/HCO$^+$ correlations in Fig. I2 and in Table I2. First and foremost, we find the same correlations and anticorrelations between the HCO$^+$ spectroscopic measurements with the molecular cloud properties as of HCN with similar correlation coefficients, slopes, and scatter. Thus, at 1–2 kpc resolution, HCN(1–0) and HCO$^+$(1–0) are sensitive to the same density variations.

APPENDIX H: CS/CO AND SFR/CS CORRELATIONS

In analogy to the HCN/CO and the SFR/HCN correlations we show the results of the determined CS/CO and SFR/CS correlations in Fig. I3 and in Table I3. Despite the much lower S/N of the CS data we recover the same trends with cloud-scale molecular gas properties as seen for HCN or HCO$^+$, though with larger uncertainties.

APPENDIX I: INDIVIDUAL GALAXIES

In Fig. I4, we show the same HCN/CO against $\langle \Sigma_{\mathrm{mol}}\rangle$ correlations as in Fig. 6 (left-hand panels), but for each galaxy individually.

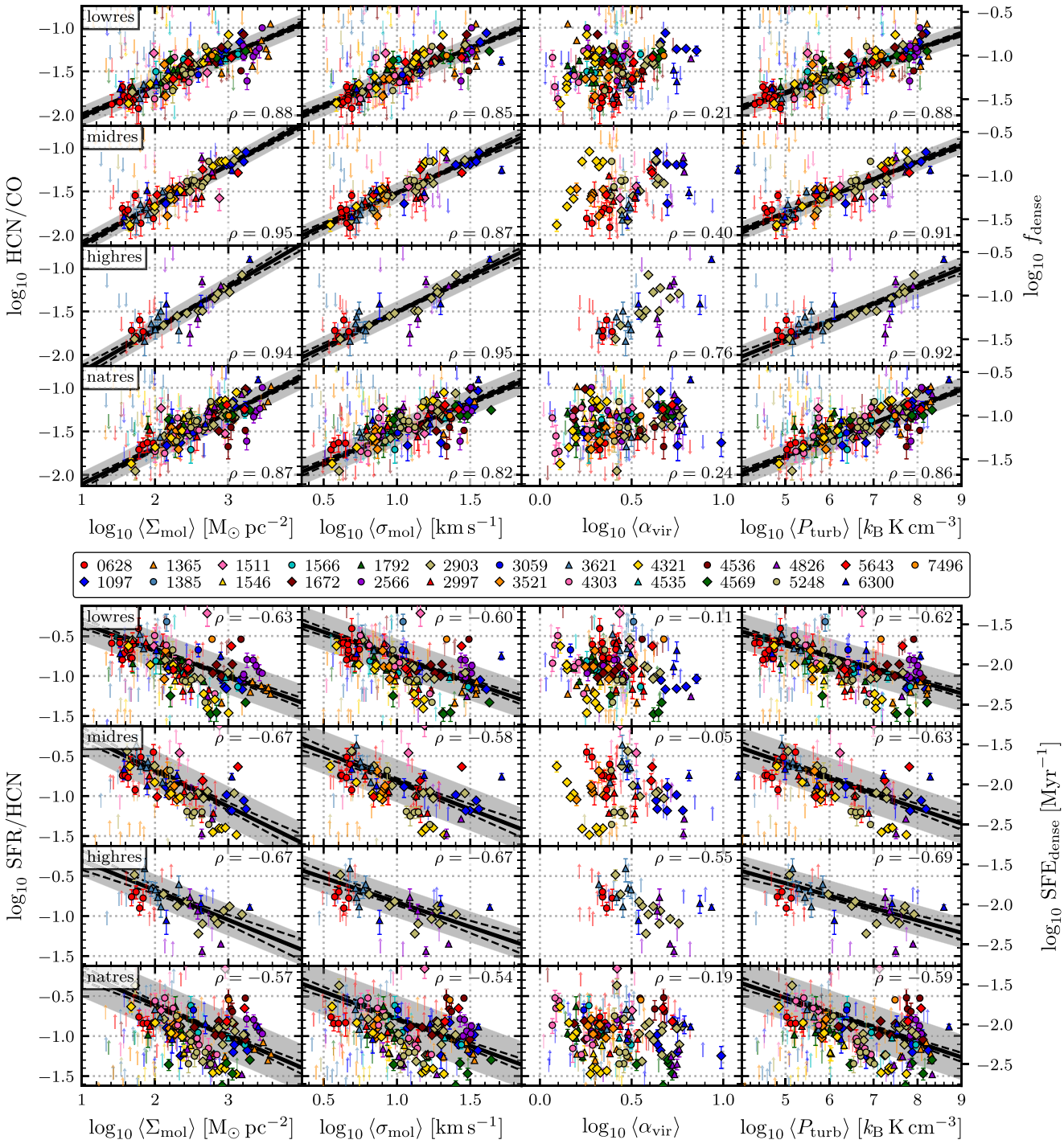

Figure I1. HCN/CO (top) versus $\langle X\rangle$ and SFR/HCN (bottom) versus $\langle X\rangle$ at different resolutions listed in Table F1. The solid line shows the best-fitting line where the dotted line is the 1σ uncertainty. The grey shaded area indicates the scatter of the significant data about the fit line.

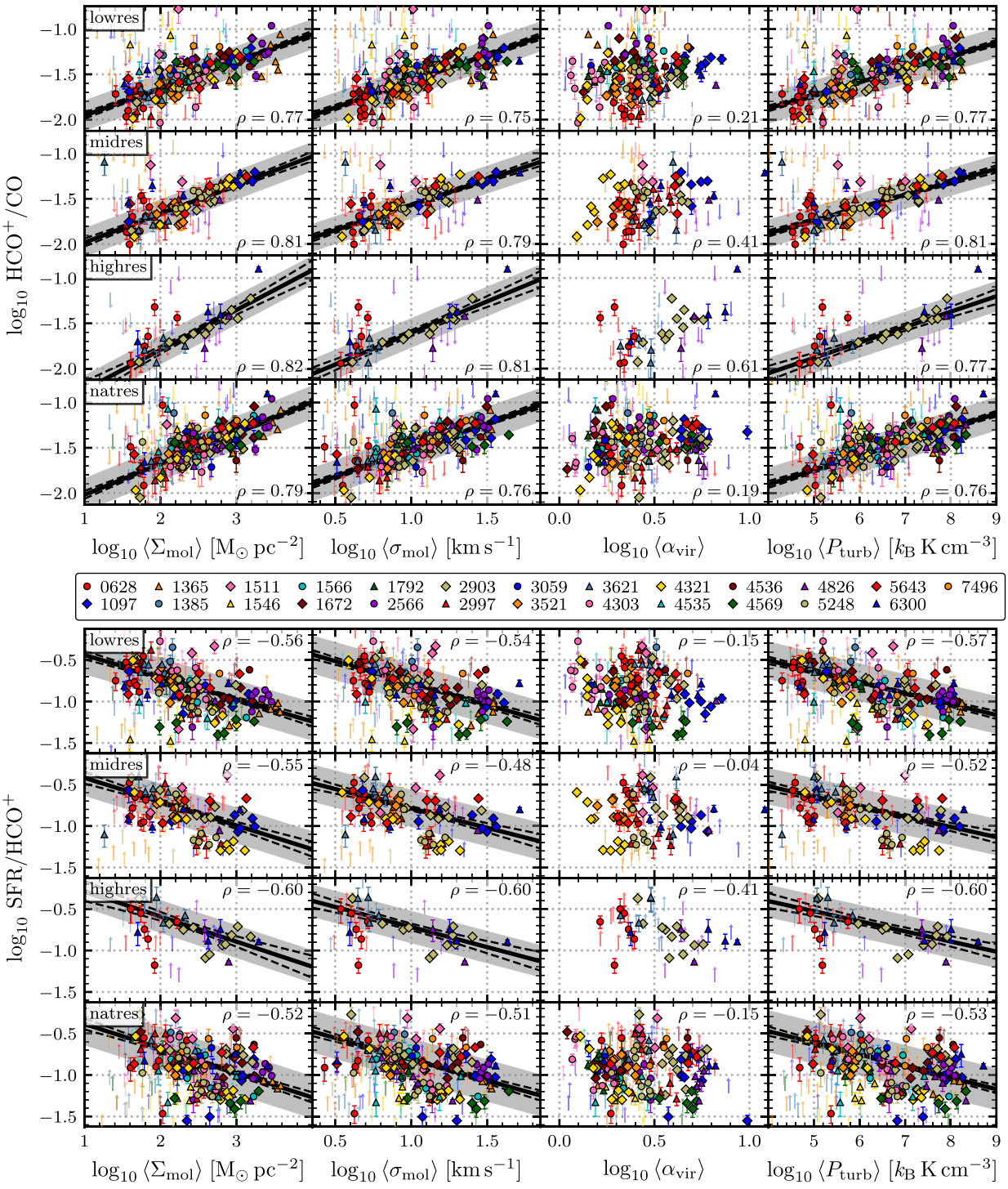

Figure 12. $\mathrm{HCO^+/CO}$ (top) versus $\langle X \rangle$ and $\mathrm{SFR/HCO^+}$ (bottom) versus $\langle X \rangle$ at different resolutions listed in Table F1.

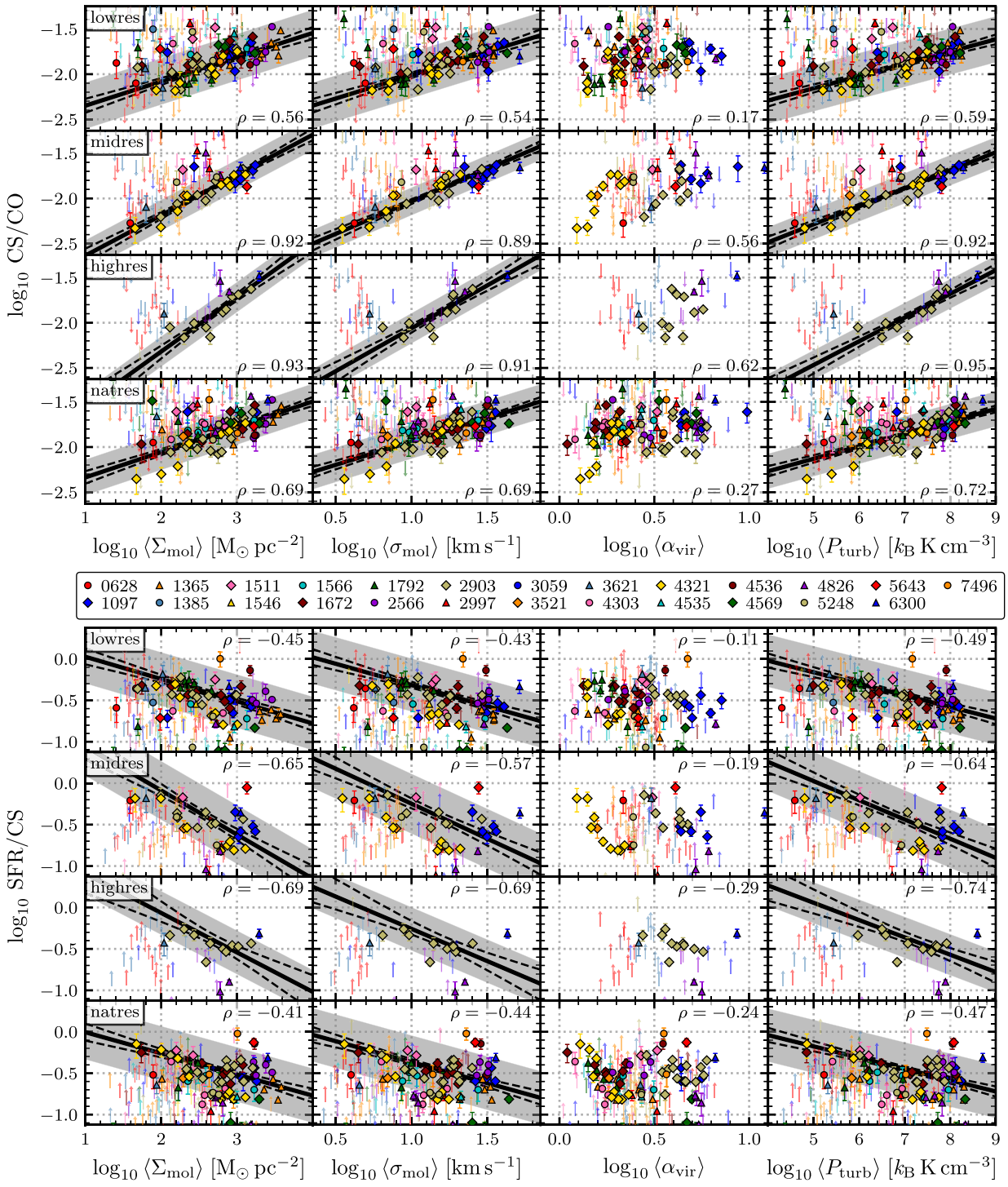

Figure I3. CS/CO (top) versus $\langle X \rangle$ and SFR/CS (bottom) versus $\langle X \rangle$ at different resolutions listed in Table F1.

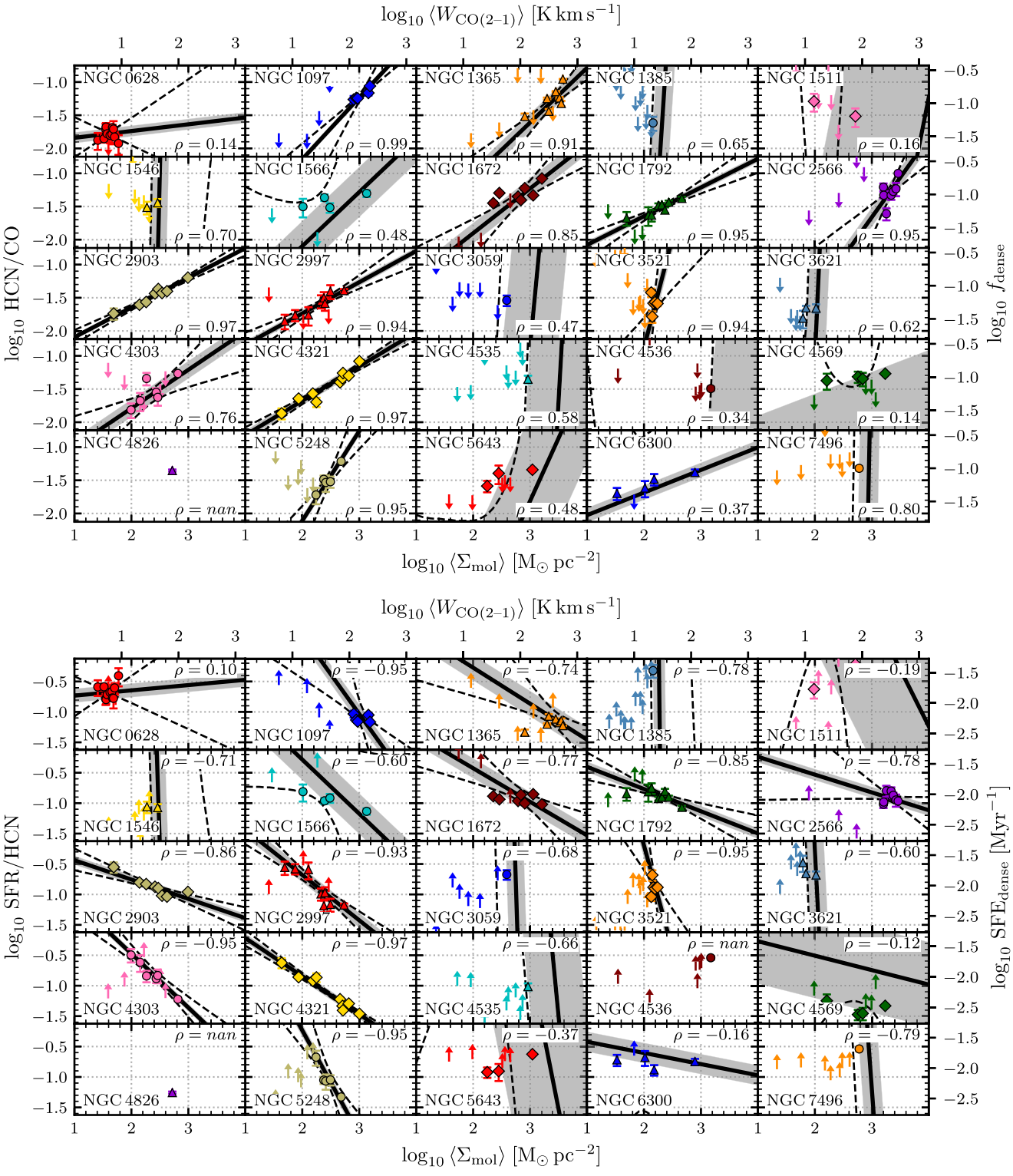

Figure I4. HCN/CO (top) and SFR/HCN (bottom) versus $\langle\Sigma_{\rm mol}\rangle$ at 2.1 kpc and 150 pc scales, plotted and fitted individually for each galaxy. The solid line shows the best-fitting line while the dotted line is the 1σ uncertainty. The grey shaded area indicates the scatter of the significant data about the fit line.

Table I1. HCN/CO and SFR/HCN correlations.

Cloud-scale Property	Resolution	HCN/CO				SFR/HCN			
		Slope (unc.)	Interc. (unc.)	Corr. ρ (p)	Scatter	Slope (unc.)	Interc. (unc.)	Corr. ρ (p)	Scatter
$\langle\Sigma_{\rm mol}\rangle$	Natres	0.41 (0.03)	− 1.49 (0.01)	0.87 (0.0)	0.14	− 0.39 (0.05)	− 0.81 (0.03)	− 0.57 (0.0)	0.29
$\langle\Sigma_{\rm mol}\rangle$	Natres-midtar	0.5 (0.03)	− 1.46 (0.01)	0.94 (0.0)	0.12	− 0.46 (0.07)	− 0.85 (0.03)	− 0.60 (0.0)	0.29
$\langle\Sigma_{\rm mol}\rangle$	Natres-hightar	0.5 (0.04)	− 1.47 (0.02)	0.95 (0.0)	0.10	− 0.44 (0.1)	− 0.86 (0.05)	− 0.66 (0.0)	0.24
$\langle\Sigma_{\rm mol}\rangle$	Lowres	0.35 (0.02)	− 1.49 (0.01)	0.88 (0.0)	0.11	− 0.33 (0.04)	− 0.84 (0.02)	− 0.63 (0.0)	0.23
$\langle\Sigma_{\rm mol}\rangle$	Lowres-midtar	0.43 (0.02)	− 1.44 (0.01)	0.95 (0.0)	0.10	− 0.42 (0.05)	− 0.93 (0.03)	− 0.7 (0.0)	0.20
$\langle\Sigma_{\rm mol}\rangle$	Lowres-hightar	0.39 (0.03)	− 1.43 (0.02)	0.97 (0.0)	0.07	− 0.31 (0.06)	− 0.90 (0.04)	− 0.73 (0.0)	0.13
$\langle\Sigma_{\rm mol}\rangle$	Midres	0.46 (0.03)	− 1.43 (0.01)	0.95 (0.0)	0.10	− 0.45 (0.06)	− 0.91 (0.03)	− 0.67 (0.0)	0.25
$\langle\Sigma_{\rm mol}\rangle$	Midres-hightar	0.41 (0.04)	− 1.43 (0.02)	0.92 (0.0)	0.10	− 0.37 (0.08)	− 0.89 (0.05)	− 0.66 (0.0)	0.19
$\langle\Sigma_{\rm mol}\rangle$	Highres	0.49 (0.04)	− 1.46 (0.02)	0.94 (0.0)	0.12	− 0.37 (0.08)	− 0.86 (0.04)	− 0.67 (0.0)	0.20
$\langle\sigma_{\rm mol}\rangle$	Natres	0.69 (0.05)	− 1.45 (0.01)	0.82 (0.0)	0.15	− 0.67 (0.09)	− 0.85 (0.03)	− 0.54 (0.0)	0.29
$\langle\sigma_{\rm mol}\rangle$	Natres-midtar	0.80 (0.06)	− 1.40 (0.02)	0.88 (0.0)	0.14	− 0.74 (0.13)	− 0.90 (0.04)	− 0.56 (0.0)	0.29
$\langle\sigma_{\rm mol}\rangle$	Natres-hightar	0.81 (0.09)	− 1.38 (0.02)	0.9 (0.0)	0.13	− 0.71 (0.17)	− 0.93 (0.05)	− 0.61 (0.0)	0.26
$\langle\sigma_{\rm mol}\rangle$	Lowres	0.66 (0.04)	− 1.5 (0.01)	0.85 (0.0)	0.12	− 0.63 (0.07)	− 0.83 (0.02)	− 0.60 (0.0)	0.23
$\langle\sigma_{\rm mol}\rangle$	Lowres-midtar	0.69 (0.05)	− 1.49 (0.01)	0.88 (0.0)	0.10	− 0.65 (0.10)	− 0.87 (0.03)	− 0.61 (0.0)	0.22
$\langle\sigma_{\rm mol}\rangle$	Lowres-hightar	0.58 (0.07)	− 1.52 (0.02)	0.9 (0.0)	0.08	− 0.46 (0.1)	− 0.83 (0.03)	− 0.68 (0.0)	0.13
$\langle\sigma_{\rm mol}\rangle$	Midres	0.75 (0.06)	− 1.44 (0.02)	0.87 (0.0)	0.11	− 0.71 (0.11)	− 0.88 (0.03)	− 0.58 (0.0)	0.27
$\langle\sigma_{\rm mol}\rangle$	Midres-hightar	0.63 (0.07)	− 1.48 (0.02)	0.89 (0.0)	0.10	− 0.56 (0.13)	− 0.84 (0.04)	− 0.64 (0.0)	0.19
$\langle\sigma_{\rm mol}\rangle$	Highres	0.81 (0.07)	− 1.42 (0.02)	0.95 (0.0)	0.12	− 0.62 (0.13)	− 0.89 (0.04)	− 0.67 (0.0)	0.19
$\langle\alpha_{\rm vir}\rangle$	Natres	...	...	0.24 (0.01)	...	...	...	− 0.19 (0.037)	...
$\langle\alpha_{\rm vir}\rangle$	Natres-midtar	...	...	0.41 (0.001)	...	...	...	− 0.15 (0.233)	...
$\langle\alpha_{\rm vir}\rangle$	Natres-hightar	...	...	0.73 (0.0)	...	...	...	− 0.53 (0.003)	...
$\langle\alpha_{\rm vir}\rangle$	Lowres	...	...	0.21 (0.028)	...	...	...	− 0.11 (0.226)	...
$\langle\alpha_{\rm vir}\rangle$	Lowres-midtar	...	...	0.46 (0.0)	...	...	...	− 0.12 (0.325)	...
$\langle\alpha_{\rm vir}\rangle$	Lowres-hightar	...	...	0.76 (0.0)	...	...	...	− 0.53 (0.005)	...
$\langle\alpha_{\rm vir}\rangle$	Midres	...	...	0.4 (0.001)	...	...	...	− 0.05 (0.666)	...
$\langle\alpha_{\rm vir}\rangle$	Midres-hightar	...	...	0.77 (0.0)	...	...	...	− 0.54 (0.005)	...
$\langle\alpha_{\rm vir}\rangle$	Highres	...	...	0.76 (0.0)	...	...	...	− 0.55 (0.002)	...
$\langle P_{\rm turb}\rangle$	Natres	0.19 (0.01)	− 1.5 (0.01)	0.86 (0.0)	0.14	− 0.19 (0.02)	− 0.80 (0.03)	− 0.59 (0.0)	0.28
$\langle P_{\rm turb}\rangle$	Natres-midtar	0.22 (0.01)	− 1.49 (0.02)	0.92 (0.0)	0.12	− 0.2 (0.03)	− 0.82 (0.04)	− 0.6 (0.0)	0.28
$\langle P_{\rm turb}\rangle$	Natres-hightar	0.22 (0.02)	− 1.52 (0.02)	0.95 (0.0)	0.10	− 0.19 (0.04)	− 0.82 (0.05)	− 0.68 (0.0)	0.23
$\langle P_{\rm turb}\rangle$	Lowres	0.17 (0.01)	− 1.49 (0.01)	0.88 (0.0)	0.11	− 0.15 (0.02)	− 0.83 (0.02)	− 0.62 (0.0)	0.22
$\langle P_{\rm turb}\rangle$	Lowres-midtar	0.18 (0.01)	− 1.47 (0.01)	0.92 (0.0)	0.10	− 0.17 (0.02)	− 0.88 (0.03)	− 0.64 (0.0)	0.21
$\langle P_{\rm turb}\rangle$	Lowres-hightar	0.15 (0.01)	− 1.5 (0.02)	0.94 (0.0)	0.08	− 0.12 (0.02)	− 0.84 (0.03)	− 0.71 (0.0)	0.13
$\langle P_{\rm turb}\rangle$	Midres	0.2 (0.01)	− 1.46 (0.01)	0.91 (0.0)	0.11	− 0.19 (0.03)	− 0.87 (0.03)	− 0.63 (0.0)	0.26
$\langle P_{\rm turb}\rangle$	Midres-hightar	0.16 (0.02)	− 1.49 (0.02)	0.89 (0.0)	0.11	− 0.15 (0.03)	− 0.84 (0.04)	− 0.67 (0.0)	0.19
$\langle P_{\rm turb}\rangle$	Highres	0.20 (0.02)	− 1.51 (0.02)	0.92 (0.0)	0.14	− 0.15 (0.03)	− 0.82 (0.04)	− 0.69 (0.0)	0.19

Note. HCN/CO (tracing $f_{\rm dense}$) and SFR/HCN (tracing $\rm SFE_{dense}$) versus molecular cloud properties – $\Sigma_{\rm mol}$, $\sigma_{\rm mol}$, $\alpha_{\rm vir}$, and $P_{\rm turb}$ – correlations for all adopted resolution configurations. Columns 3 and 4 list the slope and intercept with its uncertainty estimates as determined by the linear regression. Column 5 shows the Pearson correlation coefficient ρ and its corresponding p-value. Column 6 displays the scatter, i.e. the standard deviation of the fit residuals of the significant (S/R > 3) data. Because of lack of correlation between HCN/CO or SFR/HCN and the virial parameter, we do not show linear regression results, but only list the correlation coefficient and p-value based on the significant data points. Note that for the other cloud-scale properties, the correlation coefficient (and the p-value) is determined using both the censored and the significant data.

Table I2. HCO^+/CO and SFR/HCO^+ correlations.

Cloud-scale Property	Res. config.	HCO^+/CO				SFR/HCO^+			
		Slope (unc.)	Interc. (unc.)	Corr. ρ (p)	Scatter	Slope (unc.)	Interc. (unc.)	Corr. ρ (p)	Scatter
$\langle\Sigma_{mol}\rangle$	Natres	0.34 (0.03)	− 1.51 (0.01)	0.79 (0.0)	0.18	− 0.3 (0.04)	− 0.83 (0.02)	− 0.52 (0.0)	0.26
$\langle\Sigma_{mol}\rangle$	Natres-midtar	0.39 (0.04)	− 1.52 (0.02)	0.82 (0.0)	0.19	− 0.32 (0.06)	− 0.83 (0.03)	− 0.51 (0.0)	0.26
$\langle\Sigma_{mol}\rangle$	Natres-hightar	0.39 (0.05)	− 1.55 (0.03)	0.82 (0.0)	0.17	− 0.3 (0.09)	− 0.79 (0.04)	− 0.53 (0.0)	0.24
$\langle\Sigma_{mol}\rangle$	Lowres	0.3 (0.02)	− 1.51 (0.01)	0.77 (0.0)	0.17	− 0.27 (0.03)	− 0.84 (0.02)	− 0.56 (0.0)	0.23
$\langle\Sigma_{mol}\rangle$	Lowres-midtar	0.33 (0.03)	− 1.51 (0.02)	0.84 (0.0)	0.15	− 0.31 (0.05)	− 0.87 (0.03)	− 0.6 (0.0)	0.20
$\langle\Sigma_{mol}\rangle$	Lowres-hightar	0.3 (0.05)	− 1.53 (0.03)	0.76 (0.0)	0.12	− 0.21 (0.06)	− 0.80 (0.04)	− 0.58 (0.0)	0.14
$\langle\Sigma_{mol}\rangle$	Midres	0.32 (0.03)	− 1.51 (0.02)	0.81 (0.0)	0.16	− 0.29 (0.05)	− 0.85 (0.03)	− 0.55 (0.0)	0.22
$\langle\Sigma_{mol}\rangle$	Midres-hightar	0.22 (0.07)	− 1.56 (0.05)	0.52 (0.0)	0.20	− 0.15 (0.07)	− 0.78 (0.05)	− 0.39 (0.01)	0.19
$\langle\Sigma_{mol}\rangle$	Highres	0.44 (0.06)	− 1.57 (0.03)	0.82 (0.0)	0.16	− 0.30 (0.08)	− 0.74 (0.04)	− 0.60 (0.0)	0.20
$\langle\sigma_{mol}\rangle$	Natres	0.59 (0.05)	− 1.47 (0.01)	0.76 (0.0)	0.19	− 0.51 (0.07)	− 0.86 (0.02)	− 0.51 (0.0)	0.25
$\langle\sigma_{mol}\rangle$	Natres-midtar	0.63 (0.06)	− 1.47 (0.02)	0.79 (0.0)	0.20	− 0.51 (0.10)	− 0.86 (0.03)	− 0.48 (0.0)	0.26
$\langle\sigma_{mol}\rangle$	Natres-hightar	0.6 (0.1)	− 1.49 (0.03)	0.76 (0.0)	0.18	− 0.43 (0.14)	− 0.84 (0.05)	− 0.46 (0.0)	0.25
$\langle\sigma_{mol}\rangle$	Lowres	0.58 (0.05)	− 1.52 (0.01)	0.75 (0.0)	0.17	− 0.53 (0.07)	− 0.83 (0.02)	− 0.54 (0.0)	0.23
$\langle\sigma_{mol}\rangle$	Lowres-midtar	0.58 (0.05)	− 1.55 (0.01)	0.83 (0.0)	0.15	− 0.50 (0.09)	− 0.83 (0.03)	− 0.54 (0.0)	0.20
$\langle\sigma_{mol}\rangle$	Lowres-hightar	0.48 (0.08)	− 1.6 (0.02)	0.79 (0.0)	0.11	− 0.35 (0.09)	− 0.76 (0.03)	− 0.62 (0.0)	0.13
$\langle\sigma_{mol}\rangle$	Midres	0.56 (0.05)	− 1.51 (0.02)	0.79 (0.0)	0.15	− 0.47 (0.1)	− 0.84 (0.03)	− 0.48 (0.0)	0.22
$\langle\sigma_{mol}\rangle$	Midres-hightar	0.42 (0.10)	− 1.57 (0.04)	0.62 (0.0)	0.19	− 0.27 (0.11)	− 0.76 (0.04)	− 0.42 (0.006)	0.18
$\langle\sigma_{mol}\rangle$	Highres	0.7 (0.10)	− 1.54 (0.03)	0.81 (0.0)	0.16	− 0.48 (0.12)	− 0.77 (0.04)	− 0.60 (0.0)	0.19
$\langle\alpha_{vir}\rangle$	Natres	...	...	0.19 (0.023)	...	...	...	− 0.15 (0.069)	...
$\langle\alpha_{vir}\rangle$	Natres-midtar	...	...	0.36 (0.001)	...	...	...	− 0.17 (0.115)	...
$\langle\alpha_{vir}\rangle$	Natres-hightar	...	...	0.34 (0.044)	...	...	...	− 0.26 (0.134)	...
$\langle\alpha_{vir}\rangle$	Lowres	...	...	0.21 (0.013)	...	...	...	− 0.15 (0.069)	...
$\langle\alpha_{vir}\rangle$	Lowres-midtar	...	...	0.44 (0.0)	...	...	...	− 0.14 (0.22)	...
$\langle\alpha_{vir}\rangle$	Lowres-hightar	...	...	0.78 (0.0)	...	...	...	− 0.53 (0.003)	...
$\langle\alpha_{vir}\rangle$	Midres	...	...	0.41 (0.0)	...	...	...	− 0.04 (0.738)	...
$\langle\alpha_{vir}\rangle$	Midres-hightar	...	...	0.61 (0.001)	...	...	...	− 0.3 (0.122)	...
$\langle\alpha_{vir}\rangle$	Highres	...	...	0.61 (0.001)	...	...	...	− 0.41 (0.034)	...
$\langle P_{turb}\rangle$	Natres	0.16 (0.01)	− 1.51 (0.01)	0.76 (0.0)	0.19	− 0.14 (0.02)	− 0.82 (0.02)	− 0.53 (0.0)	0.25
$\langle P_{turb}\rangle$	Natres-midtar	0.17 (0.02)	− 1.54 (0.02)	0.8 (0.0)	0.19	− 0.14 (0.03)	− 0.81 (0.03)	− 0.51 (0.0)	0.26
$\langle P_{turb}\rangle$	Natres-hightar	0.16 (0.03)	− 1.59 (0.03)	0.78 (0.0)	0.18	− 0.13 (0.04)	− 0.77 (0.04)	− 0.54 (0.0)	0.24
$\langle P_{turb}\rangle$	Lowres	0.14 (0.01)	− 1.51 (0.01)	0.77 (0.0)	0.17	− 0.13 (0.02)	− 0.83 (0.02)	− 0.57 (0.0)	0.23
$\langle P_{turb}\rangle$	Lowres-midtar	0.15 (0.01)	− 1.54 (0.01)	0.84 (0.0)	0.15	− 0.13 (0.02)	− 0.84 (0.02)	− 0.59 (0.0)	0.20
$\langle P_{turb}\rangle$	Lowres-hightar	0.13 (0.02)	− 1.58 (0.02)	0.83 (0.0)	0.10	− 0.09 (0.02)	− 0.77 (0.03)	− 0.67 (0.0)	0.13
$\langle P_{turb}\rangle$	Midres	0.14 (0.01)	− 1.53 (0.02)	0.81 (0.0)	0.15	− 0.12 (0.02)	− 0.83 (0.03)	− 0.52 (0.0)	0.22
$\langle P_{turb}\rangle$	Midres-hightar	0.1 (0.03)	− 1.59 (0.04)	0.58 (0.0)	0.19	− 0.07 (0.03)	− 0.76 (0.04)	− 0.44 (0.004)	0.18
$\langle P_{turb}\rangle$	Highres	0.17 (0.03)	− 1.63 (0.04)	0.77 (0.0)	0.17	− 0.12 (0.03)	− 0.71 (0.04)	− 0.6 (0.0)	0.20

Note. Analogous to Table I1 but for HCO^+(1–0).

Table I3. CS/CO and SFR/CS correlations.

MC prop.	Res. config.	CS/CO				SFR/CS			
		Slope (unc.)	Interc. (unc.)	Corr. ρ (p)	Scatter	Slope (unc.)	Interc. (unc.)	Corr. ρ (p)	Scatter
$\langle\Sigma_{\rm mol}\rangle$	Natres	0.28 (0.04)	− 1.92 (0.02)	0.69 (0.0)	0.20	− 0.26 (0.06)	− 0.39 (0.03)	− 0.41 (0.0)	0.33
$\langle\Sigma_{\rm mol}\rangle$	Natres-midtar	0.42 (0.05)	− 1.95 (0.03)	0.82 (0.0)	0.18	− 0.4 (0.09)	− 0.37 (0.04)	− 0.54 (0.0)	0.32
$\langle\Sigma_{\rm mol}\rangle$	Natres-hightar	0.45 (0.08)	− 1.96 (0.04)	0.84 (0.0)	0.17	− 0.36 (0.12)	− 0.38 (0.06)	− 0.58 (0.0)	0.26
$\langle\Sigma_{\rm mol}\rangle$	Lowres	0.27 (0.05)	− 1.95 (0.03)	0.56 (0.0)	0.26	− 0.27 (0.06)	− 0.38 (0.03)	− 0.45 (0.0)	0.32
$\langle\Sigma_{\rm mol}\rangle$	Lowres-midtar	0.45 (0.1)	− 1.96 (0.05)	0.60 (0.0)	0.32	− 0.45 (0.11)	− 0.41 (0.05)	− 0.55 (0.0)	0.35
$\langle\Sigma_{\rm mol}\rangle$	Lowres-hightar	0.36 (0.08)	− 1.92 (0.04)	0.81 (0.0)	0.17	− 0.32 (0.11)	− 0.41 (0.06)	− 0.62 (0.0)	0.21
$\langle\Sigma_{\rm mol}\rangle$	Midres	0.45 (0.05)	− 1.96 (0.02)	0.92 (0.0)	0.17	− 0.53 (0.10)	− 0.35 (0.05)	− 0.65 (0.0)	0.35
$\langle\Sigma_{\rm mol}\rangle$	Midres-hightar	0.50 (0.07)	− 1.95 (0.03)	0.97 (0.0)	0.15	− 0.51 (0.16)	− 0.37 (0.07)	− 0.71 (0.0)	0.26
$\langle\Sigma_{\rm mol}\rangle$	Highres	0.60 (0.09)	− 2.02 (0.04)	0.93 (0.0)	0.17	− 0.48 (0.16)	− 0.30 (0.07)	− 0.69 (0.0)	0.26
$\langle\sigma_{\rm mol}\rangle$	Natres	0.52 (0.07)	− 1.89 (0.02)	0.69 (0.0)	0.19	− 0.51 (0.11)	− 0.42 (0.03)	− 0.44 (0.0)	0.32
$\langle\sigma_{\rm mol}\rangle$	Natres-midtar	0.71 (0.1)	− 1.90 (0.03)	0.79 (0.0)	0.18	− 0.67 (0.16)	− 0.42 (0.04)	− 0.53 (0.0)	0.32
$\langle\sigma_{\rm mol}\rangle$	Natres-hightar	0.71 (0.16)	− 1.88 (0.04)	0.76 (0.0)	0.19	− 0.52 (0.22)	− 0.44 (0.06)	− 0.51 (0.0)	0.27
$\langle\sigma_{\rm mol}\rangle$	Lowres	0.52 (0.09)	− 1.96 (0.03)	0.54 (0.0)	0.25	− 0.51 (0.11)	− 0.37 (0.03)	− 0.43 (0.0)	0.32
$\langle\sigma_{\rm mol}\rangle$	Lowres-midtar	0.73 (0.16)	− 2.02 (0.05)	0.56 (0.0)	0.32	− 0.69 (0.19)	− 0.35 (0.05)	− 0.47 (0.0)	0.36
$\langle\sigma_{\rm mol}\rangle$	Lowres-hightar	0.53 (0.13)	− 2. (0.04)	0.76 (0.0)	0.16	− 0.46 (0.18)	− 0.33 (0.06)	− 0.58 (0.0)	0.21
$\langle\sigma_{\rm mol}\rangle$	Midres	0.72 (0.08)	− 1.96 (0.02)	0.89 (0.0)	0.15	− 0.85 (0.17)	− 0.33 (0.05)	− 0.57 (0.0)	0.36
$\langle\sigma_{\rm mol}\rangle$	Midres-hightar	0.76 (0.11)	− 2.00 (0.03)	0.95 (0.0)	0.13	− 0.76 (0.25)	− 0.29 (0.08)	− 0.68 (0.0)	0.26
$\langle\sigma_{\rm mol}\rangle$	Highres	0.95 (0.15)	− 1.97 (0.04)	0.91 (0.0)	0.17	− 0.78 (0.25)	− 0.34 (0.07)	− 0.69 (0.0)	0.26
$\langle\alpha_{\rm vir}\rangle$	Natres	...	...	0.27 (0.014)	...	...	...	− 0.24 (0.032)	...
$\langle\alpha_{\rm vir}\rangle$	Natres-midtar	...	...	0.51 (0.0)	...	...	...	− 0.22 (0.155)	...
$\langle\alpha_{\rm vir}\rangle$	Natres-hightar	...	...	0.38 (0.087)	...	...	...	− 0.16 (0.475)	...
$\langle\alpha_{\rm vir}\rangle$	Lowres	...	...	0.17 (0.14)	...	...	...	− 0.11 (0.361)	...
$\langle\alpha_{\rm vir}\rangle$	Lowres-midtar	...	...	0.26 (0.128)	...	...	...	0.01 (0.936)	...
$\langle\alpha_{\rm vir}\rangle$	Lowres-hightar	...	...	0.58 (0.031)	...	...	...	− 0.27 (0.354)	...
$\langle\alpha_{\rm vir}\rangle$	Midres	...	...	0.56 (0.0)	...	...	...	− 0.19 (0.271)	...
$\langle\alpha_{\rm vir}\rangle$	Midres-hightar	...	...	0.77 (0.003)	...	...	...	− 0.44 (0.155)	...
$\langle\alpha_{\rm vir}\rangle$	Highres	...	...	0.62 (0.019)	...	...	...	− 0.29 (0.311)	...
$\langle P_{\rm turb}\rangle$	Natres	0.14 (0.02)	− 1.92 (0.02)	0.72 (0.0)	0.19	− 0.14 (0.03)	− 0.38 (0.03)	− 0.47 (0.0)	0.32
$\langle P_{\rm turb}\rangle$	Natres-midtar	0.19 (0.02)	− 1.98 (0.03)	0.82 (0.0)	0.19	− 0.18 (0.04)	− 0.35 (0.05)	− 0.56 (0.0)	0.32
$\langle P_{\rm turb}\rangle$	Natres-hightar	0.20 (0.04)	− 2. (0.04)	0.85 (0.0)	0.17	− 0.16 (0.05)	− 0.36 (0.06)	− 0.63 (0.0)	0.25
$\langle P_{\rm turb}\rangle$	Lowres	0.14 (0.02)	− 1.95 (0.03)	0.59 (0.0)	0.25	− 0.14 (0.03)	− 0.37 (0.03)	− 0.49 (0.0)	0.32
$\langle P_{\rm turb}\rangle$	Lowres-midtar	0.2 (0.04)	− 2. (0.05)	0.61 (0.0)	0.32	− 0.2 (0.05)	− 0.37 (0.05)	− 0.55 (0.0)	0.35
$\langle P_{\rm turb}\rangle$	Lowres-hightar	0.15 (0.03)	− 1.98 (0.03)	0.85 (0.0)	0.16	− 0.13 (0.04)	− 0.36 (0.05)	− 0.66 (0.0)	0.20
$\langle P_{\rm turb}\rangle$	Midres	0.2 (0.02)	− 1.99 (0.02)	0.92 (0.0)	0.17	− 0.23 (0.05)	− 0.32 (0.05)	− 0.64 (0.0)	0.35
$\langle P_{\rm turb}\rangle$	Midres-hightar	0.21 (0.03)	− 2.02 (0.03)	0.96 (0.0)	0.14	− 0.20 (0.06)	− 0.3 (0.07)	− 0.75 (0.0)	0.24
$\langle P_{\rm turb}\rangle$	Highres	0.26 (0.04)	− 2.07 (0.04)	0.95 (0.0)	0.16	− 0.21 (0.06)	− 0.26 (0.07)	− 0.74 (0.0)	0.25

Note. Analogous to Table I1 but for CS(2–1).

[1]*Argelander-Institut für Astronomie, Universität Bonn, Auf dem Hügel 71, D-53121 Bonn, Germany*
[2]*Department of Astronomy, The Ohio State University, 4055 McPherson Laboratory, 140 West 18th Ave, Columbus, OH 43210, USA*
[3]*European Southern Observatory, Karl-Schwarzschild Straße 2, D-85748 Garching bei München, Germany*
[4]*Observatorio Astronómico Nacional (IGN), C/Alfonso XII, 3, E-28014 Madrid, Spain*
[5]*Center for Astrophysics | Harvard & Smithsonian, 60 Garden St, Cambridge, MA 02138, USA*
[6]*INAF – Osservatorio Astrofisico di Arcetri, Largo E. Fermi 5, I-50125 Florence, Italy*
[7]*Max-Planck-Institut für Extraterrestrische Physik (MPE), Giessenbachstrasse 1, D-85748 Garching, Germany*
[8]*Institut für Theoretische Astrophysik, Zentrum für Astronomie, Universität Heidelberg, Albert-Ueberle-Straße 2, D-69120 Heidelberg, Germany*
[9]*Cosmic Origins Of Life (COOL) Research DAO, coolresearch.io*
[10]*Department of Physics and Astronomy, University of Wyoming, Laramie, WY 82071, USA*
[11]*Research School of Astronomy and Astrophysics, Australian National University, Canberra, ACT 2611, Australia*
[12]*ARC Centre of Excellence for All Sky Astrophysics in 3 Dimensions (ASTRO 3D), Mount Stromlo Rd, Stromlo, ACT 2611, Australia*
[13]*Max Planck Institute for Astronomy, Königstuhl 17, D-69117 Heidelberg, Germany*
[14]*Astrophysics Research Institute, Liverpool John Moores University, 146 Brownlow Hill, Liverpool L3 5RF, UK*
[15]*Centro de Desarrollos Tecnológicos, Observatorio de Yebes (IGN), E-19141 Yebes, Guadalajara, Spain*
[16]*Interdisziplinäres Zentrum für Wissenschaftliches Rechnen, Universität Heidelberg, Im Neuenheimer Feld 205, D-69120 Heidelberg, Germany*
[17]*Sterrenkundig Observatorium, Universiteit Gent, Krijgslaan 281 S9, B-9000 Gent, Belgium*
[18]*Institut de Radioastronomie Millimétrique (IRAM), 300 Rue de la Piscine, F-38406 Saint Martin d'Hères, France*
[19]*LERMA, Observatoire de Paris, PSL Research University, CNRS, Sorbonne Universités, F-75014 Paris, France*
[20]*Department of Physics, University of Alberta, Edmonton, AB T6G 2E1, Canada*
[21]*Department of Physics and Astronomy, McMaster University, 1280 Main Street West, Hamilton, ON L8S 4M1, Canada*

[22]*Canadian Institute for Theoretical Astrophysics (CITA), University of Toronto, 60 St George Street, Toronto, ON M5S 3H8, Canada*
[23]*Center for Astrophysics and Space Sciences, Department of Physics, University of California San Diego, 9500 Gilman Drive, La Jolla, CA 92093, USA*
[24]*Sub-department of Astrophysics, Department of Physics, University of Oxford, Keble Road, Oxford OX1 3RH, UK*

This paper has been typeset from a TEX/LATEX file prepared by the author.